ESCUELA TÉCNICA SUPERIOR DE INGENIEROS AERONÁUTICOS
UNIVERSIDAD POLITÉCNICA DE MADRID

DOCTORAL THESIS

Matrix-free time-stepping methods for the solution of TriGlobal instability problems

by
FRANCISCO JOSÉ GÓMEZ CARRASCO
under the direction of
RAQUEL GÓMEZ MIGUEL & VASSILIOS THEOFILIS
School of Aeronautics, Universidad Politécnica de Madrid
Plaza Cardenal Cisneros 3, E-28040 Madrid, SPAIN

Madrid, September 2013

POLITÉCNICA

Tribunal nombrado por el Sr. Rector Magfco. de la Universidad Politécnica de Madrid, el día 22 de mayo de 2013

Presidente: D. José Manuel Vega de Prada

Vocal: D. Julio Soria

Vocal: D. Enrique Sammiguel Rojas

Vocal: D. Alejandro Seilla Santiago

Secretario: D. Leo Miguel González Gutiérrez

Suplente: D. Eduardo Fernández Tarazo

Suplente: D. José Antonio Moriñigo Madueño.

Realizado el acto de defensa y lectura de la Tesis el día 2 de septiembre de 2013 en la E.T.S.I. /~~Facultad~~ Aeronáuticos

Calificación APTO

EL PRESIDENTE

LOS VOCALES

Eduardo Fernández

EL SECRETARIO

Abstract

Most flows of engineering relevance still remain unexplored in a global instability theory context for two reasons. First, because of the difficulties associated with the analysis of turbulent flows and, second, for the formidable computational resources required for the solution of the eigenvalue problem associated with the instability analysis of three-dimensional base flows, also known as TriGlobal problem.

In this thesis, the problem associated with the three-dimensionality is addressed by means of the development of a general approach to the solution of large-scale global linear instability analysis by coupling a time-stepping approach with second order aerodynamic codes employed in industry.

Three challenging flows in the terms of required computational resources and physical complexity have been chosen for demonstration of the present methodology; (i) the flow inside a wall-bounded three-dimensional lid-driven cavity, (ii) the flow past a cylinder fitted with helical strakes and (iii) the flow over a inhomogeneous three-dimensional open cavity. Results in excellent agreement with the literature have been obtained for the three-dimensional lid-driven cavity by using this methodology coupled with the incompressible solver of the open-source toolbox OpenFOAM®, which has served as validation. Moreover, significant physical insight of the instability of three-dimensional open flows has been gained through the application of the present time-stepping methodology to the other two cases. In addition, modifications to the present approach have been proposed in order to perform adjoint instability analysis of three-dimensional base flows and flow control; validation and TriGlobal examples are presented.

Finally, it has been demonstrated that the moderate amount of computational resources required for the solution of the TriGlobal eigenvalue problem using this method enables the performance of instability analysis and control of flows of industrial relevance.

Resumen

La inmensa mayoría de los flujos de relevancia ingenieril permanecen sin estudiar en el marco de la teoría de estabilidad global. Esto es debido a dos razones fundamentalmente, las dificultades asociadas con el análisis de los flujos turbulentos y los inmensos recursos computacionales requeridos para obtener la solución del problema de autovalores asociado al análisis de inestabilidad de flujos tridimensionales, también conocido como problema TriGlobal.

En esta tesis se aborda el problema asociado con la tridimensionalidad. Se ha desarrollado una metodología general para obtener soluciones de problemas de análisis modal de las inestabilidades lineales globales mediante el acoplamiento de métodos de evolución temporal, desarrollados en este trabajo, con códigos de mecánica de fluidos computacional de segundo orden, utilizados de forma general en la industria. Esta metodología consiste en la resolución del problema de autovalores asociado al análisis de inestabilidad mediante métodos de proyección en subespacios de Krylov, con la particularidad de que dichos subespacios son generados por medio de la integración temporal de un vector inicial usando cualquier código de mecánica de fluidos computacional.

Se han elegido tres problemas desafiantes en función de la exigencia de recursos computacionales necesarios y de la complejidad física para la demostración de la presente metodología: (i) el flujo en el interior de una cavidad tridimensional impulsada por una de sus tapas, (ii) el flujo alrededor de un cilindro equipado con aletas helicoidales a lo largo su envergadura y (iii) el flujo a través de una cavidad abierta tridimensinal en ausencia de homogeneidades espaciales. Para la validación de la tecnología se ha obtenido la solución del problema TriGlobal asociado al flujo en la cavidad tridimensional, utilizando el método de evolución temporal desarrollado acoplado con los operadores numéricos de flujo incompresible del código CFD OpenFOAM (código libre). Los resultados obtenidos coinciden plentamente con la literatura. La aplicación de esta metodología al estudio de inestabilidades globales de flujos abiertos tridimensionales ha proporcionado por primera vez, información sobre la transición tridimensional de estos flujos. Además, la metodología ha sido adaptada para resolver problemas adjuntos TriGlobales, permitiendo el control de flujo basado en modificaciones de las inestabilidades globales.

Finalmente, se ha demostrado que la cantidad moderada de los recursos computacionales requeridos para la solución del problema de valor propio TriGlobal usando este método numérico, junto a su versatilidad al poder acoplarse a cualquier código aerodinámico, permite la realización

de análisis de inestabilidad global y control de flujos complejos de relevancia industrial.

Agradecimientos

A Paula y mis padres

Durante la realización de esta tesis he recibido el apoyo de muchas personas. Sin ellos este trabajo no habría sido tan gratificante y satisfactorio. En estas líneas quiero agradecer a estas personas su ayuda.

Primero tengo que agradecer a mis directores de tesis Raquel y Vassilis por su interés y paciencia durante estos años. De Raquel he aprendido que siempre hay que luchar por lo que uno quiere y de Vassilis espero haber adquirido algo de su pasión por la investigación y capacidad de buscar respuestas.

Aproximádamente la mitad de este trabajo se ha realizado en el Área de Propulsión del Instituto Nacional de Técnica Aerospacial "Esteban Terradas" (INTA) gracias a una beca FPI "Calvo Rodés". Durante ese tiempo me he beneficiado de una atmósfera de trabajo inmejorable y unos excelentes compañeros con los que he tratado diriamente. Quiero agradecer por su ayuda a José Hermida, Gonzalo, Javier Conde, Pablo, Eduardo, Ernesto, José Luis, Quique y Miriam de mi Área, a nuestros vecinos de energía en el R-02, especialmente a Carmen, Jesús y Antonio por sus discusiones matinales, y a Ruth por su ayuda en temas del cluster - todos ellos son una pequeña muestra de una lista interminable de buenos compañeros.

La otra mitad de este doctorado la he realizado en el grupo de Mecánica de Fluidos Computacional de la ETSI Aeronáuticos. Gracias a esto, no sólo he podido beneficiarme de contar con Vassilis como co-director de tesis, sino que he contado con unos excelentes compañeros de grupo de investigación, entre los que he encontrado ejemplos de perfección, eficiencia y perseverancia. En orden cronológico quiero agradecer su ayuda a Daniel Rodríguez, Javier de Vicente, Leo González, José Miguel Pérez, Pedro Paredes, Elmer Gennaro, Miguel Hermanns, Juan Ángel Tendero, Soledad Le Clainche, Mamta Jotkar, Qiong Liu, Wei He y Takashi Nakazawa.

También quiero agradecer a los profesores que me han acogido durante las estancias académicas que realicé gracias al proyecto Marie Curie Grant PIRSES-GA-2009-247651 "FP7-PEOPLE-IRSES: ICO-MASEF *Instability and Control of Massively Separated Flows*"; Hugh Blackburn en la Univer-

sidad de Monash, Julio Meneghini y Bruno Carmo en la Universidad de Sao Paulo, y Pino Martin en la Universidad de Maryland. Mi tiempo en sus grupos de investigación fue muy provechoso no sólo para mi formación, sino cómo una gran experiencia personal.

Finalmente, esta tesis no hubiera sido posible sin el apoyo y comprensión de toda mi familia, especialmente de mi hermana Ana Belén, y amigos durante todos estos años de duro trabajo.

Muchas gracias a todos.

Contents

Nomenclature **xxi**

1 Introduction **1**

1.1 Overview 3

1.2 List of Papers 4

2 Hydrodynamic Instability **7**

2.1 Theoretical considerations 7

2.1.1 Modal Theory: Global Modes 10

2.1.2 Non-modal Theory: Optimal Perturbations 10

2.1.3 On the relation between numerical residuals and global modes 11

2.1.4 Strobes (snapshots), Chronoi (times) and Topoi (spaces) 11

2.1.5 Koopman modes and Dynamic Mode Decomposition 13

2.1.6 On the relation between numerical and empirical eigenmodes 14

2.1.7 TriGlobal linear modal instability analysis of incompressible flows 15

3 Direct Numerical Simulation **17**

3.1 Compressible Flow 17

3.1.1 Finite Volume Method (BERTA) 17

3.2 Incompressible Flow 19

3.2.1 Finite Volumes Method (OpenFOAM) 19

3.2.2 Spectral Collocation Method (SCM) 19

3.2.3 Spectral Elements Methods (Semtex) 21

4 Numerical Solution of the Eigenvalue Problem using Time-stepping 23

4.1 Eigenspectrum Computation 23

4.1.1 QR algorithm 23

4.1.2 Krylov-subspace methods: Arnoldi algorithm 23

4.2 Jacobian-free Newton–Krylov methods 25

4.3 Exponential Time-Stepping Transformation using full DNS 25

4.4 Exponential Time-Stepping Transformation using LNSE 27

4.4.1 Improving the algorithm: Shift-Invert Exponential Transformation 27

5 Validation of Time-Stepping Methodology 31

5.1 Case study: 2D square lid-driven cavity 31

5.1.1 Parameters selection 31

5.1.2 Validation results 32

5.2 Comparison of time-stepping with alternative EVP solution methodologies 37

5.3 Validation of the exponential shift-invert methodology 41

6 Time-stepping for TriGlobal Instability Analysis of Wall-bounded Flows 45

6.1 Three-dimensional Lid-driven Cavity 45

6.1.1 Base Flow 47

6.1.2 TriGlobal Instability Analyses 50

7 Time-stepping for TriGlobal Instability Analysis of Open Flows 59

7.1 Cylinder fitted with Helical Strakes 59

7.1.1 Base Flow 62

7.1.2 Instability Analysis 64

7.2 Flow over an inhomogeneous open cavity flow 71

7.2.1 Base Flow 71

7.2.2 Instability analysis 73

8 Flow Control Aspects 75

8.1 Flow control via state space system 75

8.2 Flow control via adjoint operator 76

8.3 Sensitivity of the flow past a circular cylinder 79

8.4 Sensitivity of the flow inside a three-dimensional lid-driven cavity 80

9 Conclusions 83

Appendix A: Direct and adjoint LNSE using the PISO algorithm 85

List of Figures

4.1 Shift-invert transformation 24

4.2 Temporal exponential transformation 26

4.3 Flux diagram of the proposed time-stepping algorithm 27

4.4 Shift-invert exponential transformation 29

5.1 Spectrum of the 2D LDC at $Re = 200$ obtained with three different methods 33

5.2 Leading eigenmode of the 2D LDC obtained using DNS and a JFNK time-stepping method at $Re = 200$ 34

5.3 First and second mode of the 2D LDC using RA, TS, DMD,BG at $Re = 2000$ 39

5.4 2D LDC instability results using RA, DMD and POD at $Re = 2000$ 40

5.5 Details of the mesh used for the stenotic flow 41

5.6 Velocity modulus of the most unstable eigenvector of the stenotic flow calculated with different methods 42

6.1 Geometrical description of the 3D lid-driven cavity and main flow features 46

6.2 Comparisons of normal velocities in the central lines $(x, 0, 0)$ y $(0, y, 0)$ of cubic lid-driven cavity at $Re = 1000$ 49

6.3 Temporal evolution of the velocity residual of the two-dimensional lid-driven cavity at $Re = 1000$ 50

6.4 Spectrum of cubic lid-driven cavity at $Re = 1000$ 51

6.5 Real part of the eigenfunction velocity field $(\hat{u}, \hat{v}, \hat{w})$ of the cubic lid-driven cavity at $Re = 1000$. 52

6.6 Temporal evolution of the velocity residual of the cubic three-dimensional singular lid-driven cavity at $Re = 2000$ 53

6.7 Three different states in the temporal evolution of the velocity residual of the cubic LDC at $Re = 2000$ 54

6.8 Real part of the eigenfunction velocity field $(\hat{u}, \hat{v}, \hat{w})$ of the cubic lid-driven cavity at $Re = 2000$ 55

6.9 Real part of the eigenfunction velocity field $(\hat{u}, \hat{v}, \hat{w})$ of the leading (*top*) and second (*bottom*) eigenmodes of the $AR = 1 : 1 : 2$ lid-driven cavity at $Re = 1000$ 56

6.10 Real part of the eigenfunction velocity field $(\hat{u}, \hat{v}, \hat{w})$ of the leading (*top*) and second (*bottom*) eigenmodes of the $AR = 1 : 1 : 3$ lid-driven cavity at $Re = 1000$ 56

7.1 Geometry of a circular cylinder fitted with helical strakes 59

7.2 Employed domain for the simulation of flow past a cylinder fitted with helical strakes 62

7.3 Geometry and Mesh of the cylinder fitted with helical strakes 64

7.4 Instant snapshots of the streamwise vorticity component and streamlines at plane $z = 5$ of the flow around a cylinder fitted with straight strakes at different phase angles at $Re = 40$ 65

7.5 Non-linear least-square fitting of the lift coefficient C_L residual of the flow past a straked cylinder at *(left)* $Re = 40$ *(right)* $Re = 50$. 66

7.6 Comparison of average in time C_D drag coefficient between the straked cylinder and the bare cylinder 67

7.7 Comparison of St number and λ between the straked cylinder and the bare cylinder 68

7.8 Velocity eigenfunctions of the leading (damped) eigenmode of the straked cylinder at $Re = 40$ 69

7.9 Isosurface of spanwise velocity $w = \pm 0.2$ at $Re = 100$ and bottom $w = \pm 0.1$ 70

7.10 Difference between wakes of *(top)* Bare cylinder and *(bottom)* Straked Cylinder at $Re = 100$. $v = \pm 0.3$ 70

7.11 Power density spectrum of the drag coefficients C_D at (*left*) $Re = 120$ (*middle*) $Re = 160$ (*right*) $Re = 200$ 71

7.12 Employed domain and mesh for the simulation of flow over the three-dimensional $AR = 1 : \frac{1}{5} : \frac{1}{5}$ open cavity 72

7.13 Leading global mode of a three-dimensional open cavity 73

7.14 $y-$vorticity component in plane $y = 0$ of the leading eigenmode of the open cavity at $Re = 100$ 74

8.1 Normalized module of the leading eigenvector of the cylinder wake at $Re = 40$ 80

8.2 Normalized module of the adjoint leading eigenvector of the cylinder wake and contour plot of the function $\delta\lambda(x, y)$ 80

8.3 Normalized module of the direct and adjoint modes of the LDC at $Re = 1000$ 81

8.4 Contour plot of the function $\delta\lambda(x, y, z)$ of the cubic LDC at $Re = 1000$ 82

List of Tables

2.1 Classification of global linear theory approaches 8

5.1 Influence of τ on FVM results 35

5.2 Influence of ϵ_0 on SCM results 35

5.3 Influence of ϵ on FVM results 36

5.4 Influence of mesh resolution n on SCM results 36

5.5 Influence of mesh resolution on FVM results 36

5.6 Damping rate of the leading stationary eigenmode obtained by solution of the global instability eigenvalue problem and DMD analysis of transient DNS data 37

5.7 Convergence of most unstable eigenvalues for stenosis flow at $Re = 700$ 41

5.8 Number of iterations carried out by the Bi-CGSTAB algorithm for the stenosis flow problem at $Re = 700$ 42

5.9 Number of iterations carried out by the shift-invert algorithm for the stenosis flow problem at $Re = 500$ for different tolerances 43

5.10 Number of iterations carried out by the Bi-CGSTAB algorithm for the stenosis flow problem at $Re = 500$ and at different integration times Δt 43

6.1 Grid convergence study based on u velocity for the cubic Lid-Driven cavity at $Re = 1000$ 48

6.2 Comparison with the benchmark solution of the minimum and maximum velocities on the centerlines v(x, 0.5, 0.5) and u(0.5, y, 0.5) for the cubic lid-driven cavity at Re = 1000 49

6.3 Effect of resolution on the first three leading eigenvalues of the lid driven cavity at $Re = 1000$ 52

6.4 Effect of aspect ratio $AR = 1 : A_y : A_z$ on the first three leading eigenvalues of the lid driven cavity at $Re = 200$ 55

6.5 Computational costs of the instability analysis of the cubic LDC at $Re = 1000$ . . . 57

7.1 Grid convergence study based on drag coefficient C_D for the bare cylinder at $Re = 40$ 63

7.2 Comparison with previous results based on drag coefficient C_D and length of the separation bubble L_w measured from the rear stagnation point 63

7.3 Time averaged drag coefficient C_D, Strouhal number St and recirculation bubble length L_w of a two-dimensional cylinder fitted with straight strakes at different phase angle 64

7.4 Grid convergence study based on the velocity downstream of the open cavity 73

List of Algorithms

1 Arnoldi Iteration 24

2 Instability analysis with full Navier–Stokes 26

3 Instability analysis with LNSE 28

4 Exponential shift-invert algorithm 30

5 Instability analysis with adjoint exponential operator 78

6 Instability analysis with direct and adjoint power iteration 79

7 PISO algorithm 86

Nomenclature

Abbreviations

BG	BiGlobal Analysis
CFL	Courant Number
DMD	Dynamic Mode Decomposition
DNS	Direct Numerical Simulation
EVP	EigenValue Problem
FVM	Finite Volume Method
LDC	Lid-driven Cavity
LES	Large Eddy Simulation
LST	Linear Stability Theory
OSE	Orr-Sommerfeld Equation
POD	Proper Orthogonal Decomposition
PSE	Parabolized Stability Equation
RA	Residual Algorithm
ROM	Reduced Order Model
SCM	Spectral Collocation Method
SVD	Singular Value Decomposition
TGL	Taylor-Görtler-Like vortices
TS	Time-stepping

Latin Symbols

$\mathbf{A}$	Jacobian Matrix
$\mathbf{H}$	Hessenberg Matrix
$\mathbf{K_m}$	Krylov subspace
m	Krylov subspace dimension
N	Number of nodes in one spatial direction
$\mathbf{q}$	Generalized instantaneous flow vector
$\bar{\mathbf{q}}$	Generalized base flow vector
$\hat{\mathbf{q}}$	Generalized vector of amplitude functions
Re	Reynolds number
$\bar{\mathbf{u}}$	Incompressible base flow components

$\mathbf{u}'$	Incompressible perturbation components
$\hat{\mathbf{u}}$	Incompressible vector of amplitude functions
$\mathbf{v}'$	Incompressible adjoint perturbation components
$\hat{\mathbf{v}}$	Incompressible vector of adjoint amplitude functions
x, y, z	Spatial coordinates

Greek Symbols

α	Wave number
Δt	Time step in temporal integration
γ, δ	Floquet multiplier, Floquet exponent
$\lambda, \mu, \sigma, \omega$	Eigenvalues
Θ	Phase function
$\boldsymbol{\phi}$	Empirical eigenfunction
$\boldsymbol{\Phi}$	Propagator operator
τ	Integration time
ϵ	Perturbation magnitude
ϵ_r	Relative error
ϵ_m	Numerical tolerance
ϵ_o	Initial order of perturbation magnitude
$\varepsilon(t)$	Integration residual at time t

Chapter 1

Introduction

Global linear instability analysis [1] plays an essential role in the investigation of the sequence of physical mechanisms leading laminar flow in complex, spatially inhomogeneous geometries through transition to turbulence. The theory deals with the temporal and spatial evolution (growth/decay) of small-amplitude perturbations superimposed upon a steady or unsteady laminar base flow. The assumption of asymptotic (long-time) instability leads to a generalized large-scale eigenvalue problem, the challenging numerical solution of which provides the spectrum of linear global modes composed of the modal frequencies and amplification/damping rates. Such numerical solution can be obtained within two classes of iterative approaches: a matrix-forming or a matrix-free/Jacobian-free framework [1] . The main difference between the two approaches is that matrix-forming strategies provide access to larger subsets of the full spectrum at the cost of large computational memory (RAM memory) while matrix-free methods provides smaller subsets of the spectrum at the cost of long time integration (CPU time). Both frameworks make use of subspace projection-iterative methods such as the Arnoldi iteration which is based on the Krylov-subspace [2, 3] , which is one of the most effective techniques to solve the resulting generalized eigenproblem when formation of the full discretized matrix is impractical due to the problem size. The Arnoldi method delivers a window of the eigenspectrum but favors the eigenvalues with the largest modulus, thus a transformation of the spectrum is required in order to introduce an eigenvalue shift towards the interesting part of the spectrum. The shift-invert transformation was first introduced in fluid mechanics instability analysis research in a matrix-forming context by Natarajan and Acrivos [4] , while the time-stepping exponential transformation was first developed by Erikson & Rizzi [5] in a Jacobian-free framework. A recent review [1] provides a discussion of the suite of matrix transformation methods used, while recent progress and challenges using these two frameworks has been recently presented by Gómez et al. [6].

Although a large number of studies using the two different frameworks have reported significant insight in instability mechanisms over the last four decades in relatively complex flows with one homogeneous spatial direction, such as attachment lines [7] or open cavities [8], most flows of practical engineering significance still remain unexplored, owing to two main reasons.

The first reason arises from the difficulties associated to the analysis of turbulent flows, an issue not discussed in this thesis; the interested reader is referred to the works of Hussain & Reynolds [9], Crouch et al. [10, 11], Biau et al. [12] and Nichols & Lele [13] amongst others.

The second reason for the relatively little attention paid to the analysis of flows of industrial interest is that the basic state of most practical flows are three-dimensional depending in an inhomogeneous manner on the three spatial directions, and no assumptions regarding spatial homogeneity can be made. This is the problem addressed in this thesis, in an analysis context known as TriGlobal linear stability. Although the single parameter of the instability problem in this situation in incompressible flow is the Reynolds number, the cost of performing a complete parametric instability analysis can be prohibitively expensive when the matrix discretizing the eigenvalue problem is solved in a dense matrix-forming framework, as inferred from the work of Rodríguez & Theofilis [14], in which a $O(1)$ Tb RAM memory matrix was formed, stored and inverted, despite the fact that the instability analysis concernes a flow with one homogeneous spatial direction.

Although recent high-order sparse matrix-forming methods have recently been shown to provide $O(10^4)$ speed-up with respect to dense matrix-forming approaches [15] , matrix-free methods remain the method of choice for TriGlobal linear instability analysis problem. The key advantage of matrix-free time-marching methods, over explicit formation of the Jacobian matrix, is that the large-sized matrices describing spatial discretization of global linear instability analysis applications in two or three inhomogeneous spatial directions resolved in a coupled manner is never formed. This enables the study of global linear stability problems on small main-memory machines at the expense of long-time integrations. A rather complete discussion of time-stepping approaches for global linear instability has recently been presented by Barkley, Blackburn and Sherwin [16]. The first successful time-stepping methodology, by Erikson & Rizzi [5], introduced a numerical differentiation of a direct numerical simulation (DNS) code used together with a temporal polynomial approximation. In that work, finite differences were used in order to study an inviscid incompressible flow over a NACA airfoil. Chiba [17] improved the Erikson & Rizzi approach by introducing a temporal exponential transformation using a full Navier-Stokes equations solver. Following Chiba's method, Tezuka and Suzuki [18, 19] successfully solved the first ever TriGlobal problem. In parallel, Edwards et al. [20] developed a time-stepping methodology in conjunction with the linearized Navier-Stokes equations, which has been successfully used and popularized by Barkley et al. [21], Tuckerman et al. [22] and many others. Although these previously mentioned algorithms are able to provide only a part of the spectrum, recent matrix-free algorithms can provide access to any part of the spectrum using time-stepping approaches, e.g. Bagheri et al. [23] and elsewhere [24, 25].

Despite these new capabilities for global stability analysis that recent sparse matrix-forming and matrix-free algorithms offer, only a number of small canonical configurations with three inhomogeneous spatial directions have been analyzed with respect to their linear instability; to the best knowledge of the author, these are the spheroid [19], an incompressible jet in a cross flow [26], an sphere [27], and the three-dimensional, lateral-wall-bounded lid-driven cavity [28, 29, 30, 31] . This lack of TriGlobal analyses in the literature can be attributed to the fact that the time-stepping matrix-free methodology requires a three-dimensional direct numerical simulation (DNS) solver and the development and validation of a three-dimensional DNS capable of handling different geometries is non-trivial.

Furthermore, the introduction of time-stepping ideas into standard aerodynamics codes, with the aim of broadening the scope of the analysis in transonic, supersonic and hypersonic flow over or through complex geometries is a non-trivial task, on account of the potentially distinct requirements of the robustness needed for aerodynamics codes to converge versus the accuracy needed for stability calculations. While the majority of spatial discretization methods employed in CFD have also been used for the solution of the global EVP in a matrix-formation context [1], the vast majority of

time-stepping approaches to solve the same problem have been implemented in conjunction with incompressible flow and high-order (typically spectral-element) spatial discretization. In following the latter path, some of the most interesting flow phenomena associated with compressible flow have remained out of the scope of global instability analysis.

The goal of this thesis is to present an algorithm for TriGlobal modal linear instability analysis that can overcome the excessive computational requirements of the matrix-forming techniques and the necessity of developing a three-dimensional direct numerical simulation solver for the specific task. This would be accomplished by linking matrix-free/Jacobian-free instability algorithms with existing general purpose aerodynamic codes, the latter run in direct numerical simulation mode. Moreover, the necessity of flexibility and ability to handle complex geometries makes second-order standard aerodynamic codes the first candidate to be examined regarding their suitability for TriGlobal instability analysis. Although no work is known to date that deals with the numerical solution of large-scale TriGlobal eigenvalue problems using standard aerodynamic codes, leaving most problems of practical engineering significance still unexplored, second-order methods have been already successfully used in global linear instability theory both for the solution of the BiGlobal [32, 33, 34, 35, 36] and that of the TriGlobal linear EVP [28]. High-order accurate spectral element methods [37, 38, 39] or finite elements [40, 41] may provide a better convergence rate for a given resolution than second-order finite volumes methods while maintaining geometry flexibility, however open-source codes based on second-order finite-volume spatial discretization have been chosen for this work because of its flexibility, ease of performing source-code modifications and the ability such codes offer to study different flow regimes in future research.

1.1 Overview

The rest of the thesis is organized into eight chapters, each one addressing a differentiated aspect of the present research work.

- Chapter 2: This chapter addresses theoretical considerations on hydrodynamic instabilities and introduces a mathematical description of the global linear modal instability theory, in which global modes are defined. Alternative methods of flow structures identification techniques such as residual algorithm, dynamic mode decomposition or proper orthogonal decomposition are briefly explained for the sake of comparison. A TriGlobal eigenvalue problem is derived from the incompressible Navier–Stokes equations, whose efficient solution is the objective of the thesis.

- Chapter 3: The different numerical methods employed in this thesis for the time-accurate solution of the Navier-Stokes equations are introduced in this chapter. High-order spectral, $hp-$spectral elements and second-order finite volume codes used for solving the temporal evolution of the flow are described. A compressible solver is also included for the sake of completeness.

- Chapter 4: This chapter describes the mathematical fundamentals of the numerical methods and algorithms employed for the solution of the TriGlobal eigenvalue problem in a matrix-free time-stepping context. The development of a general Jacobian-free approach for the solution of large-scale global linear instability analysis eigenvalue problems is presented, by coupling a time-stepping algorithm with industry-standard second-order accurate aerodynamic codes. In addition, an alternative exponential shift-invert strategy is introduced.

- Chapter 5: Validation and verification of the developed numerical methodology coupled with high and low-order codes is presented using a canonical two-dimensional square lid-driven cavity as base flow. Instability results from this same base flow are compared to other results obtained using POD and DMD. Finally, shift-invert exponential transformation is validated using a stenotic flow from the literature using the spectral element code.

- Chapter 6: The instability of a three-dimensional lid-driven cavity, a challenging flow in the context of required computational resources and physical complexity, is studied in this chapter. Results in excellent agreement with the literature are obtained by using the proposed theoretical methodology coupled with the incompressible solver of the open-source toolbox OpenFOAM®.

- Chapter 7: Although several investigations have been performed in order to predict the performance of helical strakes in mitigating or suppressing vortex shedding behind circular cylinders, proving its efficiency in specific configurations, little is understood regarding the physical mechanisms leading to the efficiency of these devices. The present chapter addresses this question from a global linear instability analysis point of view by applying the developed algorithm for the three-dimensional global (TriGlobal) at low Reynolds number in order to understand more deeply the flow instabilities and physical mechanisms that mitigate or suppress the vortex-shedding. A challenging inhomogeneous three-dimensional open cavity is also analyzed for further demonstration of the numerical method.

- Chapter 8: The influence and utility of this theory is explored in the context of flow control of three-dimensional flows with absence of homogeneity in all spatial directions, in which classical control of dynamical systems theory and adjoint methods are taking into account.

- Chapter 9: The obtained capabilities of the present methodology are summarized in this Chapter.

1.2 List of Papers

Most of the material in this rhesis, along with additional specific details, has been presented in the following publications:

- **Journal Papers** (JCR Peer-Reviewed)

  - Gómez, F., Le Clainche, S., Paredes, P., Hermanns, M., and Theofilis, V., "Four Decades of Studying Global Linear Instability: Progress and Challenges" AIAA Journal, Vol. 50, No 12, 2012, pp 2731-2743
  - Gómez, F., Gómez, R., Theofilis, V., "On three-dimensional global linear instability analysis of flows with standard aerodynamics codes" Accepted in Aerospace Science and Technology
  - Gómez, F., Pérez, J.M., Blackburn, H., Theofilis, V., "A novel shift-invert strategy for global flow instability analysis using matrix-free methods" Submitted to Journal of Computational Physics
  - Gómez, F., Pérez, J.M., Theofilis, V., "Direct and Adjoint Global Stability Analisys using OpenFOAM" Submitted to Aerospace Science and Technology

- **Conference Papers** (Peer-Reviewed with ISBN/ISSN)
  - Gómez, F., Carmo, B., Meneghini, J., Gómez, R., and Theofilis, V., "Stability analysis of the flow around a cylinder fitted with helical strakes" 43nd AIAA Fluid Mechanics Conference and Exhibit, San Diego, CA, June 2013, AIAA Paper 2013-2987
  - Le Clainche, S., Gómez, F., Li, I., Soria, J., and Theofilis, V., "3D Global instability analysis and time-resolved particle image velocimetry on a hemisphere-cylinder" 51st AIAA Aerospace Science Meeting, Grapevine, Texas, January 2013, AIAA Paper 2013-0387
  - Gómez, F., Theofilis, V., Paredes, P., Liu, Q., He, W., "On the role of global flow instability analysis in closed loop flow control" 42nd AIAA Fluid Mechanics Conference and Exhibit, New Orleans, Louisiana, June 25-38, 2012, AIAA Paper 2012-2679
  - Pérez, J.M., Gómez, F., Blackburn, H., and Theofilis, V., "A shift-invert strategy for global flow instability using matrix-free methods" 42nd AIAA Fluid Mechanics Conference and Exhibit, New Orleans, Louisiana, June 25-38, 2012, AIAA Paper 2012-3276
  - Gómez, F., Paredes, P., Gómez, R., and Theofilis, V., "Global stability of cubic and large aspect ratio three-dimensional lid-driven cavities" 42nd AIAA Fluid Mechanics Conference and Exhibit, New Orleans, Louisiana, June 25-38, 2012, AIAA Paper 2012-3274
  - Gómez, F., Gómez, R., and Theofilis, V., "Coupling time-stepping numerical methods and standard aerodynamics codes for instability analysis of flows in complex geometries," 6th Theoretical Fluid Mechanics Conference, Honolulu, HI, June 27-30, 2011, AIAA Paper 2011-3753

Chapter 2

Hydrodynamic Instability

2.1 Theoretical considerations

Global linear instability theory is concerned with the temporal or spatial development of small-amplitude perturbations superposed upon laminar steady or time-periodic three-dimensional flows, which are inhomogeneous in two (and periodic in one) or all three spatial directions [1]. The theory addresses flows developing in complex geometries, in which the parallel or weakly nonparallel basic flow approximation invoked by classic linear stability theory does not hold. As such, global linear theory is called to fill the gap in research into stability and transition in flows over or through complex geometries. Historically, global linear instability has been (and still is) concerned with solution of multi-dimensional eigenvalue problems; the maturing of non-modal linear instability ideas in simple parallel flows during the last decade of last century [42, 43, 44] has given rise to investigation of transient growth scenarios in an ever increasing variety of complex flows. The theoretical concepts underlying global linear instability analysis is necessary in order to set the scene for next discussion, which closely follows the works of Theofilis [1].

The key idea is to analyze the development in time and space of small-amplitude perturbations superposed upon a given laminar base flow. This can be described exactly by the linearized Navier-Stokes, continuity and energy equations, without the need to invoke the parallel (or weakly-non-parallel) flow assumption: the flow analyzed with respect to its global stability may be any laminar two- or three-dimensional solution of the equations of motion. The respective theoretical concepts are referred to as *BiGlobal* or *TriGlobal* analyses. Table 2.1 classifies and refines the different kinds of linear stability theory, demarcating the boundaries between *local* analysis based on variants of the Orr-Sommerfeld equation (OSE), *non-local* analysis based on the standard Parabolized Stability Equations (PSE) [45] for base flows weakly varying in one or two directions and the aforementioned versions of *global* linear theory; symbols appearing to be defined shortly.

Linearization of the equations of motion may be performed around steady or unsteady laminar *basic* flows, $\bar{\mathbf{q}} = (\bar{\rho}, \bar{u}, \bar{v}, \bar{w}, \bar{T})^T$. This is to be contrasted against some of the current global instability literature which concerns time-averaged turbulent flows, which will not be dealt with in the present thesis, although some comments on the applicability of the theory, supported by the still scarce evidence in the literature, will be made in what follows.

Basic flows in complex geometries are typically provided by two- or three-dimensional direct numerical simulations, potentially exploiting spatial invariance. Steady laminar flows exist only at low Reynolds numbers, but numerical procedures exist for the recovery of basic flows also at

Table 2.1: Classification of global linear theory approaches

	Denomination	Basic State Assumptions		Phase Function Θ
Global	TriGlobal	-	$\bar{q}(x,y,z)$	ωt
	PSE-3D	$\partial_x\bar{q} \ll \partial_y\bar{q}, \partial_z\bar{q}$	$\bar{q}(x^*,y,z)$	$\int \alpha(x^*)dx^* - \omega t$
	BiGlobal	$\partial_x\bar{q} = 0$	$\bar{q}(y,z)$	$\alpha x - \omega t$
Non-Local	PSE	$\partial_x\bar{q} \ll \partial_y\bar{q}; \partial_z\bar{q} = 0$	$\bar{q}(x^*,y)$	$\int \alpha(x^*)dx^* + \beta z - \omega t$
Local	OSE	$\partial_x\bar{q} = \partial_z\bar{q} = 0$	$\bar{q}(y)$	$\alpha x + \beta z - \omega t$

conditions where linear global instability would be expected, e.g. based on mirroring the solution computed under the imposition of symmetries, continuation [46] or selective frequency damping [47]. In using the term *small-amplitude perturbations*, the decomposition

$$\mathbf{q} = \bar{\mathbf{q}} + \epsilon\tilde{\mathbf{q}},\ \epsilon \ll 1, \tag{2.1}$$

is assumed, and solutions to the initial-value-problem

$$\mathcal{B}(Re, Ma, \bar{\mathbf{q}})\frac{d\tilde{\mathbf{q}}}{dt} = \mathcal{A}(Re, Ma, \bar{\mathbf{q}})\tilde{\mathbf{q}}, \tag{2.2}$$

are sought. Specific comments on the dependence of these quantities on the spatial coordinates, $\mathbf{x}$, and time, t, will be made in what follows. The operators $\mathcal{A}$ and $\mathcal{B}$ are associated with the spatial discretization of the linearized equations of motion and comprise the basic state, $\bar{\mathbf{q}}(\mathbf{x}, t)$ and its spatial derivatives. In case of steady basic flows, the separability between time- and space coordinates in (2.2) permits introducing a Fourier decomposition in time,

$$\tilde{\mathbf{q}} = \hat{\mathbf{q}}e^{\mathrm{i}\Theta}, \tag{2.3}$$

with Θ a phase function, leading to the generalized matrix eigenvalue problem

$$\mathbf{A}\hat{\mathbf{q}} = \omega\mathbf{B}\hat{\mathbf{q}}. \tag{2.4}$$

Here matrices $\mathbf{A}$ and $\mathbf{B}$ discretize the operators $\mathcal{A}$ and $\mathcal{B}$, respectively, incorporating the boundary conditions; $\hat{\mathbf{q}}(\mathbf{x}; t) = (\hat{\rho}, \hat{u}, \hat{v}, \hat{w}, \hat{T})^T$ is the vector comprising the amplitude functions of linear density, velocity-component and temperature or pressure perturbations. The eigenvalue problem adjoint to (2.4) may also be derived, after suitable definition of an inner product, typically associated with perturbation energy in incompressible [43] and compressible [48] flow, and enforcement of the bi-linear concomitant to zero [49]. Both the direct EVP (2.2) and its associated adjoint describe a *modal* global linear instability scenario, applicable to the dynamic behavior of the linearized equations of motion at the asymptotic limit $t \to \infty$. On the other hand, re-writing (2.2) as

$$\frac{d\tilde{\mathbf{q}}}{dt} = \mathbf{C}\tilde{\mathbf{q}}, \tag{2.5}$$

with $\mathbf{C} = \mathbf{B}^{-1}\mathbf{A}$, the autonomous system (2.5) has the explicit solution

$$\tilde{\mathbf{q}}(t) = e^{\mathbf{C}t}\ \tilde{\mathbf{q}}(0) \equiv \mathbf{\Phi}(t)\tilde{\mathbf{q}}(0). \tag{2.6}$$

Here $\tilde{\mathbf{q}}(0) \equiv \tilde{\mathbf{q}}(t = 0)$, and the matrix exponential, $\mathbf{\Phi}(t) \equiv e^{\mathbf{C}t}$, is known as the *propagator operator* [50]. In addition, attention needs to be paid in case the matrix $\mathbf{B}$ is singular. A solution of the

initial value problem (2.5) distinguishes between the limits $t \to 0$ and $t \to \infty$; while the latter limit may be described by the eigenvalue problem (2.4), growth, σ, of an initial linear perturbation, $\tilde{\mathbf{q}}(0)$, may be computed at all times via

$$\sigma^2 = \frac{\left(e^{\mathbf{C}^* t} e^{\mathbf{C} t} \tilde{\mathbf{q}}(0), \tilde{\mathbf{q}}(0)\right)}{(\tilde{\mathbf{q}}(0), \tilde{\mathbf{q}}(0))} = \frac{(\mathbf{\Phi}^*(t)\mathbf{\Phi}(t)\tilde{\mathbf{q}}(0), \tilde{\mathbf{q}}(0))}{(\tilde{\mathbf{q}}(0), \tilde{\mathbf{q}}(0))}. \tag{2.7}$$

Implicit here is the definition of an inner product, $(\cdot, \cdot)$, and the associated adjoint, $\mathbf{\Phi}^*$ and $\mathbf{C}^*$, of the operator $\mathbf{\Phi}$ and matrix $\mathbf{C}$, respectively [49]. The discussion is completed by introducing the singular value decomposition (SVD) of the propagator operator

$$\mathbf{\Phi}(t) \equiv e^{\mathbf{C} t} = \mathbf{U}\mathbf{\Sigma}\mathbf{V}^*. \tag{2.8}$$

Here the unitary matrices $\mathbf{V}$ and $\mathbf{U}$ respectively comprise (as their column vectors) initial and final states, as transformed by the action of the propagator operator, while $\mathbf{\Sigma}$ is diagonal and contains the growth σ associated with each initial state as the corresponding singular value. Given that (2.8) may be formed at all times t, without the need to introduce modal perturbations in this coordinate, the framework in which global linear analysis is performed in this context is referred to as *non-modal*, solution of (2.7) permitting study of both modal- and non-modal perturbation growth. Note also that the operator $\mathbf{\Phi}^*\mathbf{\Phi}$ appearing in (2.7) is symmetric, which has important consequences both for its computation and in relation with the interpretation of its results.

In case the basic flow has an arbitrary time-dependence, the propagator operator, $\mathbf{\Phi}(t)$, may also be defined [51] and (2.6) may be generalized as

$$\tilde{\mathbf{q}}(t_0 + \tau) = \mathbf{\Phi}(\tau)\ \tilde{\mathbf{q}}(t_0). \tag{2.9}$$

The propagator may be understood as the operator evolving the small-amplitude perturbation from its state at time t_0 to a new state at time $t_0 + \tau$. If the time-dependence of the basic state is periodic, $\forall t_0 : \bar{\mathbf{q}}(\mathbf{x}; t_0 + T) = \bar{\mathbf{q}}(\mathbf{x}; t_0)$, the propagator is denoted as the *monodromy operator* and it is also $T-$periodic, $\mathbf{\Phi}(t_0 + T) = \mathbf{\Phi}(t_0)$; the monodromy operator is defined by [52]

$$\mathbf{\Phi} = \exp\left[\int_{t_0}^{t_0+T} \mathbf{C}\left(\bar{\mathbf{q}}(\mathbf{x}; t')\right) dt'\right]. \tag{2.10}$$

Solutions to the instability problem, indicating the development of small-amplitude perturbations during one period of evolution, are obtained through Floquet theory, which seeks the eigenvalues of the monodromy operator, also known as Floquet multipliers [53], γ. To this end, the monodromy operator is evaluated at a time T and the eigenvalue problem

$$\mathbf{\Phi}(T)\hat{\mathbf{q}} = \gamma\hat{\mathbf{q}} \tag{2.11}$$

is solved. The Floquet multipliers can also be expressed in terms of the Floquet exponents, δ, as $\gamma = e^{\delta T}$, which identifies $|\gamma| = 1$ as a bifurcation point and indicates that

$$|\gamma| < 1: \quad \text{periodic} - \text{flow stability}, \tag{2.12}$$

$$|\gamma| > 1: \quad \text{periodic} - \text{flow instability}. \tag{2.13}$$

Barkley *et al.* [16] provide an up-to-date description of global instability analysis of time-periodic flows, with special focus on non-modal analysis and recovery of optimal (global) disturbances arising from localized regions of classic linear (local) instability. The discussion is completed by reference to the dimensionality of the basic state and the ensuing global instability analysis methodologies.

2.1.1 Modal Theory: Global Modes

In what follows solutions of (2.4) are referred to as *global modes*. Physical interpretation of the quantities appearing in (2.4) depends on whether a (temporal or spatial) BiGlobal or TriGlobal context of analysis is followed.

The key assumption underlying both temporal and spatial BiGlobal instability analysis is that the basic state is spatially-invariant along one spatial direction, say x. In temporal BiGlobal analysis the physical interpretation of quantities appearing in (2.4) is as follows: the wavenumber, α, appearing in Table 2.1, is a real parameter and is related with a periodicity length, L_x, along the homogeneous direction x through $\alpha = 2\pi/L_x$. In a manner analogous with classic LST, the eigenvalue ω is complex, composed of a real part, $\Re\{\omega\}$, which is related with the global mode frequency, and an imaginary part, $\Im\{\omega\}$, which is the temporal amplification rate of the global mode. In spatial BiGlobal analysis ω is a real frequency parameter and the linear EVP (2.4) is re-written as an EVP for the determination of the eigenvalue α. The obtained result $\alpha = \Re\{\alpha\} + i\Im\{\alpha\}$ may be utilized to identify a periodicity length, $L_x = 2\pi/\Re\{\alpha\}$, along the homogeneous spatial direction, x, while $-\Im\{\alpha\}$ is the spatial amplification rate.

Both the spatial discretization and the numerical solution of the global EVP itself in a matrix-forming context are well-documented in several sources (e.g. Ref. [1]) and will not be dwelled upon here. Attention will only be brought upon the fact that temporal BiGlobal theory leads to a linear EVP, while the spatial analog of this theory requires solution of a quadratic eigenvalue problem.

TriGlobal modal linear instability analysis may also be performed by numerical solution of (2.4), whereby the amplitude functions are three-dimensional functions of three inhomogeneous spatial coordinates. The analysis is always temporal, the only parameter being the flow Reynolds number, while the physical interpretation of the real and imaginary parts of the eigenvalue, ω is the same as in classic LST and temporal BiGlobal instability analysis.

Finally, independently of the numerical integrity of the global eigenvalue problem results, the ultimate criterion regarding their relevance to flow analysis is comparison with physical reality. If modal global linear instability results are consistent with those recovered from experiment and DNS (under conditions of natural-, *not* controlled-transition initialization), it may be concluded that modal global linear theory is sufficient to describe amplification of small-amplitude disturbances; otherwise, non-modal global theory must be used.

2.1.2 Non-modal Theory: Optimal Perturbations

The description of small-amplitude perturbation evolution via (2.5-2.8) and instead of monitoring the behavior of perturbations in the $t \to \infty$ limit, as (2.4) does, compute the energy growth of perturbations over a finite-time, τ is addressed in this section for the sake of completeness. The maximum energy growth at that time is defined as

$$G(\tau) \equiv \max_{\hat{\mathbf{q}}(0)} \frac{E(\tau)}{E(0)} = \max_{\hat{\mathbf{q}}(0)} \frac{(\hat{\mathbf{q}}(\tau), \hat{\mathbf{q}}(\tau))}{(\hat{\mathbf{q}}(0), \hat{\mathbf{q}}(0))}, \tag{2.14}$$

a result which already computed in (2.7-2.8). Much like the known situation in classic LST [43], the SVD of the adjoint of the global linear evolution operator times the operator itself, both calculated at a given time τ, also delivers the maximum energy growth that the linear perturbation may experience. As known from classic LST, optimal initial conditions and optimal (global) perturbations may be computed either via the left and right singular vectors of an (appropriately defined norm

of) the evolution operator [50, 51, 43] or via an iterative time- or space-marching of the related direct and adjoint linearized operator [54, 55, 56]. Early examples of global optimal perturbation computations have been demonstrated in the flat-plate boundary layer [57], the backward-facing step [55], stenotic flow [58] and the low-pressure turbine cascade [59], while analysis of optimal perturbations in three inhomogeneous spatial directions has yet to appear in the literature.

Besides its utility in the computation of optimal perturbations, the adjoint linearized operator appears in the definition of the bi-orthogonal eigenfunction system [49, 60], introduced in fluid mechanics in order to study receptivity through projection of an arbitrary initial condition on this flow eigensystem. The flat-plate boundary layer [61] and the plane Poiseuille flow [62] have served as early demonstrators of this idea.

The same idea may be extended in multiple inhomogeneous spatial dimensions: provided accurate descriptions of the direct and adjoint eigensystem are available, an arbitrary initial condition may be projected on the discrete eigenmodes $\hat{\mathbf{q}}$, solutions of (2.4), as a sum-of-eigenmodes [63, 57],

$$\mathbf{q}(\mathbf{x}; s) = \sum_j a_j(s)\hat{\mathbf{q}}(\mathbf{x}), \tag{2.15}$$

where s is the Laplace-transformed time-coordinate, related with the eigenvalue ω through $s = \mathrm{i}\omega$, and the expansion coefficients $a_j(s)$ may be computed from the bi-orthogonal direct/adjoint system using a procedure discussed, e.g., in Ref. [64].

2.1.3 On the relation between numerical residuals and global modes

For the sake of completeness of the presentation that follows, which focuses in extraction of global mode results from transient simulation data or experiment, the residual algorithm (RA) will be summarized next. The key idea of this algorithm is that when time-accurate integration of the equations of motion is started from a random initial condition, if the solution approaches a steady state, the path to the latter is conditioned by the damping of the least stable flow eigenmodes. As such, during the time prior to convergence the residual is governed only by the leading damped linear global mode. Thus, it is possible to extract information about the damping rate and amplitude functions of decaying linear global modes from the transient data of time-accurate integration of the equations of motion towards a steady state. In particular, if the time-accurate integration is close to convergence, then the decomposition (2.1) is valid, being straightforward to obtain:

$$\sigma = \ln \left| \frac{\mathbf{q^t}}{\mathbf{q^{t-\Delta t}}} \right| / \Delta t \approx \frac{d \ln[\mathbf{q^t}]}{dt} \tag{2.16}$$

where $\mathbf{q^t} = |\mathbf{q}(x, y, z, t) - \bar{\mathbf{q}}|$ is obtained from the DNS transient data and σ is identified as the damping ratio corresponding to the global modes. In addition, it is possible to extract amplitude functions and frequency of the global modes, or recover the converged solution from transient data following the same idea; further details may be found in [65, 1].

2.1.4 Strobes (snapshots), Chronoi (times) and Topoi (spaces)

The 1980's and 90's of last century witnessed exciting developments in the field of deterministic description of *coherent structures* of turbulent flows. Application of the Karhunen-Loève theory, also known in different fields of Computational Mechanics as Proper Orthogonal Decomposition

[66] and Principal Component Analysis, permits reduction of large space-time collections of numerical or experimental laminar or turbulent flow fields by solution of an eigenvalue problem for the determination of a small number of eigenmodes known as *K-L, POD* or *empirical eigenmodes*, the latter denomination alluding to the fact that knowledge of the underlying dynamical operator is not necessary for the construction of the empirical eigensystem. Concretely, given a sequence of instantaneous data, $\mathbf{u}_i \equiv \mathbf{u}(\mathbf{x}, t_i)$, one forms the cross-correlation tensor

$$\mathcal{R}(\mathbf{x}, \mathbf{x}^{'}) =< \mathbf{u}(\mathbf{x})\mathbf{v}(\mathbf{x}^{'}) > \tag{2.17}$$

(or auto-correlation tensor, when $u = v$), $\mathcal{R}$ being a compact self-adjoint operator [66], and solves the EVP

$$\int\limits_{\partial\Omega} \mathcal{R}(\mathbf{x}, \mathbf{x}^{'})\boldsymbol{\phi}(\mathbf{x}^{'})d\mathbf{x}^{'} = \lambda\boldsymbol{\phi}(\mathbf{x}) \tag{2.18}$$

in order to determine the empirical eigenmodes, $\boldsymbol{\phi}(\mathbf{x})$. This description has (at least) two major attractive features. First, unlike the global eigenmodes – solutions of (2.4), or the Koopman modes – obtained through solution of (2.26) below, the empirical eigenfunctions are orthogonal, permitting expansion of (nominally) arbitrary fields onto the latter eigensystem. Second, most of the system energy is captured by a relatively small number of empirical eigenfunctions, which forms the basis for subsequent Reduced-Order-Modeling (ROM) efforts for the efficient description of the original system[27].

Sirovich [67] introduced the *method of snapshots* or *method of strobes* in order to simplify calculation of the correlation-tensor-based eigenvalue problem (2.18) in case of short-time samples and highly-resolved data. This is of particular interest to analyzing transitional data, since long time-integration is unnecessary during the linear regime and high spatial resolution is desirable. Of particular interest in the present context is that the simplifying assumptions of spatial homogeneity, invoked in the original works in order to make the problem of calculation of empirical eigenfunctions tractable from a numerical point of view, are not necessary if the snapshots method [67, 68, 69] is used.

Sirovich [67] proceeded to expand the empirical eigenfunctions as linear combinations of the instantaneous flow fields,

$$\boldsymbol{\phi} = \sum_{j=1}^{M} \alpha_j \mathbf{u} \tag{2.19}$$

and arrive at the eigenvalue problem

$$\mathbf{C}\alpha_j = \lambda_j \alpha_j. \tag{2.20}$$

This approach circumvents tedious and impractical for large 3D problems calculation of the kernel (2.17) and is thus substantially more efficient than the original eigenvalue problem since the size of matrix $\mathbf{C}$ depends on the number of realizations (*snapshots* or *strobes*), M, utilized in its construction via

$$C_{jk} = \frac{1}{M}(\mathbf{u}_j, \mathbf{v}_k) \tag{2.21}$$

and not on the original problem dimension. As noted in [69], the empirical eigenfunctions $\boldsymbol{\phi}$ are not themselves coherent structures but may rather be used as the appropriate basis for the decomposition of the coherent structures through decomposition of any flow field into the empirical

eigenfunctions

$$\mathbf{q}(\mathbf{x}) = \sum_j a_j \boldsymbol{\phi_j}(\mathrm{x}). \tag{2.22}$$

While this discussion is equally applicable to BiGlobal and TriGlobal linear instability, in the former context it would be possible to seek empirical eigenfunctions by exploiting translational invariance along the homogeneous direction and further decompose linear perturbations into harmonic functions along the homogeneous- and an inhomogeneous two-dimensional part along the remaining two spatial directions. Rempfer and Fasel [70] argued against such a procedure, reasoning that it conceptually contradicts the idea of a compact coherent structure. Instead, they used the concept of spatio-temporal interchangeability and the bi-orthogonal expansion introduced by Aubry *et al.* [71] to decompose a given flow field as

$$\mathbf{q}(\mathbf{x}, t_j) = \sum_i \zeta_i(t_j)\sigma_i(\mathbf{x}) \tag{2.23}$$

where each time-dependent expansion coefficient, ζ_i, was termed *chronos* (time), while the space-dependent coefficient σ_i was called *topos* (space).

2.1.5 Koopman modes and Dynamic Mode Decomposition

The rather old concept of Koopman operator [72] has been recently introduced to the analysis of fluid flow structures by Rowley et al. [73] and Schmid [74], as a particular class of techniques for nonlinear systems analysis and reduction discussed in the influential work of Mezić [75, 76], in which the Koopman modes are defined. The Koopman operator is a linear operator defined for any nonlinear dynamical system, thus allowing for the spectral analysis of nonlinear flows and flow coherent structures description. The Koopman modes reduce to linear global modes when the dynamical system is governed by the linearized Navier-Stokes operator, while in case of time-periodic flows the Koopman modes reduce to Fourier modes. For the sake of completeness in this section the Dynamic Mode Decomposition (DMD) algorithm presented by Schmid *et al.* [77] is briefly described. The existence of spatial and temporal decomposition concepts open different possibilities of structural analysis with the same tool, however in this paper, attention is focused on temporal analysis.

Given a sequence of $N+1$ instantaneous data $\mathbf{v}_i \equiv \mathbf{v}(\mathbf{x}, t_i)$, two different snapshots matrices can be constructed $V_1^N = \{v(x,t_1), v(x,t_2), ..., v(x,t_N)\}$ (from the first snapshot to the N^{th} snapshot) and $V_2^{N+1} = \{v(x,t_2), v(x,t_3), ..., v(x,t_{N+1})\}$ (from the second snapshot to the $(N+1)^{\text{th}}$ snapshot). It is worth noting that, in a manner analogous to data analyzed by POD, snapshot data may arise either from simulation or experiments; in what follows DNS-obtained results will be employed to apply the algorithm and compare its results with those of global mode analysis based on numerical solution of (2.4).

Assuming a constant linear mapping, A, over the entire snapshot sequence, which in general represents a nonlinear system and connects the flow field v_i with the subsequent flow field v_{i+1}, i.e. $v_{i+1} = \mathbf{A}v_i$, it is possible to formulate the sequence of flow fields as a Krylov sequence,

$$V_2^{N+1} = \mathbf{A}V_1^N. \tag{2.24}$$

Selecting a companion matrix which can be thought of as a projection of A onto the snapshot basis V_1^N Eq. (2.24) can be approximated by

$$V_2^{N+1} \simeq V_1^N \mathbf{S}. \tag{2.25}$$

The idea behind DMD is to first construct $\mathbf{S}$ from the snapshot data and then describe the dynamical process defined by A (and approximated by S) through numerical solution of the eigenvalue problem

$$\mathbf{S}\mu = \lambda\mu, \tag{2.26}$$

where the dynamical modes Φ are the projection of the eigenvectors μ on the snapshot basis V_1^N, $\mathbf{\Phi} = \sum_{j=1} \mu_j (V_1^N)_j$, and the eigenvalues follow the next transformation $\omega = log(\lambda)/\Delta t$, where Δt is the time interval between snapshots.

2.1.6 On the relation between numerical and empirical eigenmodes

The main idea behind comparisons of global, POD and Koopman modes is to investigate the relation between numerical and experimental results since, as opposed to global instability analysis which requires a well-defined steady or time-periodic basic state, both POD and DMD analysis can be applied to either numerical or experimental stationary or time-dependent data. In addition, application of flow topology ideas to global instability analysis results has demonstrated that long-known flow structures, such as the Stall Cells at stall conditions [78] and U-separation associated with adverse-pressure-gradient boundary layer flow on a flat-plate [79], can be related to linear amplification of global modes of the respective flows.

The principal motivation of the application of the Karhunen-Loéve (K-L) theory / Proper Orthogonal Decomposition (POD) to fluid flow has been shown to provide a description of turbulence based on deterministic coherent structures, the latter reconstructed using the empirical eigensystem delivered by K-L/POD analysis [66]. By construction of the operator, this POD analysis identifies the most energetic structures in the flow as POD modes.

Rowley *et al.* [80, 81] extended the combined POD/LST analysis to two inhomogeneous spatial dimensions, studying DNS-obtained compressible flows over open cavity configurations. They demonstrated that a Reduced Order Model could be constructed, based on a relatively small (compared with that required for the DNS) number of POD modes satisfying (2.23). They also compared the spatial structure of the leading POD modes with that of the (then-available) local, parallel LST and observed certain analogies in the two sets of data in the unstable shear-layer region at the open end of the cavity.

In the same direction, recent research by Sengupta *et al.* [82] in the analysis of the flow past a circular cylinder has linked the POD modes and the instability modes of this flow by means of non-nonlinear interactions satisfying the Landau–Stuart–Eckhaus (LSE) equation, and also found qualitative analogies between LST and POD mode results.

Merzari *et al.* [83], applied POD analysis to turbulent flows in geometries using the snapshots method containing a narrow gap, thus extending their earlier global linear instability analysis of the same flows in the laminar regime [84]. These authors provided evidence by comparison of such POD eigenfunctions on the one hand, and results of their earlier BiGlobal instability analysis [84] that the leading POD eigenfunctions of turbulent flow exhibit strong spatial analogies with the amplitude functions of the leading eigenmodes.

Finally, Oberleithner *et al.* [85] recently presented direct comparison of empirical modes and linear stability eigenmodes of swirling-jet flow undergoing vortex breakdown. Besides the by now standard snapshot approach for the calculation of POD eigenmodes [67], these authors employed classic OSE- and PSE-based linear stability analysis and the triple-decomposition [9] concept to

analyze the turbulent data extracted from their experiment. To the authors' knowledge, and reservations from a theoretical point of view aside (regarding the re-construction from non-local data of the global mode, as opposed to performing a PSE-3D or TriGlobal instability analysis), Fig. 18 of Oberleithner *et al.* [85] is the first attempt at comparison and the first conclusive demonstration of excellent agreement between the leading POD and the leading *TriGlobal* global flow eigenmode.

The results of Rowley [80, 81], Sengupta [82], Merzari *et al.* [83] and Oberleithner *et al.* [85] in comparing empirical and global flow eigenmodes in two and three inhomogeneous spatial directions, respectively, demonstrate that such analysis may be feasible. It is certainly also desirable, in the sense that it paves the way to description of the flow by simpler models and, ultimately, to its control. Although speculative a this time, the same successes may both be attributable to the predominance of a single Fourier harmonic in the flow dynamics. It is worth examining how the situation may be different in (complex) flows in which additional frequencies are present, what the dependence of analogous comparisons between leading global and leading POD eigenmodes on the relative significance of the additional frequencies in the overall spectrum is and, ultimately, where may the boundary be defined between phenomena which can be attributed to linear dynamics, as opposed to flows in which consideration of non-linearity is essential.

As far as DMD is concerned, this analysis was applied to a jet in crossflow [74] and the results were compared to the POD analysis and global modes. In particular, they found that the Koopman modes eigenfunction are similar to the POD modes, which describes the most energetic structures. However, the POD modes contains several frequencies while the Koopman modes only have one frequency by construction, therefore they can separate the dynamics of the system more effectively, although the physical interpretation of that decomposition may not be clear. The most interesting result is that the Koopman frequency matches with the shedding frequencies obtained with the DNS. In addition, it is shown that the Koopman modes correctly capture the behavior on the attractor while the global eigenmodes capture only the dynamics in a neighborhood of the unstable fixed point.

The present scarcity of information on all these significant issues on the relation between numerical and empirical eigenmodes, not only in the more interesting from an application point of view turbulent but also in laminar flows, is one of the key reasons to guide future research.

2.1.7 TriGlobal linear modal instability analysis of incompressible flows

The abovementioned concepts are now applied to the three-dimensional dimensionless Navier-Stokes equations of a viscous, incompressible fluid in Cartesian coordinates, that can be written as:

$$\nabla \cdot \mathbf{u} = 0 \tag{2.27}$$

$$\frac{\partial \mathbf{u}}{\partial t} + \mathbf{u} \cdot \nabla \mathbf{u} = -\nabla p + \frac{1}{Re} \nabla^2 \mathbf{u} \tag{2.28}$$

where Re is the Reynolds number based on the corresponding reference velocity and length in the x-direction, $\mathbf{u} = (u, v, w)$ is the velocity vector expressed in Cartesian coordinates (x, y, z) and p is the pressure, with appropriate boundary conditions depending on the physical problem to deal with.

In what follows, the variable $\mathbf{q}$ from last section will be particularized to the divergence-free velocity

$$\mathbf{q}(\mathbf{x}, t) = \mathbf{u}(\mathbf{x}, t)\,. \tag{2.29}$$

The above-mentioned three-dimensional and dimensionless Navier-Stokes equations (2.28) can be written in compact form as:

$$\frac{\partial \mathbf{u}}{\partial t} = \mathbf{f}(\mathbf{u}) \,, \tag{2.30}$$

where $\mathbf{u}$ contains the divergence-free three velocity components in the computational nodes.

Following Theofilis [1] formulation for TriGlobal linear stability of steady base flows, the flow is decomposed in a base flow $\bar{\mathbf{u}}$ and three-dimensional amplitude function of the unsteady small perturbations $\epsilon \mathbf{u}'$ with $\epsilon \ll 1$,

$$\mathbf{u}(x, y, z, t) = \bar{\mathbf{u}}(x, y, z, t) + \epsilon \mathbf{u}'(x, y, z, t). \tag{2.31}$$

A linearized eigenvalue problem can be written taking this assumption into the Navier-Stokes equation (2.30), retaining the $O(\epsilon)$ infinitesimal terms:

$$\frac{\partial \mathbf{u}'}{\partial t} = \frac{\partial \mathbf{f}(\bar{\mathbf{u}})}{\partial \mathbf{u}} \mathbf{u}' \equiv \mathbf{A}\mathbf{u}' \,, \tag{2.32}$$

where $\mathbf{A}$ is the Jacobian matrix of the right hand side of the Navier-Stokes equation. According to the TriGlobal ansatz [86], solution of the equation (2.32) are sought as eigenmodes:

$$\mathbf{u}'(x, y, z, t) = \hat{\mathbf{u}}(x, y, z) \mathrm{e}^{\lambda t} + c.c. \tag{2.33}$$

where $\lambda = \lambda_r + i \cdot \lambda_i$, with λ_i representing a frequency and λ_r being the amplification/damping rate of the disturbance sought and c.c. the complex conjugate and $\hat{\mathbf{u}}$ are the eigenfunctions. Coupling this modal solution (2.33) into the linearized equation (2.32) leads to the TriGlobal eigenvalue problem

$$\lambda \hat{\mathbf{u}}(x, y, z) = \mathbf{A}\hat{\mathbf{u}}(x, y, z) \,. \tag{2.34}$$

which efficient numerical solution is the objective of this thesis. Finally, given the temporal context of the TriGlobal analysis, it needs to be noticed the change of variable in phase function Θ respect equation (2.3), in which $\lambda = i\omega$.

Chapter 3

Direct Numerical Simulation

As it has been anticipated in the previous Chapter 2 and will be explained in detail in Chapter 4, the numerical method for the solution of the TriGlobal eigenvalue problem described in this thesis is based on the time-accurate solution of the Navier-Stokes equations. The employed solvers for the direct numerical simulation are described next.

3.1 Compressible Flow

3.1.1 Finite Volume Method (BERTA)

BERTA [87, 88] is a Finite Volume solver developed at the National Institute for Aerospace Technology "Esteban Terradas" (INTA). The code presents an edge-based data structure, which allows the obtention of numerical solutions of compressible Euler and Navier-Stokes equations independently of the selected mesh type to discretize the computational domain. Based on this data structure a complete solution technique has been formulated, which allows to handle structured grids, block structured grids, and unstructured grids of tetrahedra or mixed elements without any modification. This methodology provides to the code a *grid-transparent* property. The advantage of this code lies in the possibility of directly extract the needed information to solve the equations from the geometric data of the mesh. The extraction is achieved by means of a pre-process where a new *linear* structure is build, allocating original geometric data to the mesh edges, subsequent references to the original grid are not needed. The entire compressible viscous Navier-Stokes equation are written in conservative form as:

$$\frac{\partial U}{\partial t} + \frac{\partial f}{\partial x} + \frac{\partial g}{\partial y} + \frac{\partial h}{\partial z} = \frac{\partial F}{\partial x} + \frac{\partial G}{\partial y} + \frac{\partial H}{\partial z}, \tag{3.1}$$

where U is the vector of the conservative flow variables f, g y h are the convective flow vectors F, G y H are the viscous flow vectors.

$$
\begin{gathered}
U = \begin{pmatrix} \rho \\ \rho u \\ \rho v \\ \rho w \\ \rho E \end{pmatrix}, \\
f = \begin{pmatrix} \rho u \\ \rho u^2 + p \\ \rho uv \\ \rho uw \\ \rho uE + up \end{pmatrix}, \quad g = \begin{pmatrix} \rho v \\ \rho vu \\ \rho v^2 + p \\ \rho vw \\ \rho vE + vp \end{pmatrix}, \quad h = \begin{pmatrix} \rho w \\ \rho wu \\ \rho wv \\ \rho w^2 + p \\ \rho wE + wp \end{pmatrix}, \\
F = \begin{pmatrix} 0 \\ \tau_{xx} \\ \tau_{xy} \\ \tau_{xz} \\ u\tau_{xx} + v\tau_{xy} + w\tau_{xz} - q_x \end{pmatrix}, \\
G = \begin{pmatrix} 0 \\ \tau_{yx} \\ \tau_{yy} \\ \tau_{yz} \\ u\tau_{yx} + v\tau_{yy} + w\tau_{yz} - q_y \end{pmatrix}, \\
H = \begin{pmatrix} 0 \\ \tau_{zx} \\ \tau_{zy} \\ \tau_{zz} \\ u\tau_{zx} + v\tau_{zy} + w\tau_{zz} - q_z \end{pmatrix}.
\end{gathered}
\tag{3.2}
$$

The equation system (3.1) can be written in a compact form by introducing the flux vectors:

$$
\begin{gathered}
\frac{\partial U}{\partial t} + \nabla . \overrightarrow{F_c}(U) = \nabla . \overrightarrow{F_v}(U), \\
\overrightarrow{F}_c = f\,\overrightarrow{i} + g\,\overrightarrow{j} + h\,\overrightarrow{k}\,, \\
\overrightarrow{F}_v = F\,\overrightarrow{i} + G\,\overrightarrow{j} + H\,\overrightarrow{k}\,,
\end{gathered}
\tag{3.3}
$$

being $\overrightarrow{F}_c$ y $\overrightarrow{F}_v$ the convective and viscous flux respectively. From a global instability point of view, this set of equations can also be written in the sense of equation (2.30) as:

$$
\frac{\partial U}{\partial t} = F(U)\,. \tag{3.4}
$$

Integrating the system over a control volume V with a control surface S and applying Gauss theorem it can be obtained that:

$$
\frac{\partial}{\partial t} \int\int\int_V U dV + \int\int_S \overrightarrow{F_c} . \overrightarrow{n}\, dS = \int\int_S \overrightarrow{F_v} . \overrightarrow{n}\, dS, \tag{3.5}
$$

where $\overrightarrow{n} = (n_x, n_y, n_z)$ is the vector normal to the surface S at each point.

A finite-volume scheme, in which the flow variables are stored at the vertices of the mesh, has been used for the discretization of the equations. The basic spatial discretization is formed using a central difference finite-volume scheme so the equation (3.5) can be written is discrete form for a control volume V_0 as:

$$\frac{d}{dt}(V_0 U) + \sum_i Q_{ci} = \sum_i Q_{vi}, \tag{3.6}$$

and the balance of convective flux is given by:

$$Q_c = \sum_i Q_{ci} = \sum_i \overrightarrow{F}_{ci} . \overrightarrow{S}_i, \tag{3.7}$$

where the sum is carried out on each surface of the contour of control volume around node i. Finally, this resulting discretized equations form a set coupled ordinary differential equations which are integrated in time using a multi-stage time-stepping scheme.

3.2 Incompressible Flow

3.2.1 Finite Volumes Method (OpenFOAM)

Direct numerical simulations have been performed using the transient incompressible solver of the Navier–Stokes equations of the open-source finite-volume code OpenFOAM®(Open source Field Operation And Manipulation), named *icoFoam*. The employed finite-volume formulation is analogous to the one explained in section (3.1.1) and thus is not detailed here. This solver uses a PISO[89, 90, 91] (Pressure Implicit with Splitting of Operators) velocity-pressure coupling approach to solve the Navier–Stokes equations. A GAMG (Geometric Algebraic Multi Grid) iterative method is used for the solution of the pressure equation while the momentum equations are solved using a preconditioned bi-conjugate gradient (Bi-CGSTAB [92]) . Linear interpolation is used for the volume flux calculations and the equations are advanced in time using a Crank-Nicholson scheme. A high quality performance of this solver has been already demonstrated by several authors in the literature, e.g. Sanmiguel-Rojas et al. [93] or Bohorquez et al. [94, 95], who investigated the instabilities of laminar wakes behind slender axisymmetric configurations.

3.2.2 Spectral Collocation Method (SCM)

A spectral collocation technique [96] have been used in order to compare instability results obtained with high-order methods to the ones obtained with second-order methods. This methodology permits the computation of the incompressible Navier-Stokes steady problem by the time-advancement of a linear system problem where the explicit terms are updated in every time step. The differentiation matrix is based on a rectangular Jacobi-Gauss-Lobatto grid defined by

$$\mathcal{D} = [d^1_{i,j}], \quad d^1_{i,j} = h^1_j(x_i)\,. \tag{3.8}$$

The expression of the coefficients $d^p_{i,j}$ can be found in Canuto [96] or Boyd [97]

$$(d^1)_{i,j} = \begin{cases} \frac{\hat{c}_i}{\hat{c}_j}\frac{(-1)^{i+j}}{(x_i-x_j)} & \text{if } 0 \le i,j \le N, i \ne j \\ -\frac{x_i}{2(1-x_i^2)} & \text{if } 1 \le i = j \le N-, i \ne j \\ \frac{2N^2+1}{6} & \text{if } 0 = i = j \\ -\frac{2N^2+1}{6} & \text{if } i = j = N \end{cases} \tag{3.9}$$

The way to define the differential matrices in 2-D is to use tensor products, also known as Kronecker product denoted by $\otimes$. If $\mathcal{D}_x^1$ represents the $(N_x+1)^2$ first derivative matrix in x and $\mathcal{D}_y^1$ the $(N_y+1)^2$ first derivative matrix in y direction, then $\hat{\mathcal{D}}_x^{(1)} = \mathcal{I}\otimes\mathcal{D}_x^{(1)}$ and $\hat{\mathcal{D}}_y^{(1)} = \mathcal{D}_y^{(1)}\otimes\mathcal{I}$ where $\mathcal{I}$ is the $(N_y+1)^2$ or $(N_x+1)^2$ respectively identity matrix, are the $[(N_x+1)\times(N_y+1)]^2$ 2-D derivatives matrices in x and y direction.

Using the spectral collocation method as spatial scheme, the chosen temporal scheme is the SMR proposed by Spalart et al. [98]. This SMR algorithm may be written in compact form as

$$q^{'''} = q^{''} + \Delta t\Big\{\mathcal{L}(\kappa q^{''} + \lambda q^{'''}) + \mu\mathcal{N}(q^{''}) + \nu\mathcal{N}(q^{'})\Big\}, \tag{3.10}$$

where the superscript denotes fractional time–step, $\mathcal{L}(q)$ and $\mathcal{N}(q)$ are, respectively, the linear and nonlinear operators in the problem to be solved and Δt is the time–step. The rationale behind the derivation as well as sample values of the constants κ, λ, μ and ν of a self–starting algorithm may be found in the original reference[98]. Explicitly, the operators are

$$\mathcal{L} = \frac{1}{Re}\left(\frac{\partial^2}{\partial x^2} + \frac{\partial^2}{\partial y^2}\right)\zeta - \lambda_f(x)(\zeta - Z) \tag{3.11}$$

$$\mathcal{N} = -(\psi_y\zeta_x - \psi_x\zeta_y). \tag{3.12}$$

Applying (3.10) delivers the problem to be solved for (ζ, ψ) at each fractional time–step,

$$\mathcal{M}_1\ \psi^{'''} + \zeta^{'''} = 0, \tag{3.13}$$

$$\mathcal{M}_2\ \zeta^{'''} = \mathcal{R}_2. \tag{3.14}$$

Here

$$\mathcal{M}_1 = \partial_{xx} + \partial_{yy}, \tag{3.15}$$

$$\mathcal{M}_2 = \partial_{xx} + \partial_{yy} - Re\left(\frac{1}{\lambda\Delta t} + \lambda_f\right), \tag{3.16}$$

$$\begin{aligned} \mathcal{R}_2 = & -Re\ \lambda_f\ \left(1 + \frac{\kappa}{\lambda}\right)\ Z \\ & -\frac{\kappa}{\lambda}\left[\zeta_{xx}^{''} + \zeta_{yy}^{''} + Re\ \left(\frac{1}{\kappa\Delta t} - \lambda_f\right)\zeta^{''}\right] \\ & +\frac{\mu Re}{\lambda}\left(\psi_y^{''}\zeta_x^{''} - \psi_x^{''}\zeta_y^{''}\right) \\ & +\frac{\nu Re}{\lambda}\left(\psi_y^{'}\zeta_x^{'} - \psi_x^{'}\zeta_y^{'}\right), \end{aligned} \tag{3.17}$$

After applying proper boundary conditions, these two equations can be written as:

$$\left(\frac{\partial^2}{\partial x^2}+\frac{\partial^2}{\partial y^2}+c\right)q = RHS \tag{3.18}$$

where the right hand side contains the independent term form boundary conditions. Because the constant time step, the derivative matrix can be diagonalized as:

$$M^{-1}\mu_{ii}Mq + qN^{-1}\nu_{ii}Nq + cq = RHS \tag{3.19}$$

where M and Ncontains the eigenvectors and μ and ν are the corresponding eigenvalues. By multiplying by M and post-multiplying by N^{-1} and introducing the transformed variable $\hat{\mathbf{q}} = MqN^{-1}$, the equations can be written in a set of algebraic equations as:

$$\hat{\mathbf{q}}_{ij} = \frac{R\hat{H}S}{\mu_{ii}+\nu_{ii}+c}\,. \tag{3.20}$$

The complete implementation of the code is described in detail in the Appendix A of the work of Theofilis [99].

3.2.3 Spectral Elements Methods (Semtex)

Finally, for the sake of studying complex geometries while maintaining a high-order scheme, the Semtex code [38] has been employed. Semtex is a DNS code based on spectral element formulation, which combines the geometric flexibility of finite elements with the high accuracy of spectral methods, that solves the incompressible Navier–Stokes equations in primitive variables. Standard nodal Gauss–Lobatto–Legendre basis functions are used in two inhomogeneous directions while a Fourier expansions is used in the other one, for three-dimensional problems, that is assumed homogeneous. More specifically, the domain is divide into blocks and these in quadrilateral obtained by using continuous Galerkin projection from a canonical domain, $[-1,1]\times[-1,1]$. The nodes on each direction are obtained from the zeros of Legendre polynomials. These are generalized to two-dimensional problems by using tensor-product interpolants of one-dimensional grids distribution as done with the Spectral Collocation Method in Section (3.2.2). Finally time integration employs a backwards-time differencing scheme described by [100]. This code has been validated and used in a number of works, see [101], [102], [103], [104], [38], or [104].

Chapter 4

Numerical Solution of the Eigenvalue Problem using Time-stepping

4.1 Eigenspectrum Computation

4.1.1 QR algorithm

The QR algorithm is a iterative procedure to solve an eigenproblem based on performing successive QR decompositions of the Jacobian matrix until a Schur decomposition of the eigenvalue problem is achieved. This reads,

$$\mathbf{AQ} = \mathbf{QR} \tag{4.1}$$

where $\mathbf{Q}$ contains a orthonormal basis of the invariant subspace of matrix $\mathbf{A}$ and $\mathbf{R}$ is an upper triangular matrix. Once the Schur decomposition of $\mathbf{A}$ is known, the eigenvector can be computed by different methods, as inverse iteration. The most important feature of this procedure is that the matrix need to be formed explicitly, so it is constrained by computational resources. Therefore the Jacobian matrix associated with a TriGlobal problem cannot be computed with this algorithm and an alternative method in which the order of the matrix is reduced must be sought.

4.1.2 Krylov-subspace methods: Arnoldi algorithm

Projection methods are the algorithm of choice to reduce the order of the eigenvalue problem. The most popular Krylov-subspace projection-iterative methods follow the classic Arnoldi [2, 3] algorithm, which consists of the generation of a Krylov subspace and its orthonormalization in order to create a reduced matrix that contains a finite but small number of eigenvalues (equal to the Krylov subspace dimension) m of the original Jacobian matrix. An orthonormal base $\mathbf{U}$ of a m-dimensional Krylov subspace is generated with an initial vector and successive applications of the Jacobian matrix following a Gram-Schmidt orthonormalization step. Projecting the Jacobian matrix into this orthonormal basis, it can be approximated that:

$$\mathbf{AU} \sim \mathbf{UH}\,, \tag{4.2}$$

where $\mathbf{H}$ is a $m \times m$ Hessenberg matrix obtained via Gram-Schmidt that contains an approximation of the eigenvalues of the Jacobian matrix $\mathbf{A}$. Performing an eigenvalue decomposition of the Hes-

senberg matrix $\mathbf{H} = \mathbf{D\Lambda D^{-1}}$ via a QR algorithm as explained in the previous subsection 4.1.1 it can be written that:

$$\mathbf{A} \sim \mathbf{UD\Lambda D^{-1}U^{T}}, \tag{4.3}$$

being **UD** approximations of the eigenfunctions or global modes and the eigenvalues of the diagonal matrix $\mathbf{\Lambda}$ approximations of the eigenvalues of the Jacobian matrix **A**. The complete Arnoldi method is detailed in Algorithm 1.

Algorithm 1 Arnoldi Iteration

S1. Initial Condition: Set u_0, m

S2. Arnoldi iteration: Perform until convergence $(l = 1, ..., m)$,

- **A1. Apply Operator:** $\mathbf{u'_l = Au'_{l-1}}$
- **A2. Gram-Schmidt:** $(i = 1, ..., l)$
  - **GS1.** Form Hessenberg matrix $h_{il} = \mathbf{u'}_i^T \mathbf{Au'_l}$
  - **GS2.** Orthogonalize $\mathbf{u'}_{l+1} = \mathbf{Au'_l} - \sum_{\mathbf{i=1}}^{\mathbf{j}} \mathbf{h_{il}u'_i}$
  - **GS3.** Normalize $h_{l+1,l} = \|\mathbf{u'}_{l+1}\|$, $\mathbf{u'}_{l+1} = \frac{\mathbf{u'}_{l+1}}{h_{l+1,l}}$

S3. QR: Perform eigenvalue decomposition of the $m \times m$ matrix **H**

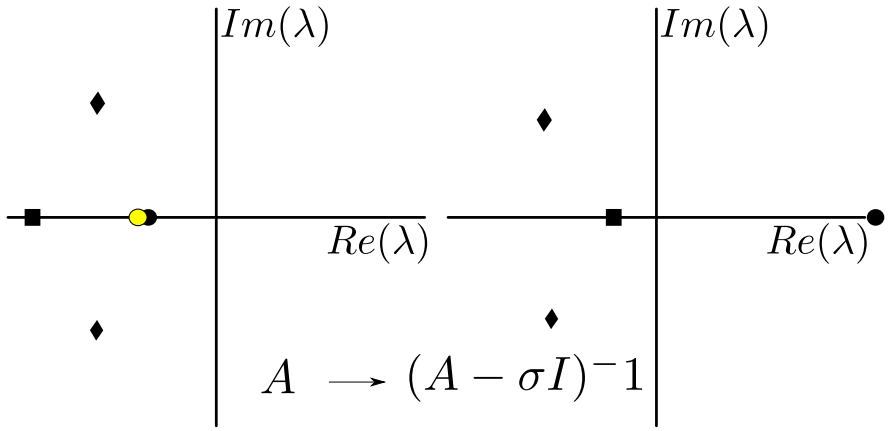

Figure 4.1: Shift-Invert transformation. Yellow circle indicates shifting value σ.

As it was anticipated in the introduction, due to the successive application of the Jacobian operator, the Arnoldi method only can recover a subset of dominant eigenvalues, which are the ones with largest modulus. Thus a transformation of the spectrum is required in order to recover the leading eigenvalues (smallest real part), which linear growth is responsible of the hydrodynamic instabilities. Figure (4.1) represents the commonly employed shift-and-invert strategy [4] for matrix-forming strategies, in which the whole matrix is inverted using a LU decomposition. In this figure the leading eigenvalue (circle) tends to infinity in the transformed spectrum due to the near shift, while the dominant eigenvalues remains in the stable half plane of the shifted and inverted spectrum.

However, the necessity of the the formation of the Jacobian matrix is not explicit in the Arnoldi algorithm and only Jacobian-matrix vector products are required to complete the algorithm. This characteristic is exploited in the present methodology by using a temporal or exponential transformation [5, 20] and will be explained next.

4.2 Jacobian-free Newton–Krylov methods

By following the Newton Iteration, which is equivalent to apply a Taylor series expansion to the Navier-Stokes equation around the steady base flow $\bar{\mathbf{u}}$ and considering that the second and higher order terms with respect to $\epsilon\mathbf{u}'$ are negligible small, it can be written that

$$\mathbf{f}(\bar{\mathbf{u}} + \epsilon\mathbf{u}') = \mathbf{f}(\bar{\mathbf{u}}) + \frac{\partial \mathbf{f}(\bar{\mathbf{u}})}{\partial \mathbf{u}}\epsilon\mathbf{u}' + O(\epsilon^2)\,, \tag{4.4}$$

and a Jacobian-vector product can be then obtained means of:

$$\frac{\partial \mathbf{f}(\bar{\mathbf{u}})}{\partial \mathbf{u}}\mathbf{u}' \approx \frac{\mathbf{f}(\bar{\mathbf{u}} + \epsilon\mathbf{u}') - \mathbf{f}(\bar{\mathbf{u}})}{\epsilon}\,. \tag{4.5}$$

This equation is also known as a Frèchet derivative [105] and it provides the Jacobian-vector product by the sum of two vectors corresponding to the right hand side of the Navier-Stokes equations. High order Frèchet derivatives can be created by increasing the stencil. The coupling of this Frèchet derivative or Newton Iteration with Krylov subspace projection-iterative methods are known as Jacobian-free Newton Krylov [106] (JFNK) methods.

4.3 Exponential Time-Stepping Transformation using full DNS

The present methodology is based on Chiba's approach [17, 107], which links a Jacobian-free Newton Krylov method[106] that follows the classic Arnoldi [3] algorithm, with a temporal exponential transformation of the spectrum. This spectrum transformation is required for the conversion of the leading eigenvalues into the dominant eigenvalues, which are the ones that the Arnoldi method can recover. Integrating the linearized equation (2.32) over a τ time and using the TriGlobal ansatz (2.33) lead to the exponential of the eigenvalue problem:

$$e^{\lambda}\hat{\mathbf{u}} = \mathbf{e}^{\mathbf{At}}\hat{\mathbf{u}}\,. \tag{4.6}$$

which spectrum correspond to the exponential of the original Jacobian matrix. Figure (4.2) represents the temporal exponential transformation of the spectrum. In this figure it can be seen how the leading eigenvalue of the Jacobian matrix (circle) becomes the dominant in the spectrum of the exponential of the Jacobian matrix. At the same time, the dominant eigenvalues are shifted to zero.

Therefore, the eigenvalue solution can be obtained now following the Arnoldi method, with the particularity of substituting the Jacobian operator $\mathbf{A}$ with its exponential $e^{\mathbf{At}}$. Integrating a τ time the original Frèchet derivative (4.5) and recalling the linearized Navier-Stoke equation (2.32), the exponential of the Frèchet derivative can be written as:

$$e^{\mathbf{At}}\mathbf{u}' \approx \frac{\int_0^t (\mathbf{f}(\bar{\mathbf{u}} + \epsilon\mathbf{u}') - \mathbf{f}(\bar{\mathbf{u}}))\mathrm{d}t}{\epsilon}, \tag{4.7}$$

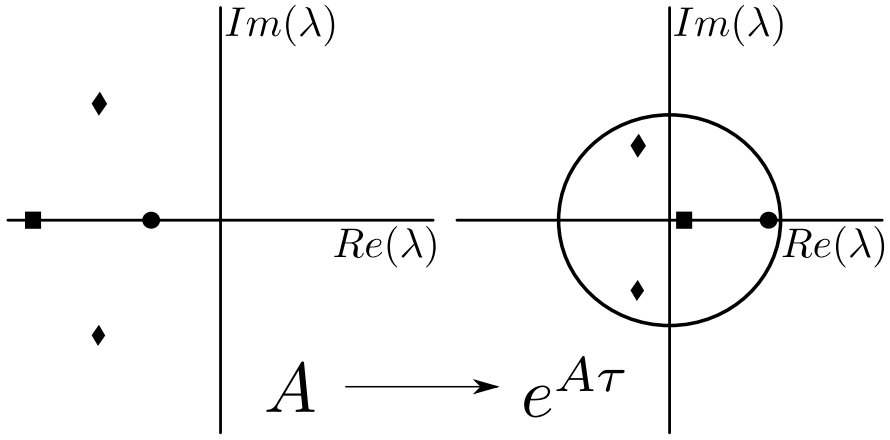

Figure 4.2: Temporal exponential transformation

which provides the exponential of the Jacobian-vector product by the sum of two vector obtained by the temporal integration of the non-linear DNS.

The major algorithmic contribution of this thesis to this methodology is to take into account that *any* non-linear DNS can be used in a *black-box* context to provide the matrix-vector products required for the stability problem. From an algorithmic point view, this means that the stability and DNS problems can be treated in separate ways and it is possible to easily couple the present stability algorithm with any DNS, without modifying the solver in any aspect. Using OpenFOAM® along with the previous descriptions of JFNK methods following the Arnoldi iteration and temporal exponential transformations, the algorithm can be detailed as:

Algorithm 2 Instability analysis with full Navier–Stokes

S1. Initial Condition: Set m and ϵ and $\mathbf{u}'_1$

S2. Arnoldi iteration: Perform until convergence $(l = 1, ..., m)$,

- **A1. Call DNS:** $\mathbf{u_{l+}} = \bar{\mathbf{u}}(\tau) + \epsilon \mathbf{u}'_l(\tau)$ and $\mathbf{u_{l-}} = \bar{\mathbf{u}}(\tau) - \epsilon \mathbf{u}'_l(\tau)$
- **A2. Frèchet derivative:** $e^{\mathbf{A}\tau}\mathbf{u}'_l = \frac{\mathbf{u_{j+}} - \mathbf{u_{j-}}}{2\epsilon}$
- **A3. Gram-Schmidt:** $(i = 1, ..., l)$
  - **GS1.** Form Hessenberg matrix $h_{il} = \mathbf{u}'^T_i e^{\mathbf{A}\tau}\mathbf{u}'_l$
  - **GS2.** Orthogonalize $\mathbf{u}'_{l+1} = e^{\mathbf{A}\tau}\mathbf{u}'_l - \sum_{i=1}^{j} h_{il}\mathbf{u}'_i$
  - **GS3.** Normalize $h_{l+1,l} = \|\mathbf{u}'_{l+1}\|$, $\mathbf{u}'_{l+1} = \frac{\mathbf{u}'_{l+1}}{h_{l+1,l}}$

S3. QR: Perform eigenvalue decomposition of the $m \times m$ matrix $\mathbf{H}$

S4. Undo exponential transformation

Figure (4.3) shows the flux diagram of the present algorithm steps coupled with the incompressible solver *icoFoam* of OpenFOAM®, where only the I/O routines need to be modified for a change

of DNS solver. Unless explicitly remarked, this methodology will be used throughout in this thesis.

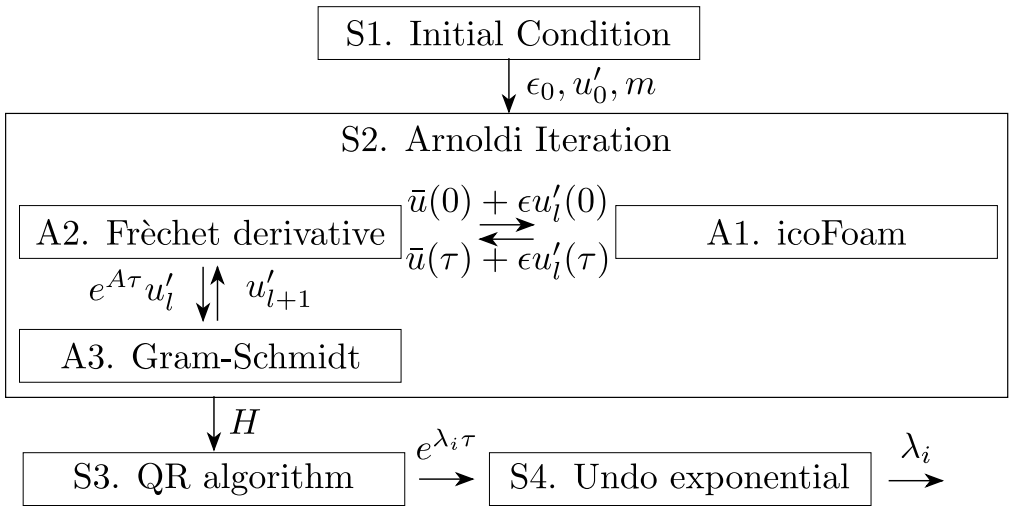

Figure 4.3: Flux diagram of the proposed algorithm (left) instability routines (middle) auxiliary routines (right) DNS routines

4.4 Exponential Time-Stepping Transformation using LNSE

Is is very interesting to remark that if instead of the full Navier–Stokes equations, the linearized Navier-Stokes equations (LNSE) (2.32) are to be solved, the linearization step via Frèchet derivative (4.7) is unnecessary and the algorithm becomes the classical time-stepping strategy [22]. The advantage of this method against the exponential time-stepping transformation using full Navier–Stokes is that the temporal integration only needs to be carried out once for the same resolution, so the method is twice as fast with the same computational requirements. However, the availability of this method is subject to the accessibility of the source code non-linear Navier–Stokes solver and, ultimately, its capacity to be modified in order to solve the temporal evolution of the linearized Navier-Stokes equations exploiting its spatial and temporal numerical schemes. Moreover, this methodology permits the instability analysis of unstable steady-state flows.

4.4.1 Improving the algorithm: Shift-Invert Exponential Transformation

The above mentioned exponential time-stepping matrix-free [5, 106] can be slow and computationally expensive in terms of CPU time [22, 108] when eigenvalues close to the imaginary axis need to be studied. In order to accelerate the procedure to obtain such eigenvalues, an analogous technique to the shift-and-invert strategy used in the approach in which the matrix is formed can be applied to the time-stepping methods; this idea was first proposed by Goldhirsch et al. [109] in a local instability analysis context and more recently by Tuckerman [22] for the case of bifurcation analysis using inverse matrix-free strategies.

In particular, Tuckerman [22] proposed using the inverse of the Jacobian in a matrix-free framework in order to obtain the eigenvalues close to the imaginary axis without spectrum transformation.

Algorithm 3 Instability analysis with LNSE

S1. Initial Condition: Set m and $\mathbf{u}'_1$

S2. Arnoldi iteration: Perform until convergence $(l = 1, ..., m)$,

A1. Call LNSE: $\mathbf{u}'_l \leftarrow e^{\mathbf{A}\tau}\mathbf{u}'_l$

A2. Gram-Schmidt: $(i = 1, ..., l)$

GS1. Form Hessenberg matrix $h_{il} = \mathbf{u}'^T_i e^{\mathbf{A}\tau}\mathbf{u}'_l$

GS2. Orthogonalize $\mathbf{u}'_{l+1} = e^{\mathbf{A}\tau}\mathbf{u}'_l - \sum_{i=1}^{j} h_{il}\mathbf{u}'_i$

GS3. Normalize $h_{l+1,l} = \|\mathbf{u}'_{l+1}\|$, $\mathbf{u}'_{l+1} = \frac{\mathbf{u}'_{l+1}}{h_{l+1,l}}$

S3. QR: Perform eigenvalue decomposition of the $m \times m$ matrix $\mathbf{H}$

S4. Undo exponential transformation

The effect of the inverse Jacobian operator can be applied by means of an iterative procedure, such as the Bi-Conjugate Gradient Stabilized algorithm [92] (Bi-CGSTAB). However, while the evaluation on the inverse of the Jacobian can be carried out in a efficient way in a matrix-forming context by means of a full LU decomposition, the iterative algorithm can be very slow or even not guarantee convergence in a matrix-free framework [110]. A preconditioner based on the Stokes operator can be used to accelerate this iterative procedure, but such preconditioner cannot be directly applied to any time-stepping in a generic way, as shown by Mack & Schmidt [24] who successfully resolved this issue for compressible flows by using a Caley transformation [33], applying a low-order inverse Jacobian as an explicit preconditioner matrix. This subsection describes a improvement of the previous methodology that accelerate and allows access to specific part of the linear global eigenspectrum. This new methodology is based on a shift transformation plus the application of the exponential of the inverse Jacobian matrix by means of the time-stepper and, following the spirit of the exponential time-stepping transformation using full DNS method, it can be directly applied to any time-stepper, regardless of its temporal or spatial discretization. Figure (4.4) sketches the transformation step by step, in which it is seen that as a results the leading eigenvalue tends to infinity in the transformed eigenspectrum.

The algorithm consists of two iterations: the outer Arnoldi iteration [110], and a inner iteration for the inversion of the exponential if the operator. This inversion is achieved using Bi-CGSTAG [92] developed for linear systems that are not symmetric definite. In order to simplify the methodology, reverse communication interfaces for the implicit Arnoldi iteration as implemented in ARPACK [111] were also used. In summary, the following scheme is used in order to obtain the eigenvalues of largest magnitude for the shift-invert problem:

Conjugate gradient iterative methods for non-symmetric definite systems may converge slowly, requiring a large number of iterations when the condition number is high. Preconditioning techniques help improve the convergence of the stability problem, see Knoll and Keyes [106] for a recent overview. The origin of the large condition number is the wide range of eigenvalues of the Laplacian operator and for this reason a Stokes preconditioner is often used (see Tuckerman *et al.* [22]). However, this preconditioner has the disadvantage of not being applicable directly to a real/complex shift-invert time-stepping and a new preconditioner must be used for the problem at hand. In

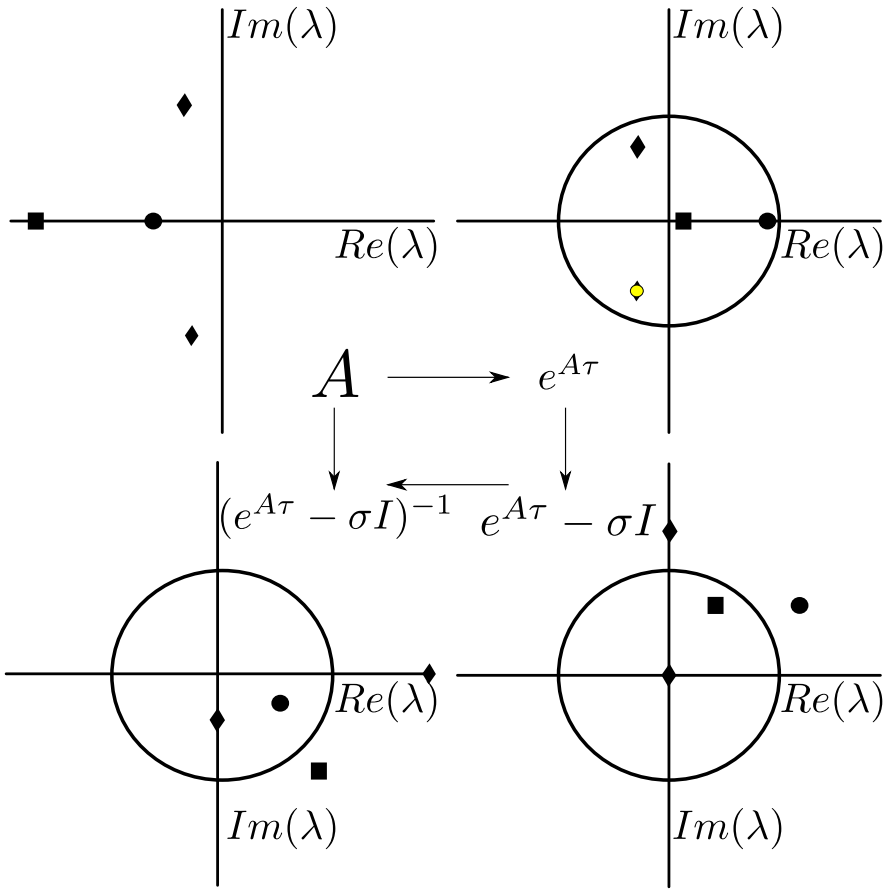

Figure 4.4: Shift-Invert Exponential transformation. Yellow circle indicates shifting value σ.

the present shift-invert methodology, a general approach based on implicit preconditioning, in the sense of improving the condition number of the matrix to invert without explicitly forming a preconditioner matrix is applied by means of the time-stepping, because the Jacobian matrix is not being inverted, instead its matrix exponential is being inverted. Although this preconditioning is only strictly valid for large integration times, since the exponential of the Jacobian matrix of the Navier–Stokes equation is not bounded by the exponential of the eigenvalues at short times because its non-normality, it will be shown that the integrations times used are large enough and that the increments in this integration time significantly improve the number of required iterations for the inversion of the exponential of the Jacobian matrix.

Algorithm 4 Exponential shift-invert algorithm

S1. Initial Condition Set $tol_{Arnoldi}$ (Arnoldi tolerance) and m (maximum number of Arnoldi iterations), $tol_{Bi-CGSTAB}$ (Iterative linear solver tolerance), $N_{Bi-CGSTAB}$ (maximum number iterations used in Bi-CGSTAG), $\mathbf{u}'_0$

S2. Arnoldi outer loop Perform until convergence, $(l = 1, ..., , m)$,

A1: Initialize $\mathbf{u}_l'^{j=0} = 0$ and $\mathbf{r}^{j=0} = \mathbf{u}'_{l-1} - \left(e^{\mathbf{A}\tau} - e^{\sigma}\mathbf{I}\right)\mathbf{u}_l'^{j=0}$, where $\mathbf{r}$ denotes the residual error

A2: Bi-CGSTAB inner loop Perform until convergence, $(j = 1, ..., N_{Bi-CGSTAB})$,

B1: Apply operator $\mathbf{u}_l'^{j} = (e^{\mathbf{A}\tau} - e^{\sigma}\mathbf{I})\mathbf{u}_{l-1}'^{j}$ on an internal vector

B2: Residual Compute $\mathbf{r}^j$

S3. Undo shift-invert exponential transformation

Chapter 5

Validation of Time-Stepping Methodology

5.1 Case study: 2D square lid-driven cavity

First, the instability of a two-dimensional regularized square lid-driven cavity (LDC), which is well-documented [112, 113, 114], has been analyzed using three different methodologies: the finite volume method (FVM) using the BERTA code, the spectral collocation method (SCM), both in a time-stepping (TS) framework, and the solution of the BiGlobal EVP (BG) with a matrix-forming technique. Since the eigenvalue spectrum is well-known in this problem from BiGlobal results, a parameter sweep has been carried out in order to identify the optimum parameters for its recovery in a TS framework.

5.1.1 Parameters selection

One of the most challenging aspects of the proposed time-stepping methodology is the correct selection of parameters. Integration time τ, perturbation magnitude ϵ and subspace dimension m must be selected by the user. This subsection provide guidelines for their adequate selection.

Criteria for the selection of the integration time τ can be found in the the early work of Goldhirsch et al. [109], where it is stated that one of the necessary conditions for the recovery of the eigenvalue λ_i using iterative projection methods is

$$Re|\lambda_i - \lambda_m|\tau \gg 1\,. \tag{5.1}$$

This condition ensures that the eigenvalues sought are enough separated from the rest in the exponential transformation of the spectrum, so they can be recovered with the Arnoldi algorithm, as it was shown in Figure (4.2). Such condition can be achieved either increasing the dimension m of the Krylov subspace by increasing the length of the temporal integration τ. Both options are equivalent in terms of computational effort. If the spectrum of the problem presents significant separation between eigenvalues or gaps, small Krylov spaces can lead to good results. In particular, for this well-known spectrum, $|Re(\lambda_1 - \lambda_{20})|\,\tau \sim 16$. However increasing τ is the best option if the leading eigenvalues of the studied spectrums are close to each other.

Another essential aspect is the control of the perturbation magnitude, since the equations that are being integrated are not linear and the perturbation must remain linear. Knoll & Keyes [106]

and Mack & Schmid [24] review advance techniques in order to do so. Here, the original criteria envisaged by Eriksson and Rizzi [5] and used by Tezuka & Suzuki [19] has proven to be enough effective. Such criteria can be written as

$$\epsilon = \epsilon_0 \frac{||\bar{\mathbf{u}}||}{||\mathbf{u}'||}\,, \tag{5.2}$$

where the constant ϵ_0 represents the initial order of magnitude of the residual of the temporal integration. A value of $\epsilon_0 \sim 10^{-5}$ has proven to be enough for this work. In addition, attention must be paid to the truncation error of the Frèchet derivative, since the order of magnitude of this error ($O(\epsilon^2)$) can be bigger than the residual tolerance of the numerical scheme ϵ_m. This issue can be solved using a second-order Frèchet derivative. Finally, the initial order of magnitude of the perturbation ϵ_0 and the length of the temporal integration τ can be related with the condition that the residual of the integration remains bigger than the residual tolerance of the numerical scheme ϵ_m, which lead to the following condition

$$\epsilon_0 e^{\lambda_1 \tau} > \epsilon_m\,. \tag{5.3}$$

Finally, a upper and lower limit to the length of integration τ can be established taking into account the previous expression and equation (5.1) as

$$\frac{1}{Re(\lambda_i - \lambda_m)} < \tau < \frac{\ln\left(\frac{\epsilon_m}{\epsilon_0}\right)}{\lambda_1}\,. \tag{5.4}$$

This expression also indicates that when left and right side hand of the equation have the same order of magnitude, Krylov subspace dimension needs to be increased.

5.1.2 Validation results

The obtained spectra with three different methods can be seen in Figure 5.1 . Numbers have been assigned to the eigenvalues to aid in their classification. For the BG a 64×64 resolution mesh and Krylov subspace $m = 300$ have been used. SCM results have been obtained with a 64×64 mesh and the FVM with a mesh $\Delta x = 10^{-3}$ and number of nodes $n_{nodes} = 900$. Time-stepping parameters Krylov subspace $m = 60$, non-dimensional integration time $\tau = 10$ and variable ϵ for the SCM and a constant $\epsilon = 10^{-2}$ for the FVM results. In what follows, the results obtained via BG analysis will be taken as reference value.

The most relevant aspect of the spectrum is that, despite the convergence of the TS spectrum has been reached, only a few correct eigenvalues are recovered because of the relatively small Krylov subspace dimension. If more eigenvectors are to be recovered, the Krylov subspace dimension should be increased. In this case, the two less sComparison of average in time C_D drag coefficient between the straked cylinder and the bare cylinder eigenvectors are correctly recovered: λ_1 and λ_3. The eigenvectors corresponding to $\lambda_1 = 0.3322$ can be seen in Figures (5.2) along with their corresponding meshes. The different isolines accurately match in both eigenvectors, except for the one corresponding to $\hat{u} = 0$ or $\hat{v} = 0$, where the numerical error due to the numerical scheme are more evident.

It is remarkable that, despite the problem is two-dimensional, there still exist three-dimensional $\hat{w}$ eigenvector component, for example associated with $\lambda_2 = 0.3979$. This is explained by the fact that the BiGlobal analysis implies a $\alpha \sim 0$ and the FVM code handles the two-dimensional problems

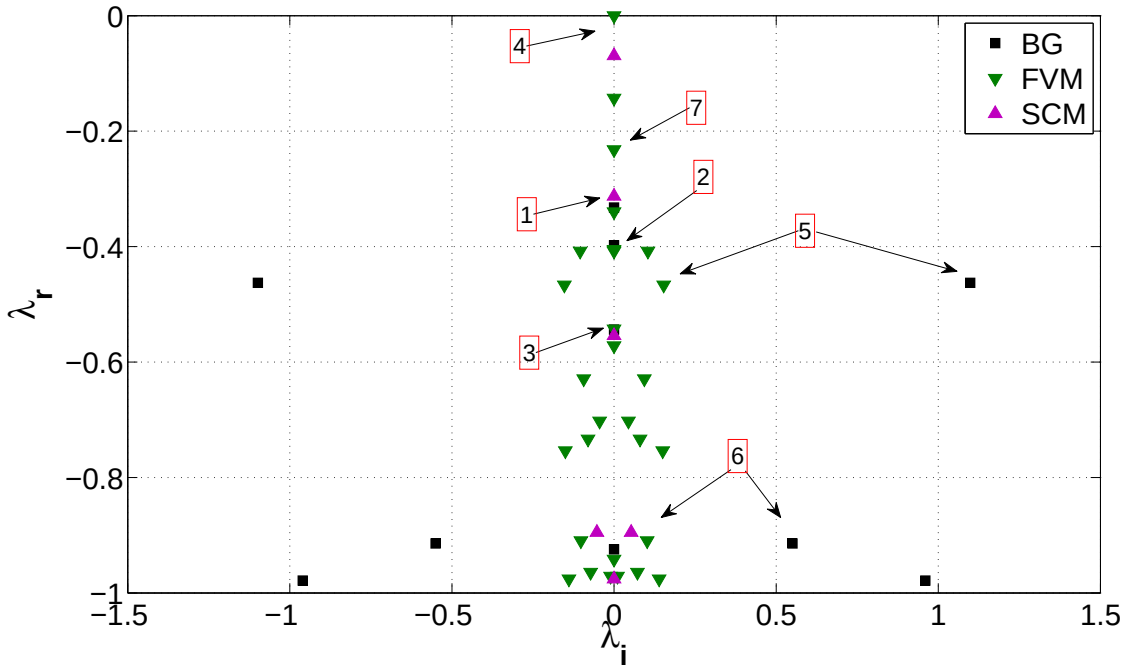

Figure 5.1: Spectrum of the regularized LDC at $Re = 200$ obtained with three different methods. Black squares for BG, upside-down green triangles for FVM and magenta triangles for SCM

by means of periodic boundary conditions in the z coordinate. Obviously, this does not occur in the pure two-dimensional spectral collocation method code. These three-dimensional modes do not need to perfectly match, since the α factor is similar to both codes, but not the same. Another interesting observation is that the base flow can be recovered as a global mode in some cases with $\lambda_4 \sim 0$. This could be explained by the existence of a short $O(1)$ transient during the first time steps of the time-accurate solutions. The FVM spectrum presents additional eigenvalues compared to those recovered by the BG and SCM methods. These additional modes appear due to the compressibility of the FVM method. As observed by Tezuka & Suzuki [19] , another important issue is that an aliasing problem may occur because the complex logarithm is a multi-evaluated function. The recovery of the imaginary part of the eigenvalue from the exponential transformation reads:

$$\lambda_i = i\frac{arg(e^{\lambda_i \tau}) + 2\pi n}{\tau} \tag{5.5}$$

being n any natural number. This means that the frequencies of the modes cannot be correctly recovered without additional help from the DNS. This explains why both the FVM and SCM complex eigenvalues only match the real part of BG results, as it happens with the eigenvalue λ_5. In addition, the use of the compressible FVM scheme adds branch of modes related to the compressibility of the flow as well as numerous spurious modes, as λ_7, which do not appear by using the SCM.

Table 5.1 shows the influence of the integration time τ on the FVM results. It can be seen that, according to the theory, when the integration time is long enough no significant improvement in the

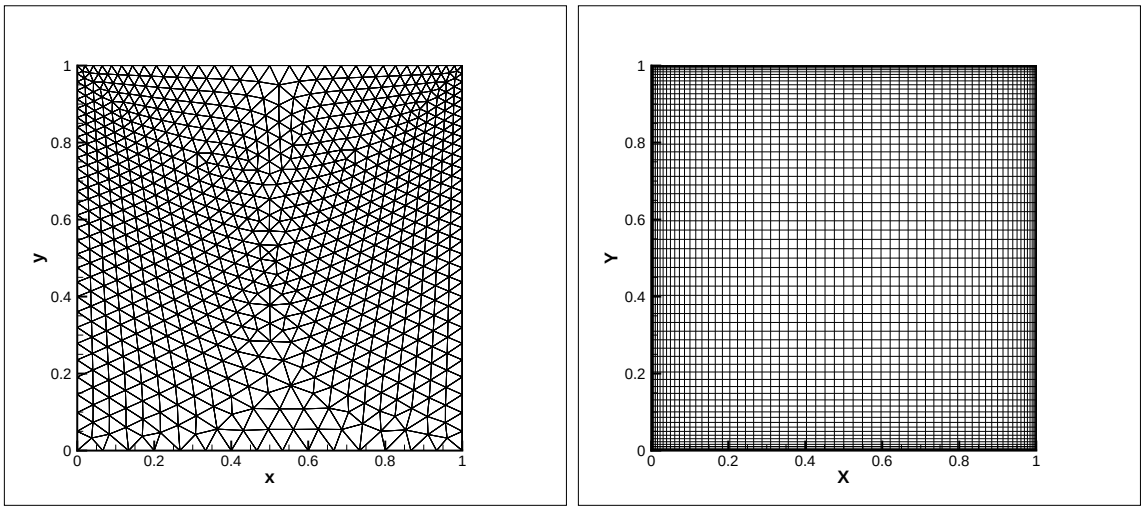

(a) FV Mesh (b) SC Mesh

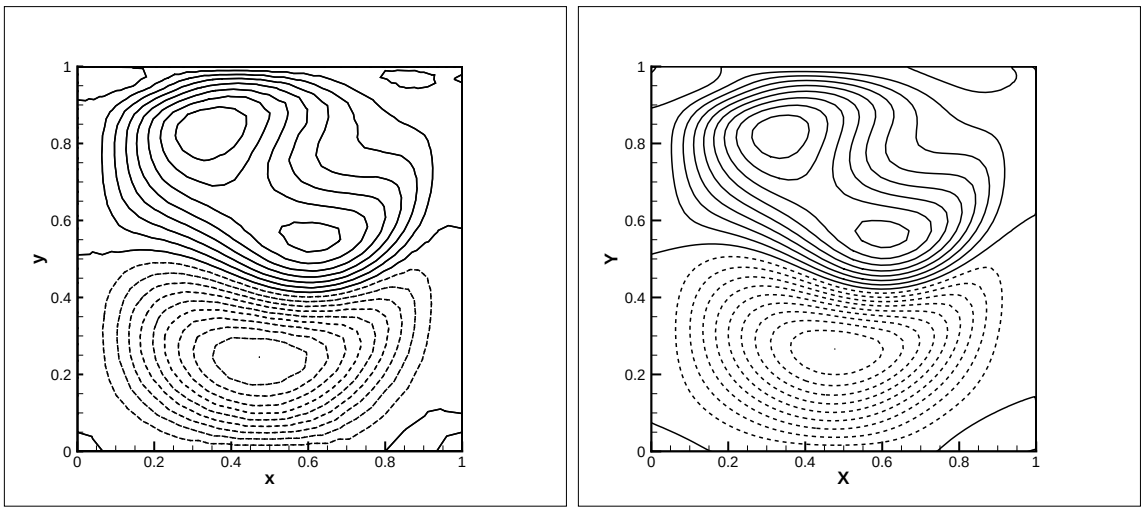

(c) $\hat{u}_{\mathrm{FV}}(x, y)$ (d) $\hat{u}_{\mathrm{SC}}(x, y)$

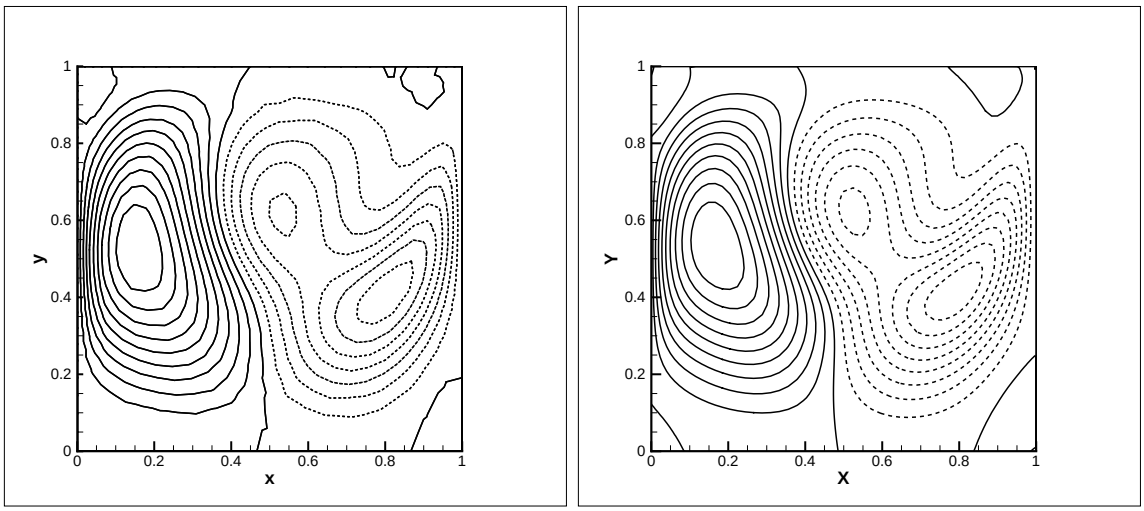

(e) $\hat{v}_{\mathrm{FV}}(x, y)$ (f) $\hat{v}_{\mathrm{SC}}(x, y)$

Figure 5.2: Leading (damped) eigenmode obtained using DNS and a JFNK time-stepping method at $Re = 200$. SC: spectral collocation, FV: finite volumes. eigenvectors are normalized with $\hat{u}_{max}$ and $\hat{v}_{max}$. Dashed lines mean negatives values. 21 equidistant isolines from $\hat{u} = -1$ to $\hat{u} = 1$ and $\hat{v} = -1$ to $\hat{v} = 1$.

results can be obtained. However for short integration times the spectrum cannot be recovered. In addition, if the integration time is too long, most of the transformed spectrum will vanish into the unit circle origin, so very few eigenvalues could be recovered, as indicated by Relation (5.3). The relative error is defined by

$$\epsilon_r = \left| \frac{\lambda_{BG} - \lambda_{TS}}{\lambda_{BG}} \right| . \tag{5.6}$$

Regarding the accuracy of the numerical differentiation, in Table 5.2 it can be seen the effect of the parameter ϵ using second order numerical differentiation with the Eriksson and Rizzi control equation. The recommended values available in the literature lead to correct results.

The effect of using a constant ϵ can be seen in Table 5.3, that shows that if the initial value of the perturbation is properly chosen, this parameter does not have a significant importance.

Higher mesh resolution provides more accurate results. This can be appreciated in Table 5.4. However, this does not significantly affect the shape of the spectrum, therefore it does not change the number of correctly recovered eigenvalues, although it significantly increases the computational time needed.

Table 5.1: Influence of τ on FVM results. First Eigenvalue with $\Delta x = 10^{-3}$, $n_{nodes} = 900$, $m = 60$, $\epsilon = 10^{-2}$. Relative error obtained comparing first eigenvalue obtained with BG

τ	λ_r	λ_i	ϵ_r
0.05	0.37727	5.30130	13.547%
0.25	0.34300	0.00000	3.233%
0.625	0.33975	0.00000	2.253%
1.125	0.33997	0.00000	2.261%
2.5	0.33984	0.00000	2.282%
5	0.33989	0.00000	2.295%
7.5	0.33981	0.00000	2.271%
10	0.33983	0.00000	2.277%

Table 5.2: Influence of ϵ_0 on SCM results. Relative error obtained comparing first eigenvalue obtained with BG

n	m	τ	ϵ_0	λ_r	ϵ_r
48	20	1	10^{-5}	0.33918	2.10%
48	20	1	10^{-6}	0.33654	1.30%
48	20	1	10^{-7}	0.33654	1.30%
48	20	1	10^{-8}	0.33654	1.30%

Table 5.3: Influence of ϵ on FVM results. First Eigenvalue with $\Delta x = 10^{-3}$, $n_{nodes} = 900$, $m = 60$, $\tau = 10$. Relative error obtained comparing first eigenvalue obtained with BG

ϵ	λ_r	ϵ_r
10^0	0.33987	2.289%
10^{-2}	0.33983	2.277%
10^{-4}	0.33954	2.189%
10^{-6}	0.33948	2.171%

Table 5.4: Influence of mesh resolution n on SCM results. Relative error obtained comparing first eigenvalue obtained with BG

n	m	τ	λ_r	ϵ_r
48	20	1	0.33918	2.10%
64	20	1	0.33914	2.09%
80	20	1	0.33907	2.06%

Table 5.5: Influence of mesh resolution on FVM results. Relative error obtained comparing first eigenvalue obtained with BG.

Mesh	Method	Δx	λ_r	error	CPU time (serial)	Memory
64x64 SC	BG	-	0.3322	-	2 min	1.6GB
Mesh A	FVM	10^{-3}	0.3398	2.28%	0.5h	500KB
Mesh B	FVM	10^{-4}	0.3313	0.27%	100h	20MB

Regarding the FVM mesh influence, the maximum achievable accuracy is given by the mesh characteristics. The modes can be recovered with great accuracy if a good mesh is used along proper time-stepping parameters as it can be seen in table 5.5.

The codes have been run on a standard desktop computer having 4GB of RAM memory and 3MB of L2 Cache. CPU times in serial machines are estimated by $ET \sim m \cdot \tau \cdot N_{nodes}/\Delta x$. Table 5.5 shows that high quality meshes lead to significantly better results that those provided by low quality meshes. However, the increment in CPU time is two orders of magnitude larger than the improvement in accuracy. In addition, the memory required to perform the analysis is insignificant compared to the one required in the BiGlobal analysis, even with high quality meshes.

As a small summary of this subsection, it has been demonstrated the feasibility of performing instability analysis using unsteady standard finite-volume solvers. Guidance for the required parameters of the time-stepping method have been provided, which have a crucial importance in the reliability of performing the analysis. Instability of three-dimensional flow using these findings will be carried out in the next chapter.

5.2 Comparison of time-stepping with alternative EVP solution methodologies

Attention has been paid in the previous section to the somewhat artificial dilemma of whether to perform global linear instability in a matrix-forming or a time-stepping framework, which has plagued the community of global instability practitioners since its formation. In this subsection, a new question is addressed regarding the degree to which the RA, DMD and POD algorithms may be used to extract quantitative information from the same simulation data used in the time-stepping (TS) or matrix-formation algorithm discussed in the previous subsection; the square lid-driven cavity is chosen again as a test-flow for this section.

As a non trivial example of structures identification, linear global modes of the two-dimensional lid-driven cavity flow have been obtained by solution of the BiGlobal (BG) eigenvalue problem (2.4) on 64×64 spectral collocation points at subcritical conditions, ($Re = 2000, \alpha = 0.0001$), as well as by performing DMD, time-stepping (TS), residual-algorithm RA and POD analyses of DNS-obtained solutions. This flow is known to be stable [115] and comprise both stationary and traveling decaying modes. The objective of this section is to compare the performance of the different approaches in describing these structures. For the DNS work the flow is calculated with spectral collocation for the spatial discretization and the algorithm proposed by Spalart *et al.* in [98] for the temporal discretization. More details about the DNS can be found in [116]. The Chiba approach [17] has been followed in the TS analysis, with a random linear perturbation superimposed upon the base flow used as initial condition, and a total integration time $t = 40$. For this particular base flow, a small Krylov subspace dimension ($m = 6$) is sufficient to capture accurately the first two flow eigenmodes. Regarding the frequency recovery, an aliasing-like problem occurs due to the relatively large integration time used in the DNS and the fact that the complex logarithm is a multi-valued function. However, this problem is easily solved by analyzing the Fourier transform of the DNS. In order to compute DMD/Koopman modes and POD a sequence of 400 snapshots is taken, starting at $t = 200$ with $\Delta t = 2$, not sampling the transient time.

Fig. 5.3 (upper) presents the leading eigenmode of lid driven cavity flow at $Re = 2000$ obtained by using four different methods: BiGlobal analysis, DMD, TS, residual algorithm (RA) and POD analysis. In all cases line-thickness agreement is seen in the respective results. The leading corresponding eigenvalue is compared in Table 5.6 for the four methods.

Table 5.6: Damping rate of the leading stationary eigenmode obtained by solution of the global instability eigenvalue problem and DMD analysis of transient DNS data

Mode I				
	EVP (2.4)	DMD (2.26)	TS (2.4)	RA (2.16)
$\Re\{\omega\}$	0	0	0	0
$\Im\{\omega\}$	-0.031714	-0.031712	-0.031754	-0.031703
Mode II				
	EVP (2.4)	DMD (2.26)	TS (2.4)	RA (2.16)
$\Re\{\omega\}$	0.966158	0.963098	0.961099	0.958778
$\Im\{\omega\}$	-0.066754	-0.064574	-0.067017	-0.059983

On the other hand, due to the existence of a strongly dominant linear instability (high kinetic energy level) over the flow field pattern, the first POD "topo-mode" (See Eq. (2.23)) is able to capture its spatial structure. BiGlobal analysis results are considered as converged reference. Relative error for the leading eigenvalue is $6.3 \cdot 10^{-5}$ for the DMD analysis, $1.2 \cdot 10^{-3}$ for TS analysis and $3.4 \cdot 10^{-4}$ for the RA algorithm.

As it was mentioned before, the first POD "topo-mode" is able to capture the spatial structure of the leading linear global eigenmode, due to the existence of a large damping ratio. However the first POD "chrono-mode" (See Eq. (2.23)) presents a single oscillatory frequency ($\omega_r = 0.000976$). Fig. 5.4 (lower) presents the frequency diagram of this first POD "chrono-mode" which contains more than 99.9% of the kinetic energy. As usual in POD analysis, POD modes travel in pairs. In this problem, energy level and magnitude of second and third "topo-" and "chrono-" modes are of the same order. Due to its small amount of energy, they can be considered as small variations of the dominant mode that compose the original flow and they are not considered as relevant case of this study.

Fig. 5.3 (lower) presents the second leading eigenmode of lid driven cavity flow at $Re = 2000$ obtained by the first four methods (upper). Line thickness agreement is again recovered in the results of the first four methods. The second leading eigenvalue is also presented in Table 5.6. The relative error of the real part of the eigenvalue is $3.1 \cdot 10^{-3}$ for the DMD analysis, $3.9 \cdot 10^{-3}$ for TS analysis and $7.6 \cdot 10^{-3}$ for the RA algorithm and for the imaginary part is $3.2 \cdot 10^{-2}$ for the DMD analysis, $5.2 \cdot 10^{-3}$ for TS analysis and $1.0 \cdot 10^{-1}$ for the RA algorithm.

Fig. 5.4 (upper) presents the damping ratio σ obtained with the RA method. The damping rate presents a exponential decay with time and is a linear combination of the first, second and third leading modes. Two traveling modes with frequency $\omega_r = 0.958778$ and $\omega_r = 1.879050$ are superimposed upon the non oscillatory steady mode ($\omega_r = 0$) and are shown in Fig. 5.4 (middle), which presents the correspondence of the frequencies of the damped linear two-dimensional eigenmodes of the converged steady-states, with those obtained from discrete Fourier transforms of the DNS.

In summary, it is shown that in this particular flow configuration, which is dominated by a few stationary and traveling linearly-damped eigenmodes, the frequency and damping characteristics of the leading linear flow perturbations are captured correctly by either of DMD, TS and RA analysis. Due to the fact that the leading POD eigenmode contains practically all the disturbance energy at the conditions examined, POD analysis can also capture exactly this dominant flow perturbation, such that any of the aforementioned methods may be used if analysis is to focus exclusively on that flow eigenmode.

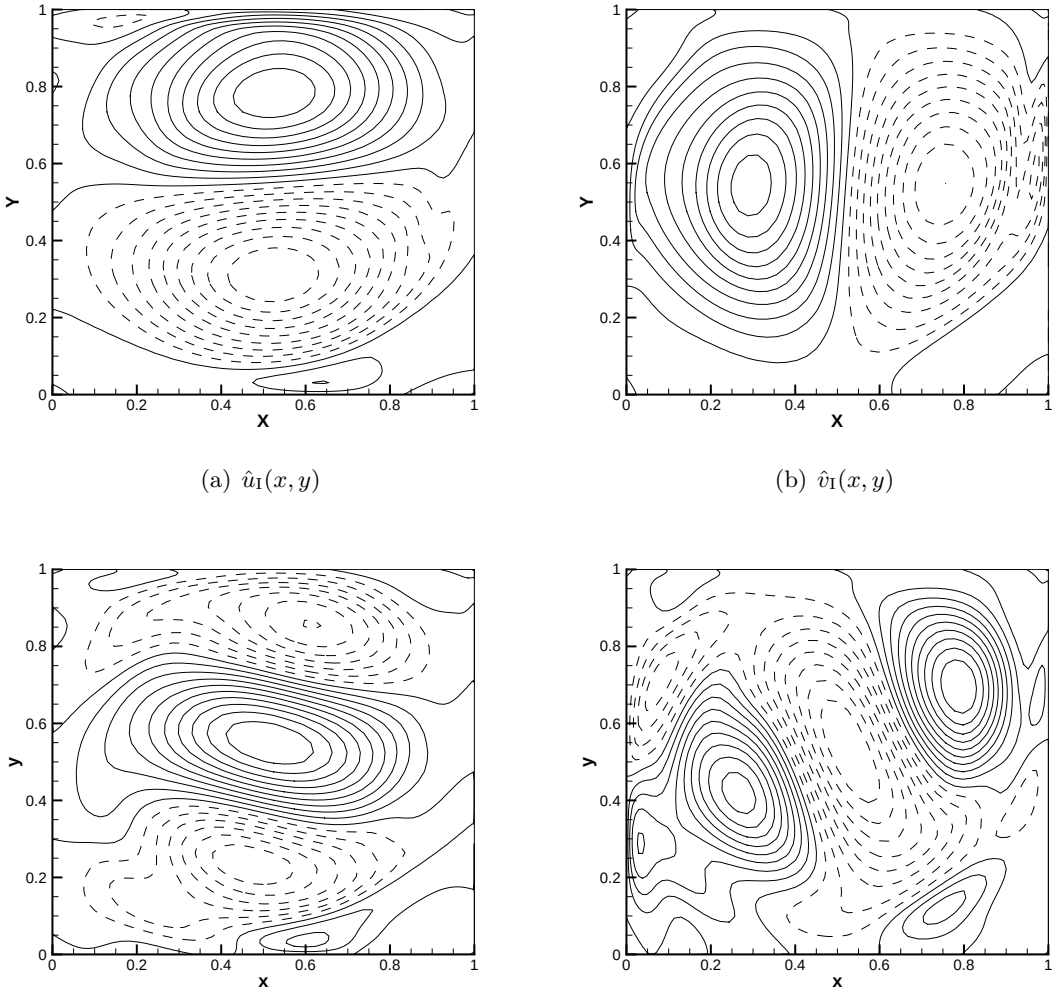

(a) $\hat{u}_{\mathrm{I}}(x, y)$

(b) $\hat{v}_{\mathrm{I}}(x, y)$

(c) $\hat{u}_{\mathrm{II}}(x, y)$

(d) $\hat{v}_{\mathrm{II}}(x, y)$

Figure 5.3: Upper: Leading eigenmode of the regularized LDC obtained using BiGlobal Instability Analysis (BG), Time-stepping (TS), Koopman analysis (DMD) and residual algorithm (RA) and first Proper Orthogonal Decomposition (POD) "topo-mode" (Eq. (2.23)) at Re= 2000. Lower: Second eigenmode of the regularized LDC obtained using BiGlobal Instability Analysis (BG), Time-stepping (TS), Koopman analysis (DMD) and residual algorithm (RA) at Re= 2000. Eigenvectors are normalized with $\hat{u}_{max}$ and $\hat{v}_{max}$. Dashed lines mean negatives values. 21 equidistant isolines from $\hat{u} = -1$ to $\hat{u} = 1$ and from $\hat{v} = -1$ to $\hat{v} = 1$. Line-thickness agreement is obtained between the results of all algorithms employed.

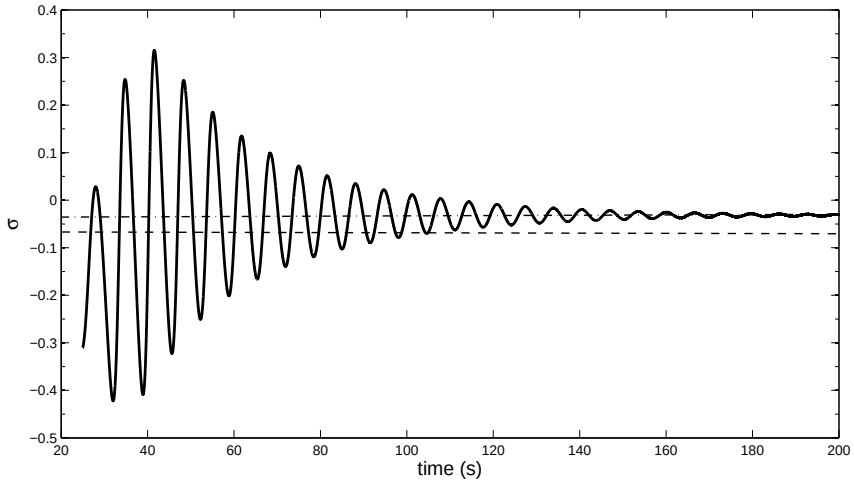

(a) *Damping ratio in RA*

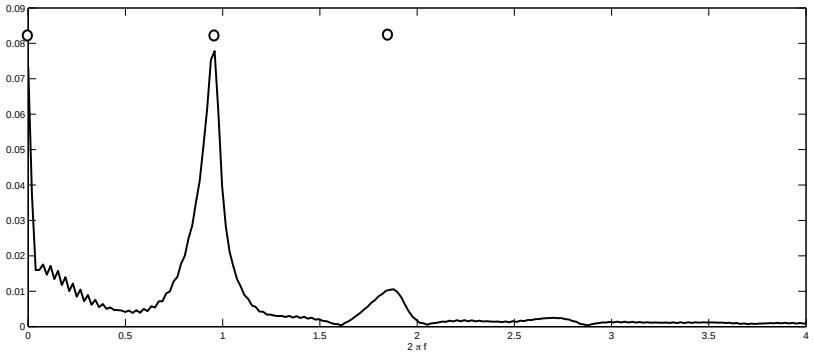

(b) *Frequency in RA*

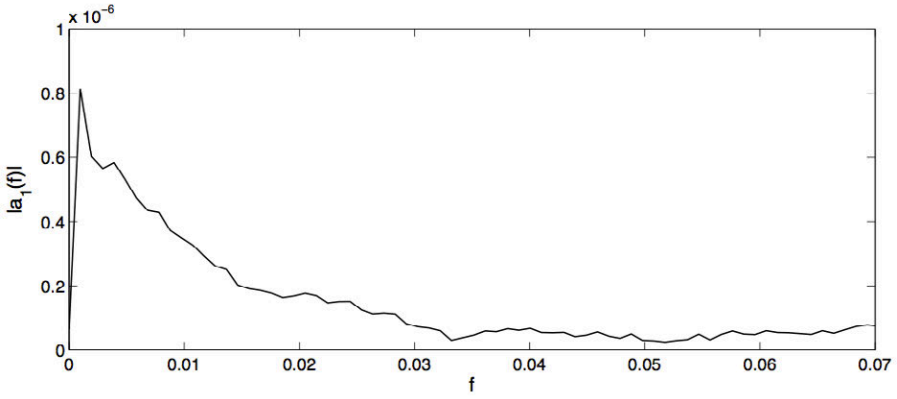

(c) *Frequency in POD*

Figure 5.4: Upper: Dependence of damping ratio σ with time showing the exponential decay of two traveling modes ($\omega_r = 0.958778$, $\sigma = 0.059983$) and ($\omega_r = 1.879050$, $\sigma = 0.065227$), superimposed upon the steady mode ($\omega_r \sim 0$, $\sigma = 0.031703$) at $Re = 2000$. Middle: Correspondence of the frequencies of the damped linear two-dimensional eigenmodes of the converged steady-states obtained from discrete Fourier transforms of the DNS signals at $Re = 2000$. Lower: Frequency diagram of the first POD "chrono-mode", Eq. (2.23), ($\omega_r = 0.000976, 0.012695, 0.041992$) at $Re = 2000$.

5.3 Validation of the exponential shift-invert methodology

The stenosic flow studied by Sherwin et al. [117] has been considered in this section in order to validate the exponential shift-invert methodology. The linearized solver of the spectral element code Semtex is used in conjunction of the instability methodology.

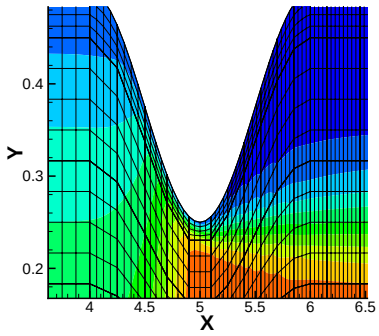

Figure 5.5: Details of the mesh used for the stenotic flow. Note that a high-degree polynomial is used inside each element. Superposed in color is the streamwise component of the basic velocity field.

Linear stability around the steady stenosic flow at $Re = 500$ and $Re = 700$ is considered in this section. The mesh and $x-$velocity component of the base flow is presented in Figure 5.5. The base flow solution is obtained using Newton–Raphson iteration started from a known initial solution, see Blackburn [38] for details. For these simulations, polynomial orders $N_p = 5$ and $N_p = 7$ were considered in order to expand flow variables within each element. A low value of $N_p = 5$ was sufficiently accurate for our study and at the same time permits fast simulations. The Krylov subspace dimension, the maximum number of iterations and the tolerance were taken equal to 8, 200 and 10^{-5}, respectively.

As seen in Table 5.7 and Figures 5.6, there is a very good agreement between the results obtained with the exponential method (Figure 4.2) and the real shift invert method (Figure 4.4). The most unstable modes obtained using the two strategies agree up to the third decimal place.

Table 5.7: Convergence of most unstable eigenvalues for stenosis flow at $Re = 700$, where $N_p = 5$ and m is the number of Arnoldi iterations. Krylov dimension = 8, $tol_{Arnoldi} = 10^{-5}$, $N_{Arnoldi} = 200$. *Case a*: Exponential method, *Case b*: Real shift-invert method for $\sigma = 0$, $tol_{Bi-CGSTAB} = 10^{-3}$ and $N_{Bi-CGSTAB} = 300$

Cases	Magnitude	Angle	Growth Rate	Frequency	N
a	9.9723(-01)	0.0000	-3.7011(-03)	0.0000	76
b	9.9737(-01)	0.0000	-3.5113(-03)	0.0000	8

The different tolerances considered delivered converged solutions in all cases, see Table 5.8. As it can be seen, the maximum number of iterations was not achieved in any case, which is a requisite for an accurate solution. It is also remarkable that the number of iterations carried out in the

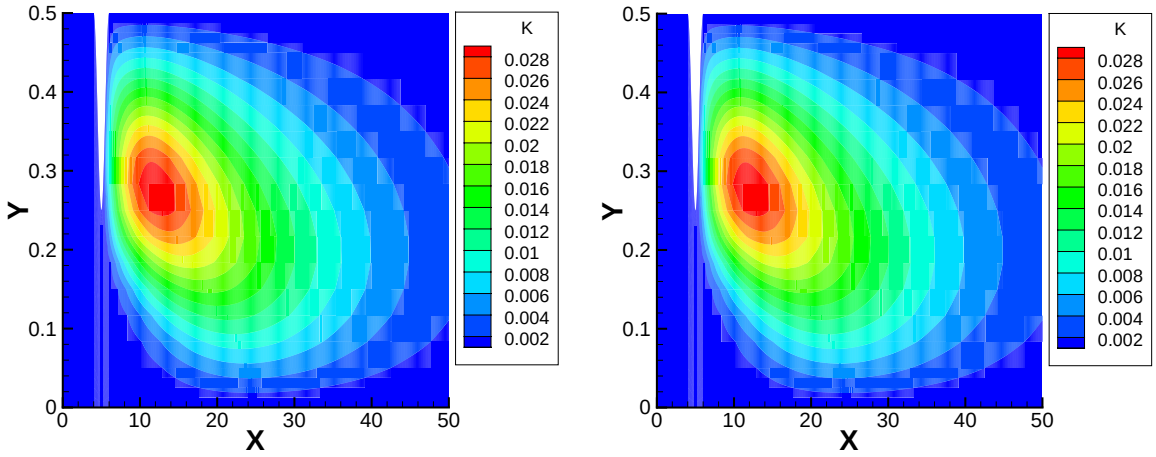

(a) (b)

Figure 5.6: Stenotic flow at $Re = 700$, in which ($K = \sqrt{u^2 + v^2 + w^2}/2$). Velocity modulus of the most unstable eigenvector calculated by the exponential and the Arnoldi shift invert strategy with shift equal to 1. *Left:* Exponential method. *Right:* Real shift-invert method.

internal loop is independent of the Arnoldi tolerance at convergence. Likewise, it can be seen that the number of Arnoldi iterations is drastically reduced from 76 to 8 when the shift-invert method is used in place of the direct method. This, however, does not imply a reduction in the computational cost, due to the high number of iterations required to invert the matrix on each Arnoldi iteration. These numbers used in the Bi-CGSTAB loop are summarized in Table 5.8.

Table 5.8: Number of iterations carried out by the Bi-CGSTAB algorithm for the stenosis flow problem at $Re = 700$. Real shift-invert method for $\sigma = 0$, Krylov dimension = 8, $tol_{Arnoldi} = 10^{-5}$, $m = 100$. *Case a*: *Magnitude* = 9.9737(-01), *Growth Rate* = -3.5111(-03), $tol_{Bi-CGSTAB} = 10^{-3}$ and $N_{Bi-CGSTAB} = 300$ *Case b*: *Magnitude* = 9.9737(-01), *Growth Rate* = -3.5113(-03), $tol_{Bi-CGSTAB} = 10^{-4}$ and $N_{Bi-CGSTAB} = 300$ $a.b(c) = a.b \times 10^c$.

Arnoldi Iteration	*Case a*	*Case b*
1	62	73
2	43	50
3	44	51
4	53	53
5	66	67
6	69	95
7	78	101
8	80	109

In order to evaluate the shifting capability of the method, a value of $\sigma = 0.1$ has been used to extract non-leading eigenvalues from the spectrum. Results of these runs at different Arnoldi

and Bi-CGSTAB tolerance can be seen in Table 5.9. The recovery of this eigenvalue has not been possible by using the exponential method at the same resolution and tolerance for any number of iterations or Krylov subspace dimension. In addition, it can be observed in Table 5.9 that increases in accuracy barely change the number of Arnoldi iterations required, as it was noticed before. On the other hand, the total number of Bi-CGSTAB iterations increases with the tolerance.

Table 5.9: Number of iterations carried out by the shift-invert algorithm for the stenosis flow problem at $Re = 500$ for different tolerances with $tol_{Arnoldi} = tol_{Bi-CGSTAB}$ and $\tau = 6$. Real shift-invert method for $\sigma = 0.1$, $m = 8$.

$tol_{Bi-CGSTAB}$	10^{-3}	10^{-4}	10^{-5}
$N_{Arnoldi}$	13	13	13
$N_{Bi-CGSTAB}$	216	277	312
Growth Rate	-0.43269	-0.43269	-0.43270
Frequency	0.037742	0.037742	0.037748

Regarding the effect of the integration time, Table 5.10 presents the effect of the increase in integration time Δx on the total number of Bi-CGSTAB iterations. It can be appreciated that the total number of iterations are reduced as the integration time increases.

Table 5.10: Number of iterations carried out by the Bi-CGSTAB algorithm for the stenosis flow problem at $Re = 500$ and at different integration times Δt. Real shift-invert method for $\sigma = 0$, Krylov dimension = 8, $tol_{Arnoldi} = 10^{-3}$, $m = 100$, $tol_{Bi-CGSTAB} = 10^{-3}$ *Magnitude* = 9.7378(-01), *Growth Rate* = -5.3146(-02)

Arnoldi Iteration	$\Delta t = 1$	$\Delta t = 2$	$\Delta t = 4$
1	20	11	5
2	22	9	4
3	16	8	3
4	15	7	4
5	18	9	4
6	26	10	5
7	21	10	4
8	28	10	4
$N_{Bi-CGSTAB} \cdot \Delta t$	166	148	132

From these results it is concluded that, although the time-stepping shift-invert methodology has been successfully applied to study global instability analysis using a new shift-invert strategy aiming at the efficient capturing of any eigenvalue of the spectrum, the inversion of the Jacobian-matrix requires a significant number of Bi-CGSTAB iterations in order to converge. This leaves the classical exponential transformation as the method of choice for the recovery of leading eigenvalues. On the other hand, the strength of this method resides in accessing to specific parts of the full global spectrum and this methodology could complement the exponential method when full access to the eigenspectrum is required. Finally, as opposed to other methods described through the

subsection, this strategy can be directly applied to any time-stepper, regardless of its temporal or spatial discretization.

Chapter 6

Time-stepping for TriGlobal Instability Analysis of Wall-bounded Flows

6.1 Three-dimensional Lid-driven Cavity

The three-dimensional, lateral-wall-bounded lid-driven cavity was chosen as a demonstration problem for TriGlobal linear instability analysis, since it permits examining two different aspects: physical complexity and computational efficiency. In addition, the non-unity aspect ratio configuration of this cavity flow, though well-studied from an experimental and a three-dimensional DNS point of view, has presenty not been addressed as regards its TriGlobal linear instability.

From the point of view of physical complexity, the accurate description of the fully three-dimensional lid-driven cavity flow still remains inconclusive in many aspects, as stated in the recent work by Feldman & Gelfgat [30], although the analysis of the two-dimensional counterpart of the lid-driven cavity flow has become a benchmark problem in fluid mechanics and has been extensively reviewed [118, 119, 120] .

The main reason for this lack of understanding is that the three-dimensional lid-driven cavity flow, as found experimentally by Koseff and Street [121, 122] and numerically by Iwatsu et al. [123, 124], presents a far more complicated structure that cannot be directly compared to the corresponding two-dimensional flow. The most important three-dimensional flow features are the Taylor-Görtler-Like (TGL) vortices [121, 125] and corner eddies or end-wall vortices (EWV) [126, 127] in the flow field. Figure (6.1) shows schematically the geometry and the main flow features: primary eddie (PE), downstream secondary eddie (DSE), upstream secondary eddie (USE) and upstream upper eddie (UUE).

Aidun et al. [128] performed lid-driven cavity experimental visualizations, presenting an excellent qualitative description of the state diagram of TGL structures and demonstrated the existence of different branches of n-cell TGL structure. They observed that stability is lost through growth of a steady primary mode with a one-cell pattern and that the flow becomes oscillatory because of the subsequent competition of the steady modes with the remaining rest of n-cell TGL branches. Guermond et al. [129] carried out comparisons between numerical and experimental start-up flows in lid-driven cavities of aspect ratio 1:1:2. In agreement to Aidun et al. [128] and Migeon [130],

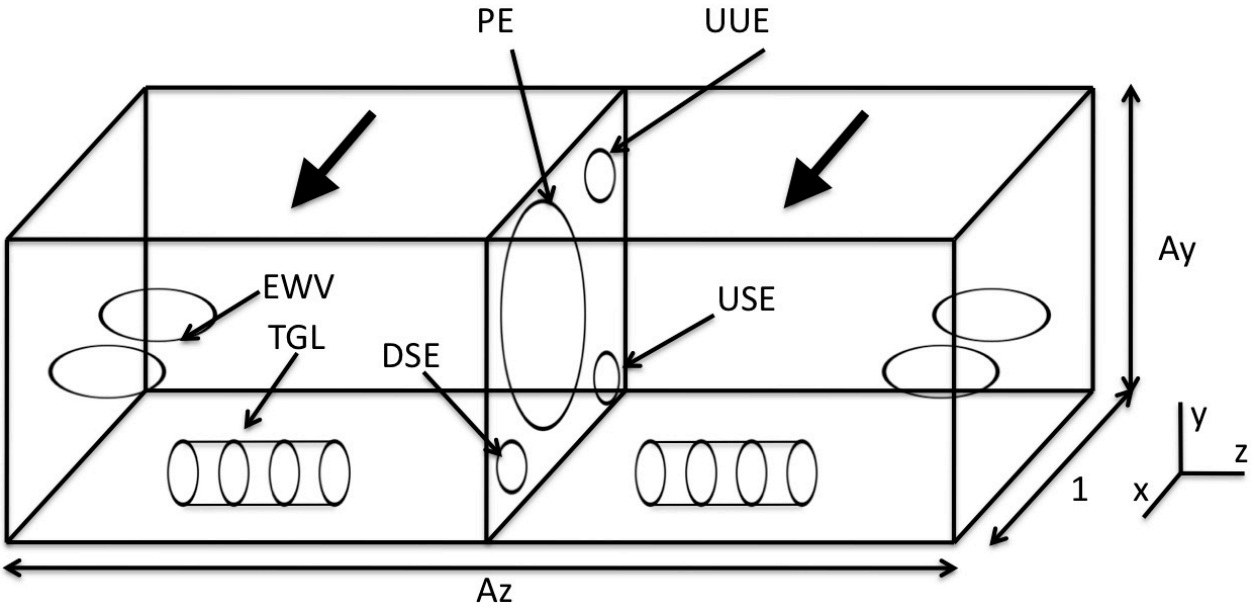

Figure 6.1: Geometrical description of the 3D lid-driven cavity and main flow features

the time evolution of the perturbations showed several TGL structures even at $Re = 1000$. These observations indicate that the stable eigenfunctions of the flow may be related with the TGL structures. In addition, Kim and Moin [131] linked the existence of perturbations with the formation of TGL vortices in their numerical work. Along the same line of qualitative association of linear flow perturbations and TGL vortices, Koseff and Street[121, 122] also suggested that most of the velocity fluctuation in the lid-driven cavity at low Reynolds number are caused by the TGL vortices. The above qualitative explanations provide motivation for validating the present methodology with the three-dimensional lid-driven cavity.

Linear stability analysis in the case of periodic boundary conditions, corresponding to a two dimensional base flow imposing a third homogeneous direction, was first studied by Ramanan and Homsy [132] and later by Ding and Kawahara [114]. Correct critical Reynolds number for different wave number were given by Theofilis et al. [133, 112] and Albensoeder et al. [134] among other works. The most unstable eigenvector appears with a wave number of $\alpha \sim 15.3$ at a critical Reynolds number $Re_{cr} \sim 783$. Following this methodology, other wall-bounded cavities with one homogeneous spatial direction have been also studied, such as swirling [135], triangular [41] or double-sided [136] lid-driven cavities.

Regarding the instability onset of the cubic lid-driven cavity, the latter part of the past decade has seen some significant advances in this field [118, 123, 124, 137, 138]. Giannetti et al. [28] found, by means of the first TriGlobal linear stability analysis applied to this kind of flows, that a stationary mode becomes unstable just above $Re \sim 2000$. The latter result is consistent with that of Liberzon et al. [29, 30], who refined the prediction of Giannetti et al. [28] and experimentally and numerically found that the flow becomes oscillatory at $Re > 1970$ and a steady-unsteady transition occurs in the range $1700 < Re < 1970$. This kind of steady-unsteady transition has been also observed by Aidun, Benson at al. [128, 139] and Chiang et. al [140, 126] in a cavity of aspect ratio $1 : 1 : 3$, and by Albensoeder and Kuhlmann [141] with a very long cavity of aspect ratio $1 : 1 : 6.55$.

In order to alleviate disagreements in the numerical results of three-dimensional cavity flows [118, 123, 124, 137, 138], Albensoeder and Kuhlmann [142] created benchmark data of the three-dimensional cubic lid-driven cavity flow by employing high-order spectral collocation schemes. They show that rather high resolutions of $N^3 = 96$ spectral collocation nodes are required for an accurate description of the flow at $Re = 1000$. The lack of such resolution in several previous studies by other authors could explain most disagreements. Taking this benchmark data into account, Feldman & Gelfgat [30] made use of a resolution up to $N^3 = 200$ for their research of the cubic lid driven cavity stability, while Liberzon et al. [29] validated the results of Feldman & Gelfgat [30] experimentally. At this point, considering the resolutions employed for an accurate description of the flow in previous works, it is expected that computational cost required for an TriGlobal instability analysis of the three-dimensional wall-bounded lid driven cavity using second-order methods can become formidable and can be considered a challenge for the methodology presented in Chapter 4.

6.1.1 Base Flow

The base flow results of the cubic lid-driven cavity at $Re = 1000$ have served as validation case of the capability to run an incompressible solver of OpenFOAM® in DNS mode; a grid convergence analysis has been carried out. Then the obtained steady-state solution has been compared with the benchmark data created by Albensoeder et al. [142] and the transient solver quality have tested comparing the damping ratio using the residual algorithm described in Section 2.1.3 [65, 143].

The transient incompressible solver *icoFoam* has been employed to obtain the base flow. The Reynolds number Re is based on the lid speed and length in the x-direction and no-slip boundary conditions $u = v = w = 0$ are applied at all the boundaries, except in the lid-driven wall, where $u(x, y, z) = 1$. The base flow is calculated by advancing in time the Navier-Stokes equations from a quiescent initial condition until the residual satisfies a predetermined convergence criterion. This residual $\varepsilon(t)$ is defined at each time t as the $L1$ norm of the discretized residual vector

$$\mathbf{u_r}(t) = \frac{\partial \mathbf{u}(t)}{\partial t} + \mathbf{u}(t) \cdot \nabla \mathbf{u}(t) - \frac{1}{Re} \nabla^2 \mathbf{u}(t) + \nabla p(t)\,, \tag{6.1}$$

normalized by the initial residual $\varepsilon(0)$. A residual tolerance for the temporal integration $\varepsilon(t) < \epsilon_m$ with $\epsilon_m = 10^{-12}$ has been found sufficient for this work.

A grid refinement study based on a generalized Richardson extrapolation method [144], as used by Sanmiguel-Rojas et al. [93] has been employed in order to analyze mesh convergence. The method consists of constructing a grid convergence index [144] (GCI) that acts as a measure of the behavior of the numerical solution as it approaches a grid-independent asymptotic value, following the Richardson extrapolation method. This grid convergence index [144] can be defined as:

$$GCI_{j+1,j} = 3 \times \left| \frac{u_{j+1} - u_j}{u_j (l^n - 1)} \right| \times 100\,, \tag{6.2}$$

where u_j is any variable discretized on mesh j, where mesh $j+1$ is coarser than mesh j, l is the fine-to-coarse grid size refinement ratio in one spatial direction and n is the order of convergence rate of the method. In addition, attention has to be paid in order to ensure that monotonic convergence has been achieved before applying the method. Furthermore, the grid-independent solution based on Richardson extrapolation can be estimated as

Table 6.1: Grid convergence study based on u velocity for the cubic Lid-Driven cavity at $Re = 1000$ using five meshes: M1 finest, M2 fine, M3 medium, M4 coarse and M5 coarsest. Grid convergence index obtained with $l = 1.5$ and $n = 1.71$

Mesh	N_x	N_y	N_z	Number of nodes	$u(0.5, 0, 75, 0, 5)$	$GCI_{j+1,j}(\%)$	rel error ϵ_j (%)
Grid-independent	-	-	-	-	0.07861	-	-
M1	216	216	216	$\sim 1 \times 10^7$	0.07859	0.54	0.02
M2	144	144	144	$\sim 3 \times 10^6$	0.07852	1.09	0.11
M3	96	96	96	$\sim 9 \times 10^5$	0.07837	2.01	0.29
M4	64	64	64	$\sim 2.5 \times 10^5$	0.07811	3.92	0.63
M5	42	42	42	$\sim 7.5 \times 10^4$	0.07759	-	1.29

$$u_{re} \sim u_j + \frac{u_{j+1} - u_j}{(l^n - 1)}\,, \tag{6.3}$$

so the corresponding relative percentage error of each mesh compared to the grid-independent solution is defined as:

$$\epsilon_j = \left| \frac{u_j - u_{re}}{u_{re}} \right| \times 100\,. \tag{6.4}$$

Table 7.1 presents the convergence results obtained with the incompressible OpenFOAM® solver for five meshes with different resolutions of the cubic lid-driven cavity flow at $Re = 1000$. A cubic mesh with a linear stretching function of $1 : 8$ ratio has been employed in order to solve accurately the flow in the vicinity of the lid and cavity walls and corners. The velocity in the direction of the lid movement u in the point $(0.5\,, 0.75\,, 0.5)$ has been selected as probe in order to alleviate the influence of the mesh stretching in the three directions towards the walls on the GCI.

Results shown in 7.1 demonstrate the slow improvement in accuracy as resolution is increased, due to the second-order accuracy of the numerical discretization even with a fine-to-coarse grid size refinement ratio $l = 1.5$ in each direction. It can be seen that the GCI-based on the velocity component u in the lid direction indicates than the mesh M2 with $\sim 3 \times 10^6$ cells is necessary to accurately predict the flow in the lid-driven cavity at $Re = 1000$, although the relative error criterion suggests that the resolution employed in mesh M4 may be sufficient to describe the flow this Reynolds number value. Figure 6.2 shows comparisons of normal velocities at the centerlines $(x, 0, 0)$ and $(0, y, 0)$ of the cubic lid-driven cavity at $Re = 1000$, calculated on meshes M3 and M4, against the reference value.

Table 6.2 quantifies the values of maximum and minimum absolute velocity at three different spanwise aspect ratios and shows that the maximum discrepancies from the reference solution are of order $O(10^{-3})$. These minimal differences in base flows obtained on the grids M2, M3 and M4 suggest that any of these grids may provide quantitatively comparable stability analysis results.

In addition, a study of different large aspect ratio cavities flow has been carried out on meshes with same resolution as M2 and M3. Results are also shown in Table 6.2, where a discrepancy of $O(10^{-2})$ from the reference solution can be seen. The accuracy of these base flows is also sufficient for the purposes of the present analyses, as will be shown in the next section.

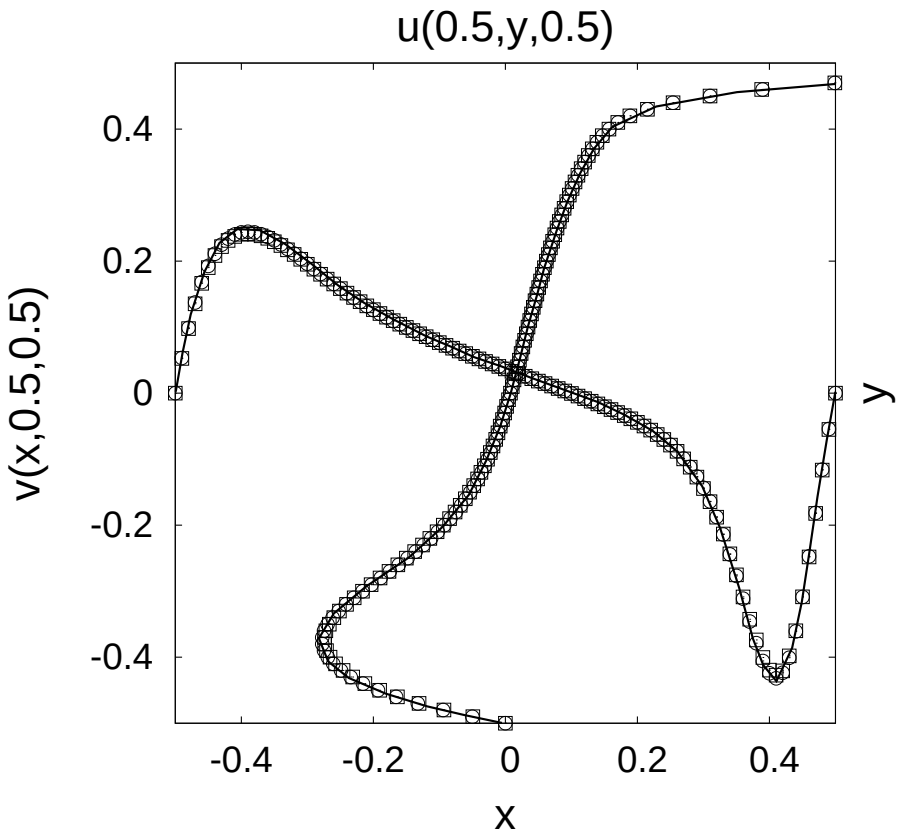

Figure 6.2: Comparisons of normal velocities in the central lines $(x, 0, 0)$ y $(0, y, 0)$ of cubic lid-driven cavity at $Re = 1000$. Lines corresponds to reference values[142], and circle and squares to mesh M4 $N^3 = 64^3$ and mesh M3 $N^3 = 96^3$ respectively

Table 6.2: Comparison with the benchmark [142] solution of the minimum and maximum velocities on the centerlines v(x, 0.5, 0.5) and u(0.5, y, 0.5) for the cubic lid-driven cavity at Re = 1000

Method	AR	N_x	N_y	N_z	v_{min}	x	v_{max}	x	u_{max}	y
SCM	1:1:1	96	96	64	-0.4350	0.9096	0.2466	0.1091	-0.2803	0.1242
FVM	1:1:1	144	144	144	-0.4333	0.9076	0.2456	0.1073	-0.2792	0.1235
FVM	1:1:1	96	96	96	-0.4332	0.9101	0.2444	0.1117	-0.2777	0.1284
FVM	1:1:1	64	64	64	-0.4280	0.9079	0.2416	0.1148	-0.2746	0.1274
SCM	1:1:2	96	96	96	-0.4736	0.9108	0.2941	0.1305	-0.3197	0.1306
FVM	1:1:2	64	64	96	-0.4604	0.9079	0.2852	0.1151	-0.3127	0.1408
SCM	1:1:3	96	96	96	-0.4901	0.9097	0.3235	0.1237	-0.3444	0.1367
FVM	1:1:3	64	64	192	-0.4687	0.9079	0.3001	0.1274	-0.3219	0.1549

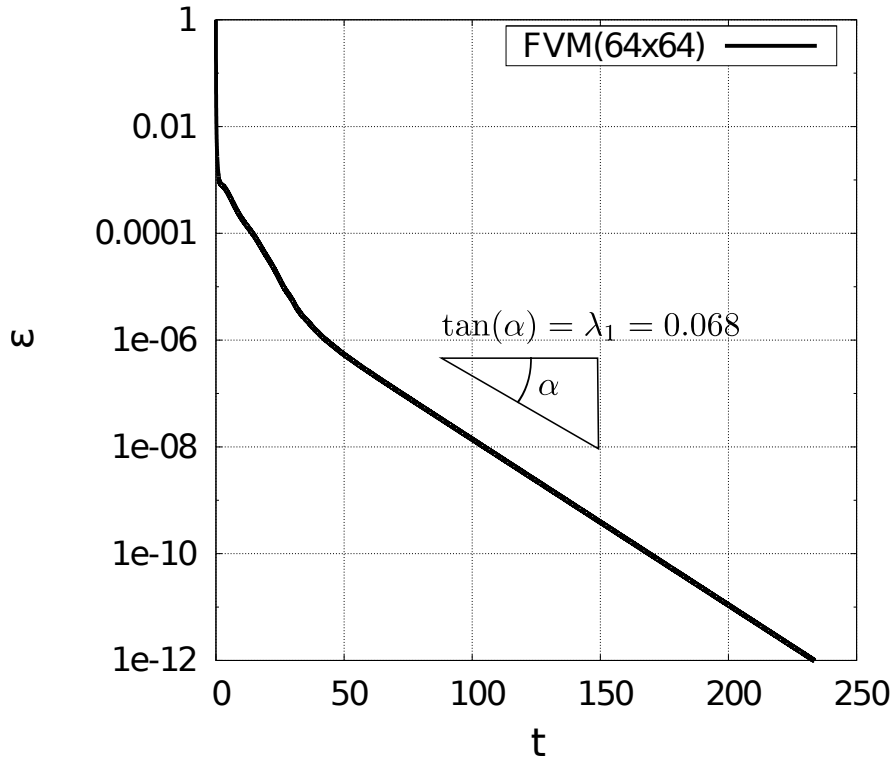

Figure 6.3: Temporal evolution of the velocity residual of the two-dimensional lid-driven cavity at $Re = 1000$

Finally, the transient behavior of the solver has been also validated by means of the residual algorithm developed by Theofilis [65, 143] and explained in Section 2.1.3. For the particular case of a steady leading mode, recalling the definition of residual from (6.1), the corresponding damping ratio can be extracted from the logarithmic derivative of the signal, which reads

$$\lambda_1 = \frac{\ln\left(\frac{\epsilon(t+\Delta t)}{\epsilon(t)}\right)}{\Delta t}\,. \tag{6.5}$$

Figure 6.3 shows the temporal evolution of the residual of the two-dimensional lid-driven cavity at $Re = 1000$, in which the constant slope of the residual decay corresponds to the damping ratio and thus can be recovered with the previous expression. For this particular case, the recovered damping ratio corresponds to $\lambda_1 = 0.068$, which perfectly matches the value available in the literature [112] of $\lambda_{ref} = 0.068$. The same procedure will be used to cross-verify damping rate results of the time-stepping algorithm in the cubic lid-driven cavity against those delivered by this basic signal processing technique.

6.1.2 TriGlobal Instability Analyses

Validation of the present three-dimensional global (TriGlobal) instability analysis algorithm has been provided by comparison against reference works, starting with those of Giannetti et al.[28] at $Re = 1000$. Krylov subspace dimensions ranging from $m = 12$ to $m = 48$ have been tested

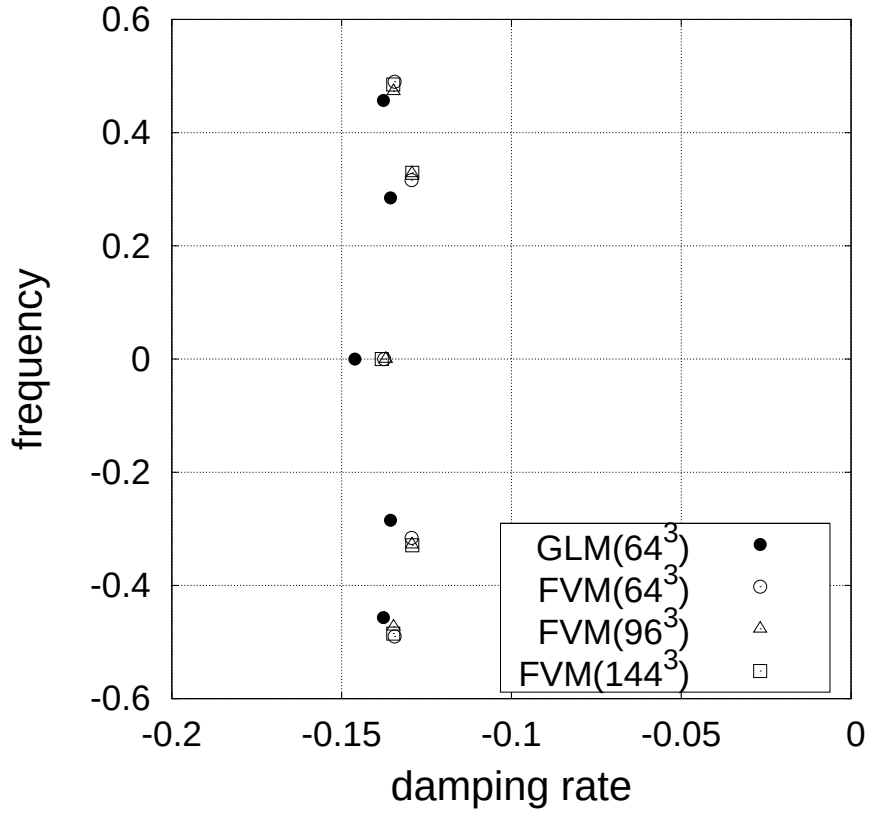

Figure 6.4: Spectrum of cubic lid-driven cavity at $Re = 1000$ calculated by Giannetti et al.[28] (GLM) and own methodology (FVM) with different resolutions

along with integration times from $\tau = 10$ to $\tau = 100$ for the instability analysis. It has been found sufficient to use a Krylov subspace dimension $m = 12$ with integration time $\tau = 40$ for the recovery of the three first leading eigenvalues, satisfying the criteria discussed in the previous section. The recovered eigenvalues calculated with three different meshes M2, M3 and M4 can be seen in Table 6.3. Comparison between the reference spectrum of Giannetti et al. [28] and the present results obtained with these three different meshes can be seen in Figure 6.4. An overall good agreement between the location of the eigenvalues can be seen, while the differences can be explained by the different numerical methods employed. Figure (6.5) shows the eigenfunctions corresponding to these three least stable eigenvalues.

The first two are traveling, corresponding to $\lambda_1 = -0.1292 \pm i0.329$ and $\lambda_2 = -0.138 \pm i0.457$, while the third is a stationary eigenmode with a damping ratio $\lambda_3 = -0.146$. At this Reynolds number, it is observed that the two first eigenvalues are related to the corresponding modes of the two-dimensional flow, properly affected by the presence of the wall and thus the above-mentioned EWV structure. However, the existence of different n-cell symmetric and asymmetric families of linear modes with TGL structure may be inferred from the third mode.

Stability analysis at $Re = 2000$ close to the instability onset has also been performed on the coarser meshes M3 and M4. Figure 6.6 shows the temporal evolution of the flow using these two

Table 6.3: Effect of resolution on the first three leading eigenvalues of the lid driven cavity at $Re = 1000$

$N_x \times N_y \times N_z$	λ_1	λ_2	λ_3
$144 \times 144 \times 144$	-0.1292 $\pm i$0.329	-0.1348 $\pm i$0.485	-0.1382 $\pm i$0.000
$96 \times 96 \times 96$	-0.1293 $\pm i$0.328	-0.1347 $\pm i$0.473	-0.1370 $\pm i$0.000
$64 \times 64 \times 64$	-0.1294 $\pm i$0.316	-0.1344 $\pm i$0.490	-0.1375 $\pm i$0.000

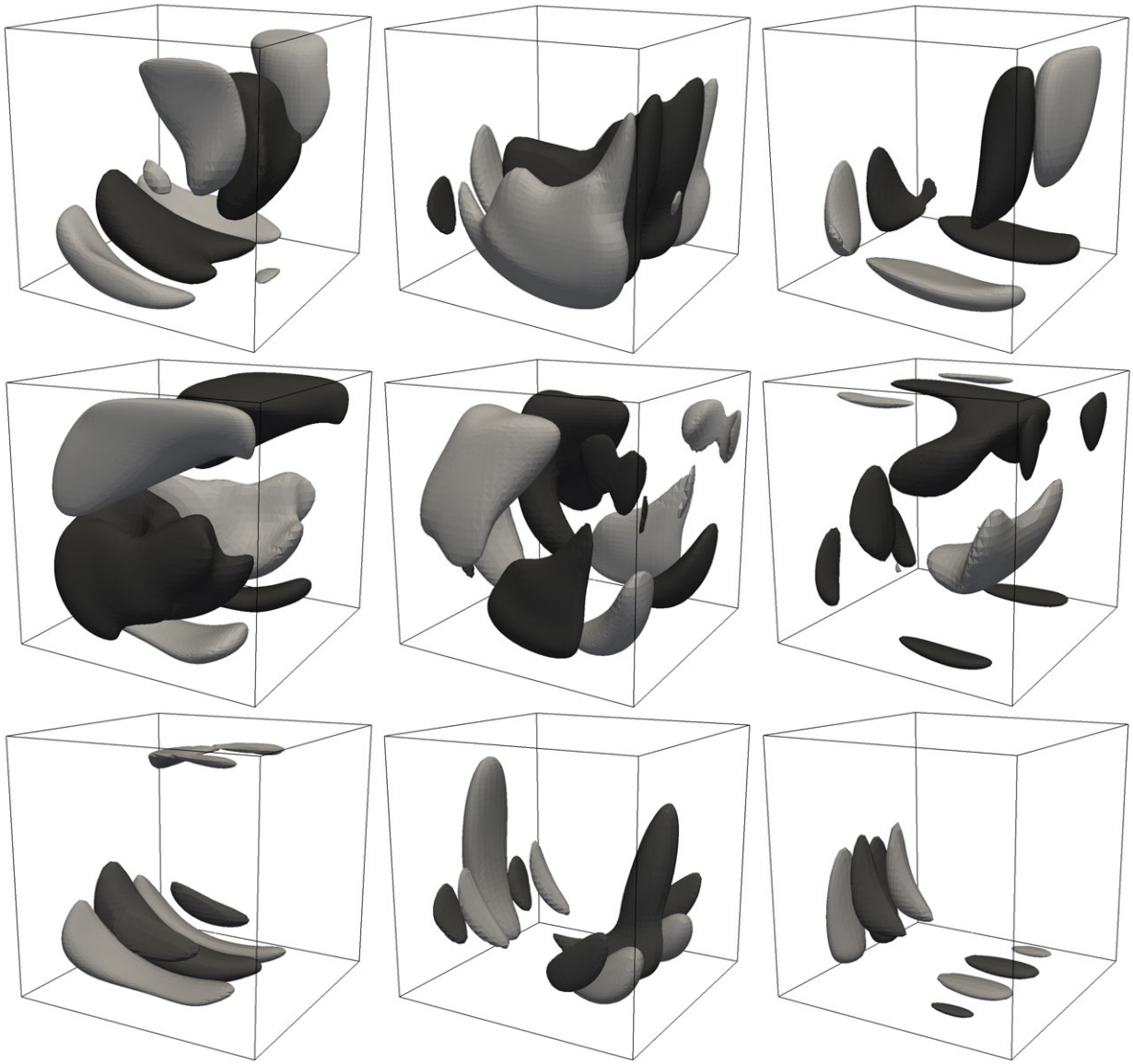

Figure 6.5: Real part of the eigenfunction velocity field $(\hat{u}, \hat{v}, \hat{w})$ of the cubic lid-driven cavity at $Re = 1000$. Eigenfunctions normalized with $max(\hat{u})$, lid moves from left to right. Resolution $N^3 = 96$. *(top):* $\lambda_1 = -0.136 \pm i0.285$ showing $\hat{u}, \hat{v}, \hat{w} = \pm 0.3$ *(middle):* $\lambda_2 = -0.138 \pm i0.457$ showing $\hat{u}, \hat{v}, \hat{w} = \pm 0.3$*(bottom):* $\lambda_3 = -0.146$ showing $\hat{u}, \hat{v}, \hat{w} = \pm 0.15$

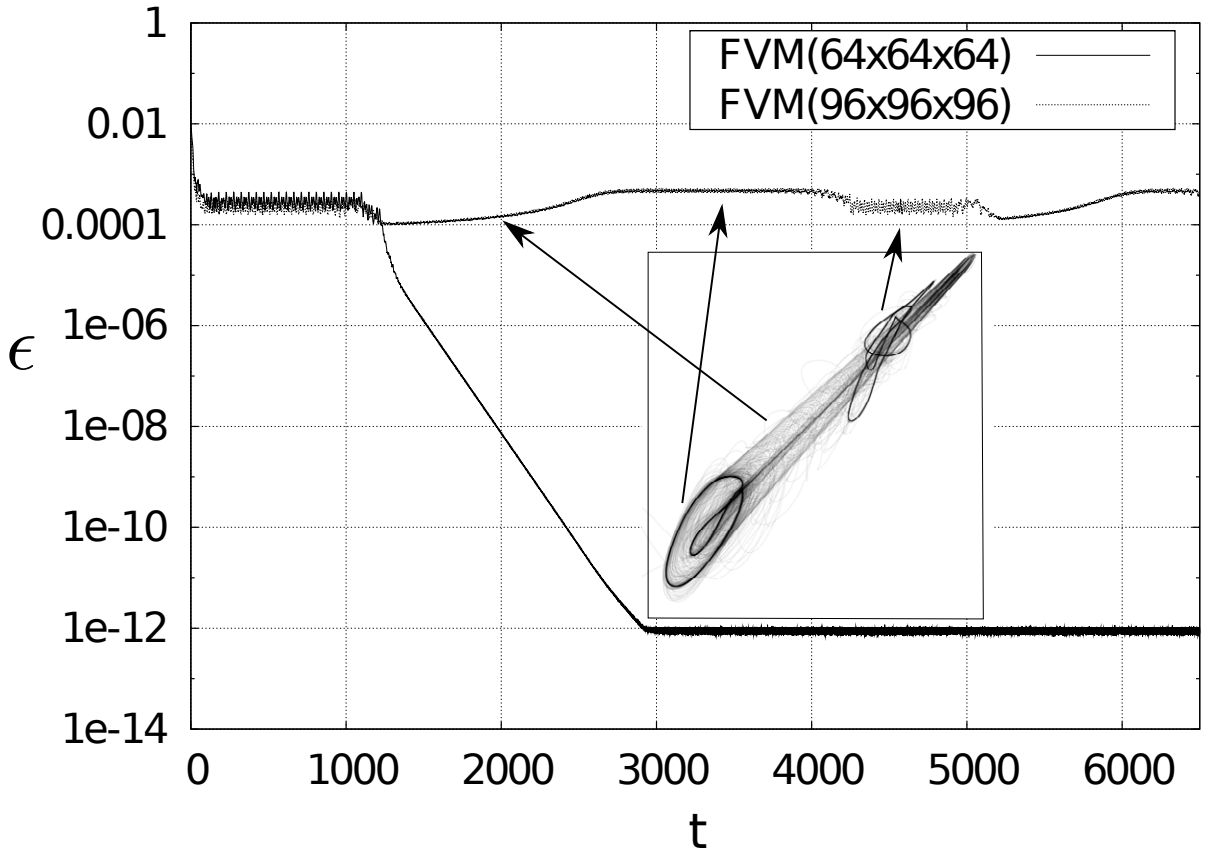

Figure 6.6: Temporal evolution of the velocity residual of the cubic three-dimensional singular lid-driven cavity at $Re = 2000$

meshes. The flow is shown to be stable using the coarsest resolution of $N^3 = 64$, a fact which can be attributed to the insufficient resolution to capture the salient flow features. Figure 6.6 also shows that the residual decays with a damping ratio of $O(10^{-2})$ and that the mode is traveling. A stability analysis of the obtained steady base flow provides a traveling mode with a eigenvalue $\lambda_1 = 0.0095 \pm i0.091$ and the corresponding eigenfunction with TGL shape is shown in Figure 6.8. It needs to be noticed that the discrepancy in the obtained instability results using the mesh M3 has the same order of magnitude than the damping ratio and thus only affects this, while the obtained frequency, with a bigger order of magnitude, is not affected by this discrepancy and is in good agreement with the results found by Liberzon, Feldman and Gelfgat [29, 30] .

In addition, results in Figure 6.6 show that the flow is non-linear at $Re = 2000$ using a resolution of $N^3 = 96$ and three different oscillatory regimes can be identified: a) an unstable oscillatory flow, the frequency of which matches that of the leading eigenmode, b) the corresponding linear saturation of this mode and c) a quasi-steady oscillatory regime with a smaller frequency. The temporal evolution of the residual of these three regimes is shown in detail in Figure 6.7. This behavior of the flow has been described as competition between modes with different pairs of TGL vortices by Aidun et al. [128], Guermond et al. [129] or as steady-oscillatory transition by Liberzon, Feldman and Gelfgat [29, 30], with the presence of a steady-mode. Although the accurate physical

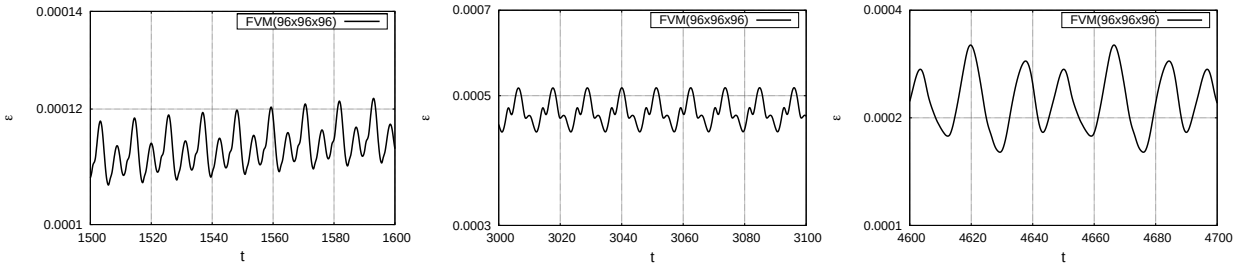

Figure 6.7: Three different states in the temporal evolution of the velocity residual of the cubic three-dimensional singular lid-driven cavity at $Re = 2000$ zoomed from Figure(6.6)

interpretation of these numerical results lies beyond the objective of this thesis, these phenomena could be explained with the existence of a limit cycle, as Figure 6.6 shows.

The steady-state solver of OpenFOAM® based on the SIMPLE method [91] has been employed to calculate an unstable steady base flow at $Re = 2000$ and resolution $N^3 = 96$, however the difference between the obtained results with the transient solver and the steady-state solver has an order of magnitude of (10^{-4}) and this difference is bigger than the magnitude of the small initial linear perturbation that needs to be superimposed upon the base flow in order to study the instability of the flow. Thus the base flow obtained with the steady-state solver of OpenFOAM® cannot be analyzed with the present instability methodology.

Next, the flow features of lid-driven cavities with aspect ratio different to unity have been explored for the first time in a global instability analysis context using the proposed methodology. Regarding the spatial structure of the eigenfunctions of large aspect ratio cavities, the existing pattern of different n-cell symmetric and asymmetric families of modes can be found in all aspect ratios studied. As an example, the two least-stable eigenfunctions of the lid driven cavity of aspect ratio $AR = 1 : 1 : 2$ and $AR = 1 : 1 : 3$ at $Re = 1000$ are shown in Figure 6.9 and Figure 6.10, where symmetric and asymmetric n-cell patterns of TGL vortices can be observed. The corresponding damping ratios of the leading eigenvectors at this Reynolds number are $\lambda_1 \sim 0.05$ for the $AR = 1 : 1 : 2$ cavity and $\lambda_1 \sim 0.03$ $AR = 1 : 1 : 3$ cavity. These modes are in agreement with the damped TGL flow structures found in the start-up experiments and simulation carried out by Aidun et al. [128], Guermond et al. [129] and Migeon [130].

Moreover, Table 6.4 contains the three least-stable eigenvalues of different aspect ratio lid-driven cavities at a low Reynolds number $Re = 200$, where the strong influence of the wall on the flow stability may be appreciated. It is remarkable that the cavity of $AR = 1 : \frac{1}{3} : \frac{1}{3}$ is one order of magnitude more stable than the cubic lid driven cavity, which is agreement with the findings of Albensoeder and Kuhlmann [141], who showed that TGL vortices are not formed close to the wall-end in large aspect ratio cavities. Next, independent increases of the aspect ratio parameters A_z or A_y have been performed in order to document their effect on flow stability. It was found that an increase in aspect ratio decreases the stability of the flow in both directions, as can also be seen in Table 6.4. As a mere exercise, the residual of very long cavities of aspect ratio up to $AR = 1 : 1 : 40$ has been also investigated, finding a damping ratio very close to that obtained by BiGlobal linear analysis of spanwise homogeneous flows [112] $\lambda_1 = 0.3297$.

Finally a study of the computational cost for the analysis using the proposed algorithm is shown in Table 6.5. Information is provided on the required CPU time T_{total} and RAM memory for

Table 6.4: Effect of aspect ratio $AR = 1 : A_y : A_z$ on the first three leading eigenvalues of the lid driven cavity at $Re = 200$

$AR = 1 : A_y : A_z$	λ_1	λ_2	λ_3
1:1:∞	-0.332 $\pm i$0.000	-0.551 $\pm i$0.000	-0.981 $\pm i$0.034
1:$\frac{1}{3}$:$\frac{1}{3}$	-2.111 $\pm i$0.449	-2.285 $\pm i$0.289	-2.710 $\pm i$0.690
1:1:1	-0.403 $\pm i$0.132	-0.435 $\pm i$0.000	-0.547 $\pm i$0.188
1:1:2	-0.310 $\pm i$0.000	-0.337 $\pm i$0.146	-0.369 $\pm i$0.276
1:1:3	-0.278 $\pm i$0.000	-0.332 $\pm i$0.120	-0.352 $\pm i$0.000
1:2:1	-0.240 $\pm i$0.000	-0.322 $\pm i$0.000	-0.324 $\pm i$0.058
1:3:1	-0.235 $\pm i$0.000	-0.239 $\pm i$0.000	-0.256 $\pm i$0.000

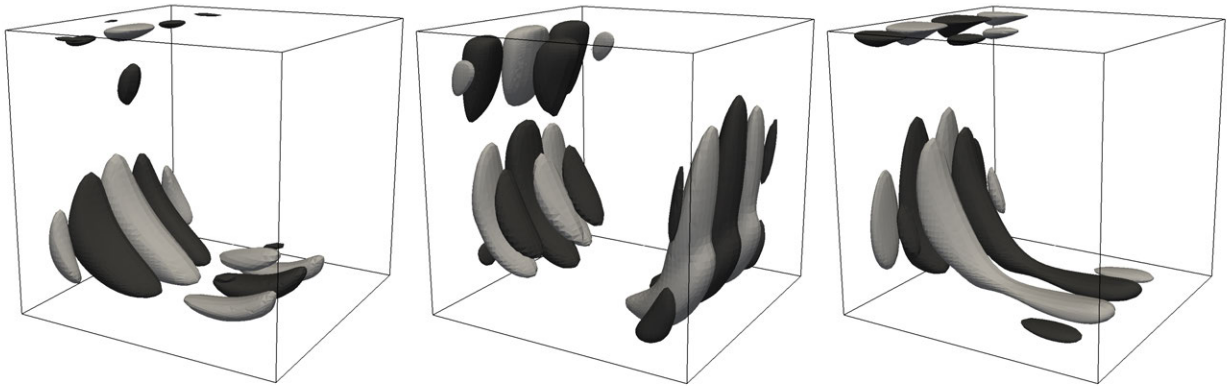

Figure 6.8: Real part of the eigenfunction velocity field $(\hat{u}, \hat{v}, \hat{w})$ of the cubic lid-driven cavity at $Re = 2000$. Eigenfunction normalized with $max(\hat{u})$. Showing $\hat{u}, \hat{v}, \hat{w} = \pm 0.1$, lid moves from left to right. $N^3 = 64$. $\lambda_1 = -0.095 \pm i0.091$

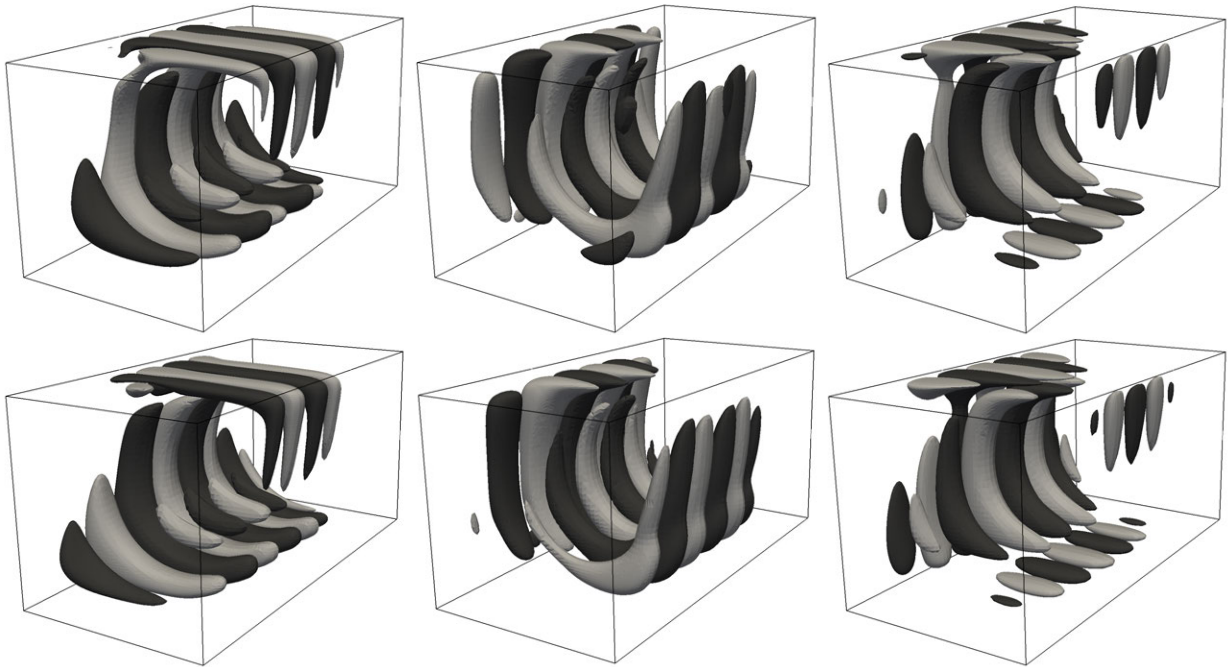

Figure 6.9: Real part of the eigenfunction velocity field $(\hat{u}, \hat{v}, \hat{w})$ of the leading (*top*) and second (*bottom*) eigenmodes of the $AR = 1:1:2$ lid-driven cavity at $Re = 1000$. Eigenfunctions normalized with $max(\hat{u})$. Showing $\hat{u}, \hat{v}, \hat{w} = \pm 0.1$, lid moves from left to right.

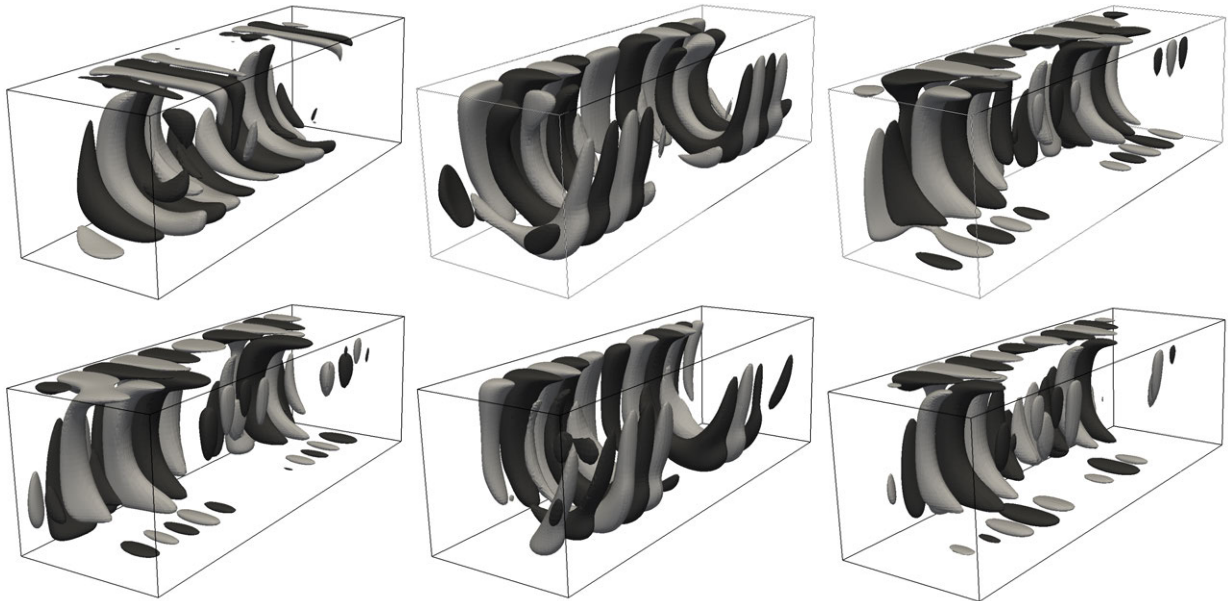

Figure 6.10: Real part of the eigenfunction velocity field $(\hat{u}, \hat{v}, \hat{w})$ of the leading (*top*) and second (*bottom*) eigenmodes of the $AR = 1:1:3$ lid-driven cavity at $Re = 1000$. Eigenfunctions normalized with $max(\hat{u})$. Showing $\hat{u}, \hat{v}, \hat{w} = \pm 0.1$, lid moves from left to right.

Table 6.5: Computational costs of the instability analysis of the cubic LDC at $Re = 1000$ with $m = 12$ and $\tau = 40$ using different resolutions in a 8-processor workstation

Mesh	N^3	Δt	$T_{step}(s)$	$T_{total}(h)$	Memory (GB)
M1	216^3	0.006	299.0	$O(10^5)$	30.1
M2	144^3	0.025	21.8	~ 232	9.9
M3	96^3	0.05	14.1	~ 75	3.6
M4	64^3	0.1	2.7	~ 7.2	1.2

a stability analysis of the cubic LDC with each of the employed meshes using a Krylov subspace dimension $m = 12$ with an integration time $\tau = 40$. In addition, the required CPU time T_{total} for a complete instability analysis can be estimated as:

$$T_{total} \sim \frac{2m\tau T_{step}}{\Delta t}\,, \tag{6.6}$$

T_{step} being the employed CPU time by the solver for one numerical time step.

All simulations have been run in parallel on a 8-core workstation with 32 GB RAM memory. It is remarkable that the CPU time has been reduced by an order of magnitude because of the good properties of the employed mesh; due to the orthogonality of the mesh and its $1:8$ stretching towards the walls, it has been able to set a maximum CFL number as $CFL \sim 10$, avoiding numerical oscillations. This has been tested performing analysis using mesh $M4$ with $CFL < 0.3$ and $CFL \sim 10$, providing identical results. Moreover, it is also shown that calculation with resolutions beyond $N^3 = 144$ are not feasible in reasonable CPU times and even can lead to lack of RAM memory issues. These findings represent the limits of the proposed methodology, if reasonable computing times are to be employed for the instability analysis of three-dimensional laminar flows.

Chapter 7

Time-stepping for TriGlobal Instability Analysis of Open Flows

Having identified the limits of serial performance of the matrix-forming algorithm and its applicability to TriGlobal problems, attention is finally turned to the open flows using the present time-stepping approach for the recovery of its global eigenspectrum. The flow past a cylinder fitted with helical strakes and the flow over an inhomogeneous open cavity will be studied next applying the present methodology.

7.1 Cylinder fitted with Helical Strakes

Helical strakes [145] are surface protrusions placed as helices in the spanwise direction around the surface of cylindrical structures. The geometry of the strakes is shown in Figure 7.1 and is characterized by the number of strakes n_s, the strake pitch p, the strake height h and the cylinder diameter d. These helical strakes are the devices most employed in order to affect the separation lines and separated shear layers and thus mitigate or altogether suppress vortex shedding in a wide range of Reynolds numbers. Interest in these devices arises on account of the multiple applications associated with cylinder wake manipulation, especially in the context of vortex-induced vibrations [146] (VIV) of drilling risers. In particularly, in a VIV context, strong interest exists on account of the fact that such vibrations can induce structural damages due to fatigue failures.

Several experiments have been performed in the past in order to predict the performance of

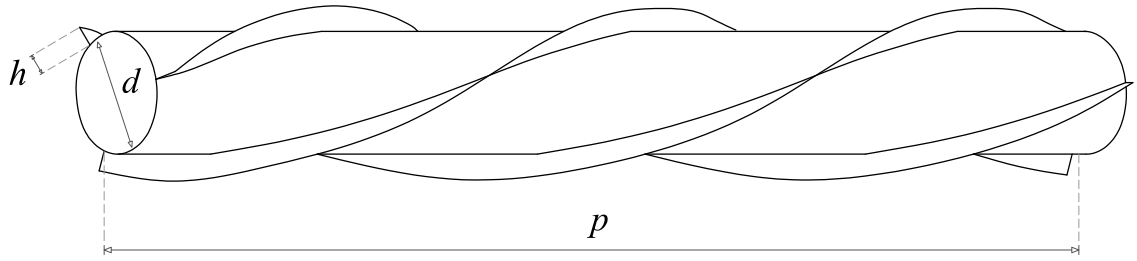

Figure 7.1: Geometry of a circular cylinder fitted with helical strakes

helical strakes. Zdravkovich [147] was the first to present a review of the state-of-the-art in the use of different devices in the mitigation of vortex shedding, proving the efficiency of the three helical strakes (THS) configuration. Results show that the strake height h has a major role in vortex shedding control. Particularly, increases in strake height mitigate instabilities and beyond a certain height the vortex shedding is almost suppressed. However, high height strakes also significantly increase the drag coefficient. It was also found that the strakes lose efficiency when the straked cylinder is placed in an oscillatory wake from another cylinder or when the upstream flow is very turbulent. Zdravkovich was also the first to qualitatively describe the physical mechanisms of vortex shedding suppression in terms of entrainment layer and confluence points, suggesting that vortex shedding can be mitigated by interfering the upstream shear layers and/or preventing their confluence.

Investigation on optimum pitch and strake height was first carried out by Scruton [148], and many others as reviewed by Zdravkovich [147], pointing out the effectiveness of the THS configuration. However, while some authors agreed that the optimum configuration for suppressing the oscillation was a three helical system with pitch between $p = 4d$ and $p = 5d$, with a height of $0.1d$, others suggested that the efficiency depends on each particular configuration. In this aspect, the early work of Ishizaki et al. [149] is also relevant, in that these authors found a slight improvement in instability control by using four instead of three strakes, with a pitch angle of 40° and a height bigger than $0.075d$. However, it should be mentioned that this experiment was carried out using tapered cylinders. More recent experiments showing the effectiveness of the THS were carried out by Allen et al.[150], Trim et al.[151], Brankovic et al.[152], Lubbad et al. [153], Korkischko & Meneghini [154] and Zhou et al.[155]. Lubbad et al. [153] performed experiments concluding that the optimum configuration corresponds to three strakes with a pitch of $5d$ and a strake height of $0.15d$, which is in agreement with the early results summarized by Zdravkovich [147]. Independently, Korkischko & Meneghini [154] performed an extensive assessment of the strakes effectiveness by varying the strake geometric parameters and confirming that a strake with $h = 0.1d$ moderately mitigates the vibration and beyond $h = 0.2d$ almost suppress the vortex-induced flow-induced vibrations, and that the pitch has no apparent effect on high-height strakes while increases in pitch for $h = 0.1d$ has a positive effect. In addition, these experiments show that the strakes prevent shedding from becoming correlated along the spanwise direction and the three-dimensionality of the separated flow created by the strakes destroys regular vortex shedding. Zhou et al.[155] performed wind-tunnel experiments with a $p = 10d$ bare and straked cylinder reaching similar conclusions about the VIV suppression. In addition, they performed flow visualization using smoke wire of the bare and straked cylinder at $Re = 300$ and were able to show the different structures between the two cylinders. This is the only work known that qualitatively describes the three-dimensional straked cylinder flow at low Reynolds number.

Constantinides & Oakley [156] performed the first numerical simulation of the flow around a straked cylinder. They carried out high Reynolds ($Re = 10^6$) simulations using RANS and DES turbulence models. Their simulation showed that the strakes induce a wave length of one third of the pitch and a significant flow in the spanwise direction, preventing the formation of coherent structures in the wake. Similar findings were obtained by Korkischko & and Meneghini [157] by means of the volumetric reconstruction of the mean flow around circular cylinder fitted with strakes from experiments at $Re = 1000$ and $Re = 10000$. Korkischko & and Meneghini [157] also found that the helical strakes prevent the formation of strong vortices near the base of the cylinder. Carmo et al. [158] carried out two and three dimensional simulations of the flow around a straked cylinder at a moderate Reynolds number $Re = 1000$ reaching similar conclusions and identifying two

physical mechanisms. First, the decrease in vortex shedding correlation in the spanwise direction and second, that the strakes increase the distance between the two separated shear layers, limiting their interaction and making the formation of vortices to occur further downstream.

From a dynamical system analysis point of view, extensive research has been done for the bare cylinder case [159, 160, 33, 161, 162, 163, 164, 165, 166, 167, 168]. It is very well known that flow remains steady and homogeneous in the spanwise direction until Reynolds number $Re \sim 46$. Beyond this Re number the flow undergoes a Hopf bifurcation that leads to an oscillatory state homogeneous in the spanwise direction, known as the Von Karman vortex street. This oscillatory state loses stability to finite-amplitude disturbances in the spanwise direction beyond $Re = 188.5$ [169] and another primary bifurcation occurs, known as mode A. This mode linearly saturates the flows and the flow loses homogeneity in the spanwise direction. Secondary subsequent bifurcations with short-wavelengths occur at $Re = 259$, known as mode B [170, 21] and tertiary bifurcations corresponding to quasi-periodic (QP) modes appear beyond $Re = 377$ [171]. This extensive knowledge in the cylinder wake dynamics have been possible mostly because of the application of global instability analysis which, in case of time-periodic flows must be performed in a Floquet analysis context.

As an example of the application of the Global (and Floquet) instability analysis in this kind of flows, Barkley & Henderson [21] employed this theory to study the stability of the cylinder wake, successfully reporting for first time the two three-dimensional secondary instability modes existent at low Reynolds that were identified in earlier transition experiments [170]. This finding was an important breakthrough in the quest of understanding the sequence of instabilities leading to a turbulent wake. However, it has to be noticed that most of the computational results obtained for the cylinder dynamics has been possible by exploiting the temporal and spatial symmetries of the flow. For example, Barkley [172] studied the properties of the primary instability mean flow by means of the spatial symmetry and Blackburn et al. [172] performed a Floquet analysis based on a half-period-flip map to recover the modes QP that arise from secondary or tertiary bifurcation of the three-dimensional cylinder wake flow. None of these approaches can be applied to the cylinder fitted with helical strakes because of its spatial three-dimensional inhomogeneity.

Despite the extensive above-mentioned studies on the bare cylinder wake, no work is known to date that deals with the effect on the strakes on the different bifurcations of the wake flow past the cylinder. Several questions are open in this context:

- Is the primary instability onset the result of a local or a global bifurcation?
- Does a global mode exist, with a unique frequency or are there different vortex shedding modes, operative at different locations with different shedding frequencies?
- How does three-dimensionality affects the von Karman street once this loses stability to finite-amplitude spanwise disturbances?
- And finally, can any of these results provide insight in the VIV reduction caused by the presence of the strakes?

The goal of the present chapter is to address these open questions by performing Direct Numerical Simulation and Global stability analysis theory to the flow around a cylinder fitted with helical strakes in order to understand more deeply the flow instabilities and physical mechanisms identified in the literature that mitigate and suppress the vortex shedding.

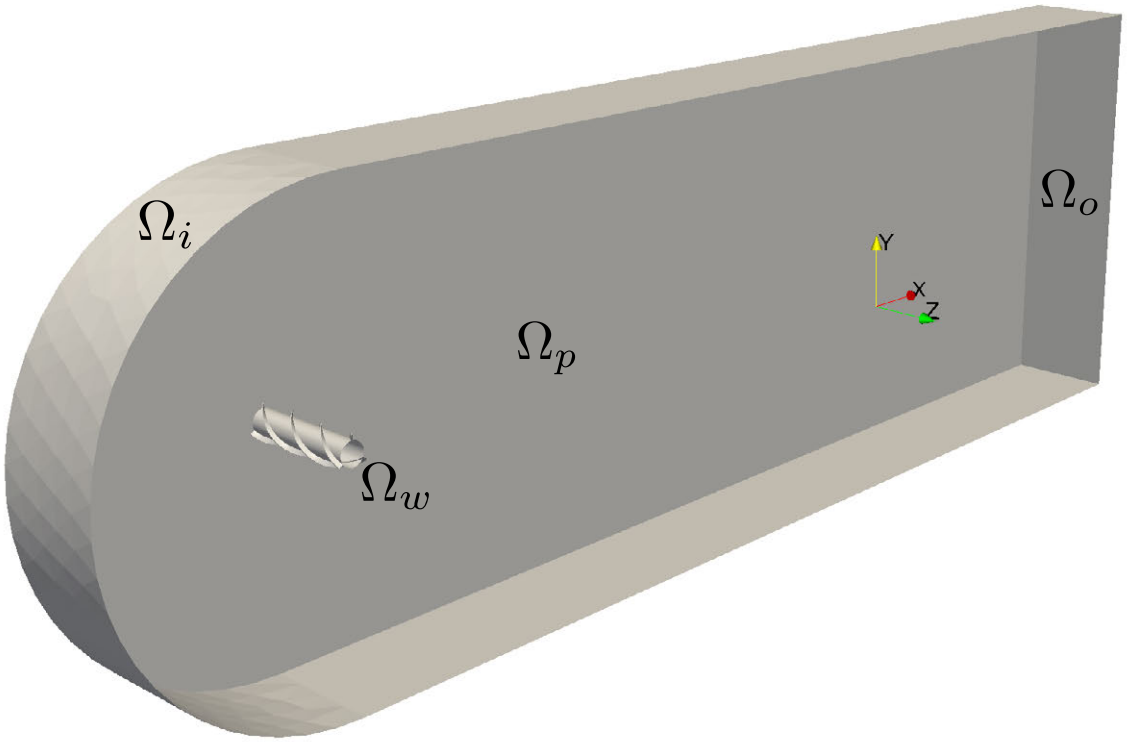

Figure 7.2: Employed domain for the simulation of flow past a cylinder fitted with helical strakes

7.1.1 Base Flow

The flow past a cylinder fitted with helical strakes is described by the three-dimensional and dimensionless Navier–Stokes (2.28) with the Reynolds number defined as:

$$Re = U_\infty d/\nu\,, \tag{7.1}$$

U_∞ being the free stream velocity, d the cylinder diameter, ν the kinematic viscosity. Figure 7.2 shows the computational domain and boundaries employed for the direct numerical simulation of the flow. The boundary condition for the Navier–Stokes are inlet for boundary Ω_i, periodic boundary conditions for the domain sides Ω_p, no-slip for the cylinder with strakes Ω_w and outlet for the rear part of the domain Ω_o, which follows:

$$\begin{array}{cccc}
\mathbf{u}(x,y,z) = (1,0,0), & \frac{\partial p(x,y,z)}{\partial \mathbf{n}} = 0 & \text{on } \Omega_i \\
\mathbf{u} = (0,0,0), & \frac{\partial p(x,y,z)}{\partial \mathbf{n}} = 0 & \text{on } \Omega_w \\
\mathbf{u}(x,y,0) = \mathbf{u}(x,y,5), & p(x,y,0) = p(x,y,5) & \text{on } \Omega_p \\
\frac{\partial \mathbf{u}}{\partial \mathbf{n}} = 0, & p(x,y,z) = 0 & \text{on } \Omega_o\,.
\end{array}$$

C-meshes for the bare cylinder have been created in order to deal with the helical strakes in three-dimensions in a consistent way avoiding skew volumes. In order to test the mesh convergence, the grid refinement study based on a generalized Richardson extrapolation method [144] as used by in Chapter 6 has been employed. Table 7.1 presents convergence results obtained with the OpenFOAM® solver for four different meshes of a bare cylinder with a pitch $p = 5d$ at $Re = 40$.

Table 7.1: Grid convergence study based on drag coefficient C_D for the bare cylinder at $Re = 40$ using three meshes: M1 finest, M2 fine, M3 medium and M4 coarse. Grid convergence index obtained with $l = 2^{1/3}$ and $n = 1.83$

Mesh	n_r	n_θ	n_z	Number of nodes	C_D	$GCI_{j+1,j}(\%)$
M1	131	87	87	$\sim 1 \times 10^6$	1.51536	0.43
M2	104	68	68	$\sim 5 \times 10^5$	1.51626	0.58
M3	83	54	54	$\sim 2.5 \times 10^5$	1.51746	0.98
M4	66	43	43	$\sim 1.2 \times 10^5$	1.51949	-

It can be seen that the GCI based on the drag coefficient C_D indicates than the mesh M3 with $\sim 2.5 \times 10^5$ cells is enough to accurately predict the flow quantities around the cylinder surface and that doubling the mesh resolution only leads to slight improvements in accuracy. The computational domain size of the baseline mesh has been chosen as $d_i = 10d$ for the inlet boundary Ω_i and Ω_o has been placed at $d_o = 50d$ from the straked cylinder origin, taking into consideration the recent work of Barkley & Henderson [21] and Giannetti & Luchini [168]. This domain is shown in Figure 7.2. The steady base flow solutions obtained with the OpenFOAM® solver in the convergence test have been validated against the solutions available at the literature for the bare cylinder case. Results shown in Table 7.2 present an excellent agreement between the drag coefficient C_D obtained and the recirculation bubble length with those results found on the literature.

Table 7.2: Comparison with previous results based on drag coefficient C_D and length of the separation bubble L_w measured from the rear stagnation point

Author	Cylinder Type	Re	C_D	L_w
Kim et. al [165]	bare	40	1.51	-
Ye et. al [163]	bare	40	1.52	2.27
Giannetti et al. [168]	bare	40	1.54	2.24
Present results (M3)	bare	40	1.51	2.21

Besides resolution, the slight discrepancies may come from performing a three-dimensional simulation with periodic boundary conditions instead of a two-dimensional simulation. In addition, drag coefficient C_D and Strouhal number St results using this resolution and domain size are shown in Figures 7.6 and 7.7 *left* respectively, where a reasonable agreement with the extensive results available in the literature can be inferred. Although further convergence analysis based on the Strouhal number $St = fd/U_\infty$ and a flow quantity located in the wake for the detection of blockage, outflow or artificial dissipation effects may be needed for a accurate calculation of the onset of the instability, the domain employed is enough for the present goal of this thesis. The C-mesh for the cylinder fitted with helical strakes has been constructed using a similar resolution as the one of the near-wake region in mesh M3 in order to ensure that the flow around the cylinder surface retains grid convergence. This mesh is shown in Figure 7.3 and corresponds to a straked cylinder with a number of strakes $n_s = 3$, a strake pitch $p = 5d$, a strake height $h = 0.2d$ and a cylinder diameter $d = 1$.

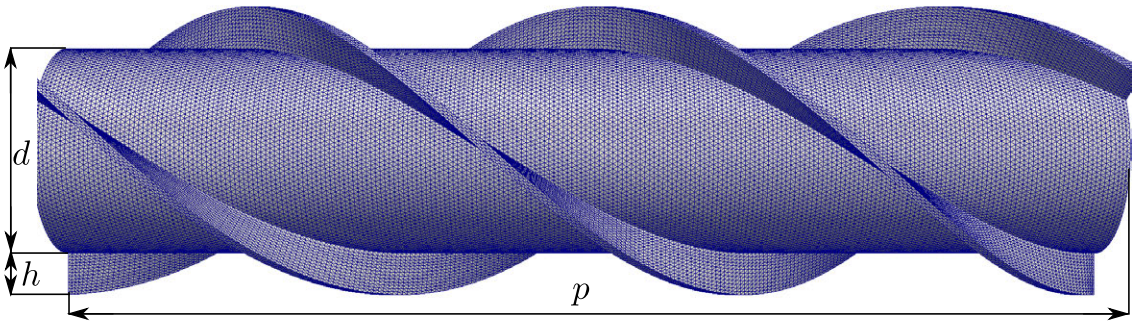

Figure 7.3: Geometry and Mesh of the cylinder fitted with helical strakes created by using a cylindrical mesh with helical splines. Current geometry with $n_s = 3$, $h = 0.2d$, $d = 1$ and $p = 5d$.

7.1.2 Instability Analysis

The effects of fitting straight strakes in the cylinder at different phase angle θ have been studied previously to the helical strakes in order to isolate the effect of change in phase angle. This phase angle θ is defined as the angle that the upstream strake forms with free-stream velocity. Table 7.3 shows a comparison between the drag coefficient, Strouhal number and wake length of the bare cylinder and cylinders fitted with three straight strakes at different phase angles with a span of $p = 5d$.

Table 7.3: Time averaged drag coefficient C_D, Strouhal number St and recirculation bubble length L_w of a two-dimensional cylinder fitted with straight strakes at different phase angle θ, $Re = 40$ and $p = 5d$

Cylinder Type	θ	C_D	St	C_L
bare	-	1.51	steady	0
straight strakes	0°	1.66	steady	0
straight strakes	15°	1.70	0.101	0.502
straight strakes	30°	1.76	0.098	0.784
straight strakes	45°	1.92	0.096	0.565
straight strakes	60°	2.03	0.094	0
helical strakes	-	1.94	0.087	0

These results indicate than the phase angle has a strong influence on how the strakes modify the flow around the cylinder. For example, the flow remains steady at phase angle $\theta = 0°$, while it is unsteady at different phase angles. Figure 7.4 shows instant snapshots of the streamwise vorticity component and streamlines of the flow around a cylinder fitted at plane $z = 5$ with straight strakes at different phase angles at $Re = 40$ $p = 5d$.

It can be seen that for asymmetric configurations in the streamwise direction at this Reynolds number, vortex shedding occurs behind the most upstream strake in such a way that the interaction of the wake with the shear layer that goes through the second most upstream is reduced. It remains to be discovered whether the vortex shedding starts at a determined location or as a global mode.

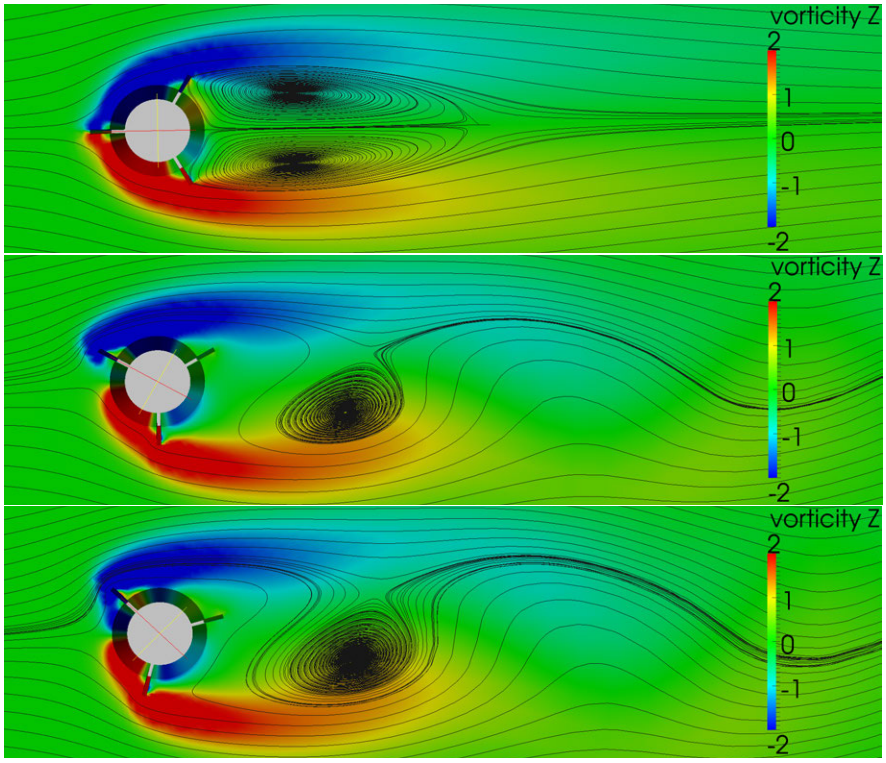

Figure 7.4: Instant snapshots of the streamwise vorticity component and streamlines at plane $z = 5$ of the flow around a cylinder fitted with straight strakes at different phase angles at $Re = 40$ $p = 5d$. *(top)* $\theta = 0°$ *(middle)* $\theta = 30°$ *(bottom)* $\theta = 45°$

As observed in previous works [158, 155], drag coefficient C_D also significantly changes with the phase angle. In addition, strakes increased the drag coefficient at the same temporal state. It is also remarkable that the Strouhal number changes with the phase angle, so the change in vortex shedding frequency with the phase angle could explain the decrease in vortex shedding correlation along the span. These effects of the straight strakes homogeneous in the spanwise spatial direction on the cylinder flow features are in perfect qualitative agreement with the ones described using two-dimensional VIV analysis by Carmo et al.[158].

Complete fully three-dimensional time-resolved Direct Numerical Simulations have been performed from $Re = 20$ to $Re = 100$ employing the solver and meshes described in the previous section. Comparisons have been made against the flow of a bare cylinder with the same pitch $p = 5d$ as the straked cylinder. Given the formidable computational cost of performing a single TriGlobal linear modal instability analysis, a modification of the residual algorithm developed by Theofilis [1] have employed to calculate damping ratio and frequencies of the leading eigenmode past the critical Reynolds as a first step in the analysis. In order to extract the flow features from the Direct Numerical Simulation results, an implementation of the nonlinear least-squares (NLLS) Marquardt-Levenberg algorithm [173, 174] in conjunction with the residual algorithm developed by Theofilis[1] has been used. This least-squares fitting permits the identification of the linear regime of the growth of the leading eigenmodes before the corresponding linear saturation. As a conse-

quence of the linearization carried out in equation (2.32) and the ansatz (2.33), the residuals from the temporal integration of the drag coefficient defined as $C_L{}' = C_L(t+dt) - C_L(t)$ can be fitted to the sought solution as

$$C_L{}' = \epsilon \hat{C_L} \mathrm{e}^{\lambda_r t} \cos(2\pi St + \phi) \tag{7.2}$$

for the particular case of an unique oscillatory leading eigenvalue. The fitting is iteratively carried out until the the sum of the squared differences of the function χ^2 is less than 10^{-5} and the asymptotic standard error of each parameter $\epsilon\hat{C_L}$, λ_r, St and ϕ are less than 1%. Figure 7.5 shows the non-linear least-square fitting of the lift coefficient C_L residual of the flow past a straked cylinder at $Re = 40$ and $Re = 50$. For $Re = 40$ the fitting delivers as solution

$$C_L{}'(Re = 40) = 1.85410^{-4}\mathrm{e}^{-0.0174t} \cos(0.658 - 20.73)\,, \tag{7.3}$$

which corresponds to a damping ratio of $\lambda_r = -0.015$ and a Strouhal number of $St = 0.105$. Thus, the flow is steady at this Reynolds number. The solution of the fitting for $Re = 50$ is

$$C_L{}'(Re = 50) = 2.4610^{-4}\mathrm{e}^{0.015t} \cos(0.728 - 8.84)\,, \tag{7.4}$$

which delivers a growth ratio of $\lambda_r = 0.015$ and a Strouhal number of $St = 0.116$. The Direct Numerical Simulation shows that this leading eigenmode grows until saturation and the flow becomes periodic with the same frequency.

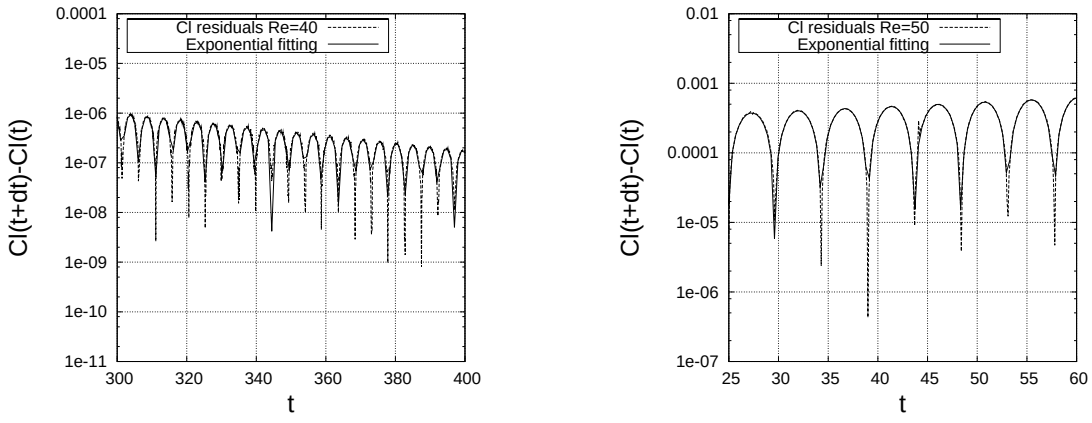

Figure 7.5: Non-linear least-square fitting of the lift coefficient C_L residual of the flow past a straked cylinder at *(left)* $Re = 40$ *(right)* $Re = 50$.

Figure 7.6 shows the comparison of average in time C_D drag coefficient between the straked cylinder and the bare cylinder using the results from the Direct Numerical Simulations and those available in the literature.

Besides noting that the drag coefficient is significantly bigger for the straked cylinder, which may be explained in terms of an increase in effective diameter of the straked cylinder due to the strakes, the most interesting aspect of the Figure 7.6 is that the changes in C_D slope behave similarly in both cylinders. Figure 7.7 *left* shows the results of this fitting for the St number from $Re = 20$ to $Re = 100$ and its comparison with the bare cylinder based on the results of Barkley & Henderson[172] and

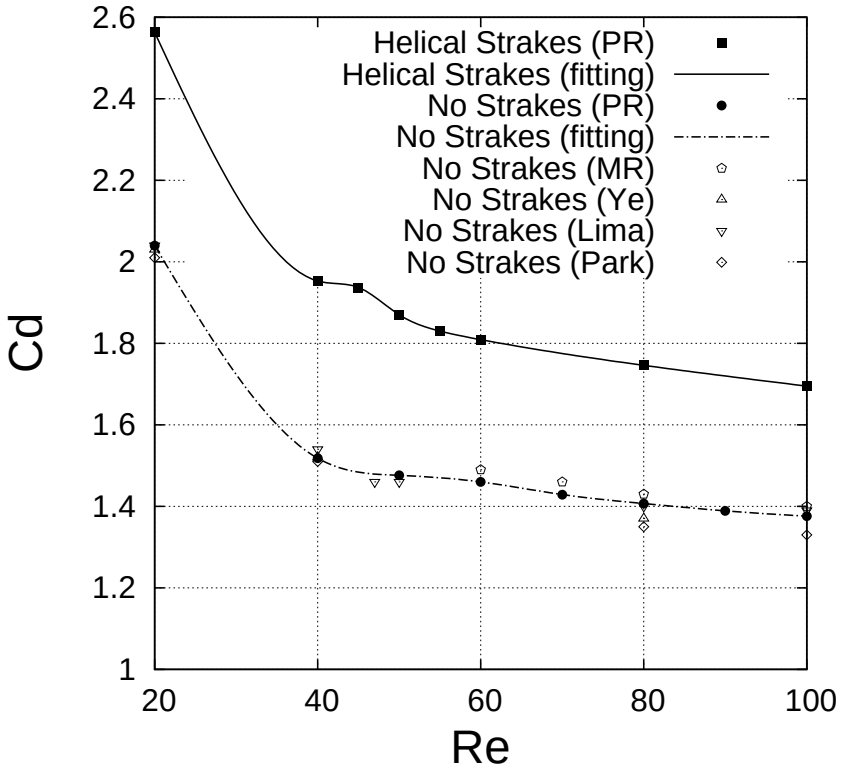

Figure 7.6: Comparison of average in time C_D drag coefficient between the straked cylinder and the bare cylinder. (PR) Present results, (MR) Mittal & Raghunvanshi, (Ye) Ye et al. [163], (Lima) Lima et al.[166] (Park) Park et al.[162]

Giannetti & Luchini [168]. The discrepancy of the bare cylinder results beyond the bifurcation at $Re = 47$ is explained by the different analysis carried out by the authors. Giannetti & Luchini provide the St of a unstable steady state solution while Barkley & Henderson[172] provide the St of the saturated base flow. Analogously, the present results for the straked cylinder are those of the stable steady or periodic base flow. Three different zones can be inferred from Figure 7.7 *left*: a large slope until $Re \sim 40$, a band with constant $St = 0.116$ until $Re \sim 55$ and a slow increase in St number beyond $Re \sim 55$. In order to interpretate the St results, the rest of flow features must be explained first.

Figure 7.7 shows the comparison of λ damping/growth rate between the straked cylinder and the bare cylinder. It can be seen that the leading eigenmode of the straked cylinder flow crosses the real axis at $Re_1 \sim 43$ which is a smaller critical Re than the one of the cylinder without strakes flow. Beyond this Re_1, the leading eigenmode grows and saturates the flow into an oscillatory flow with $St = 0.116$ as the Direct Numerical Simulation results shows.

In order to understand more deeply this first bifurcation of the flow, Global Stability Analysis using the time-stepping methodology have been carried out at $Re = 20$ and $Re = 40$. A Krylov subspace dimension $m = 20$ and an integration time of $\tau = 10$ have been required to accurately capture the first eigenmode. These analysis take $O(200)$ hours in a 12−core workstation.

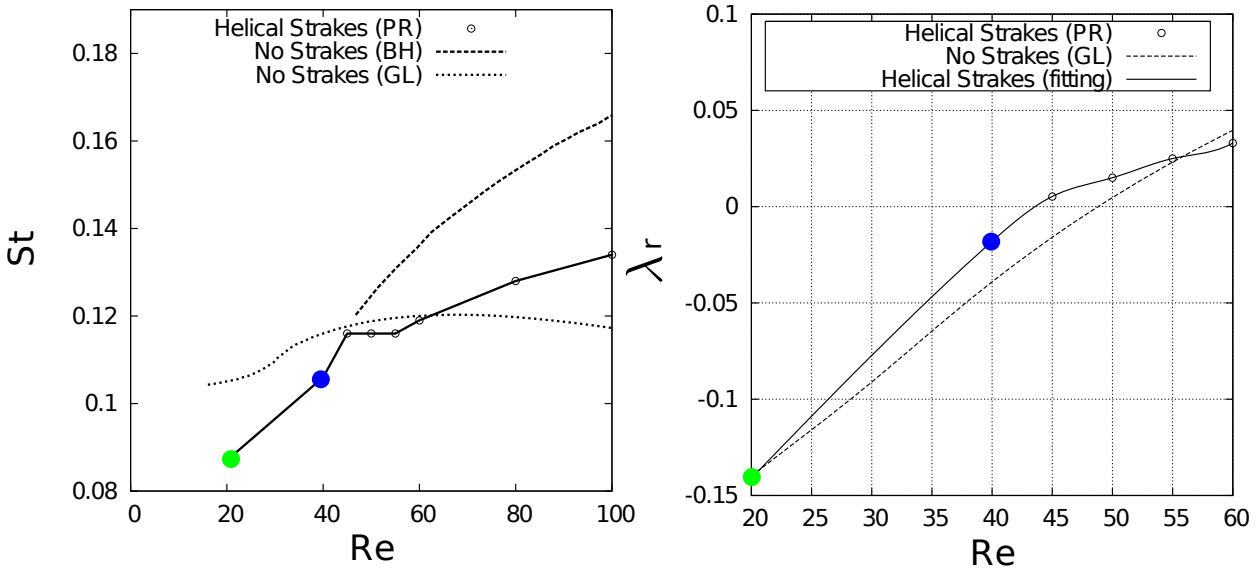

Figure 7.7: (*left*) Comparison of St number between the straked cylinder and the bare cylinder. (*right*) Comparison of λ damping/growth ratio between the straked cylinder and the bare cylinder. (PR) Present results (BH) Barkley & Henderson[172] (GL) Giannetti & Luchini [168]. ● $Re = 20$ $\lambda = -0.14$, $St = 0.087$ ● $Re = 40$ $\lambda = -0.017$, $St = 0.105$

The eigenvalues associated with the leading global modes of the flow at $Re = 20$ and $Re = 40$ recovered with the present methodology are represented in Figure 7.7 by a green and blue circle respectively. (7.8) shows the real part of the velocity eigenfunctions of the leading (damped) global eigenmode of the straked cylinder at $Re = 40$, which corresponds to a complex eigenvalue with a damping ratio of $\lambda = 0.017$ and a Strouhal number $St = 0.105$, which are in perfect agreement with the results from the Direct Numerical Simulations. This eigenfunction is similar to the classic Von Karman vortex street, however it is completely three-dimensional, as vortex shed from the upper part and bottom part of the cylinder have spanwise velocity components in opposite directions. Because of the existence of this global mode, it is stated that the flow undergoes a Hopf bifurcation and no local shedding is produced. Figure 7.9 shows the isosurface of spanwise velocity with a magnitude of more than 10% of the free-stream velocity at $Re = 100$ where this three-dimensionality is more clear. The three-dimensionality effects induced by the strakes vanish at a distance $x \sim 3d$ because of the high dissipation at this Reynolds number. It is also observed in Figure 7.7 *left* that the shedding frequency of the straked cylinder is around a 20% slower that of the bare cylinder. This effect may be related to the increase in effective diameter of the straked cylinder due to the strakes height. Figure 7.10 shows the difference between wakes of the bare cylinder and the straked cylinder at $Re = 100$, where the difference in shedding frequency are observed as well as the three-dimensionality features of the wake.

Next, additional three-dimensional time-resolved Direct Numerical Simulations have been performed from $Re = 100$ to $Re = 200$ in order to find subsequent bifurcations of the periodic state. The fitting technique based on residuals is not applicable now because of the appearance of additional frequencies and parameters, making the fitting problem ill-posed. Power density spectra obtained via FFT of the temporal evolution of the drag coefficient C_D are presented in Figure 7.11

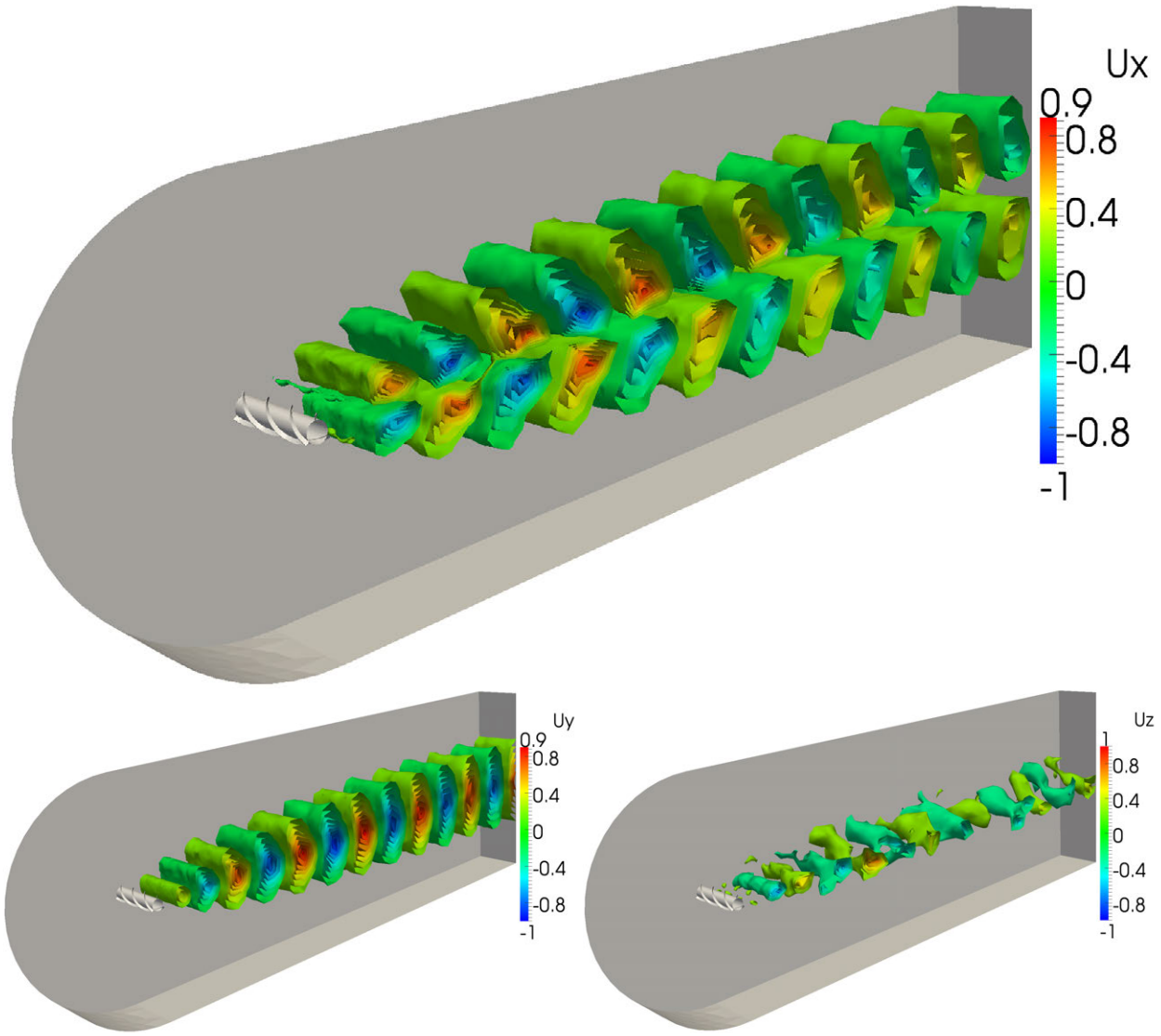

Figure 7.8: Velocity eigenfunctions of the leading (damped) eigenmode of the straked cylinder at $Re = 40$

for $Re = 120, 160$ and 200. The flow remains periodic until $Re = 120$. Beyond this Re number, the increase in Re has two consequences; the magnitude of the periodic oscillations with $St \sim 0.12$ is significantly reduced while two new frequencies appear. A very slow frequency $St \sim 0.035$ that becomes dominant as the Re is increased, and a faster frequency $St \sim 0.45$, that somehow interacts with the original shedding frequency, shifting its value and producing additional subharmonic frequencies, as it can be seen in the FFT of $Re = 200$.

Further instability analysis based on Floquet theory must be attempted in order to investigate this subsequent bifurcation. A Floquet analysis has been attempted in order to recover the least stable Floquet multipliers at $Re = 100$ using a Krylov subspace dimension ($m = 20$) and an integration time of $\tau = 1/St$. However these parameters have not been enough to accurately

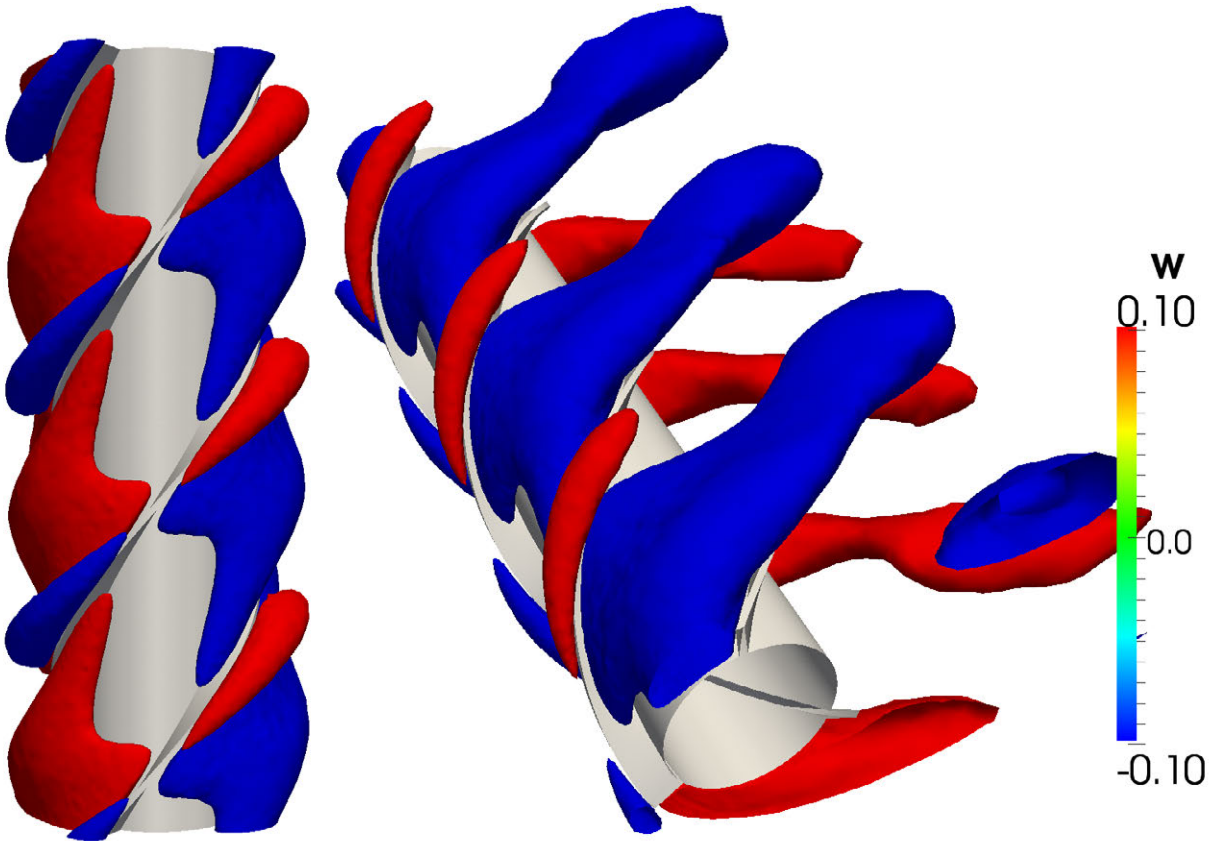

Figure 7.9: Isosurface of spanwise velocity $w = \pm 0.2$ at $Re = 100$ and bottom $w = \pm 0.1$

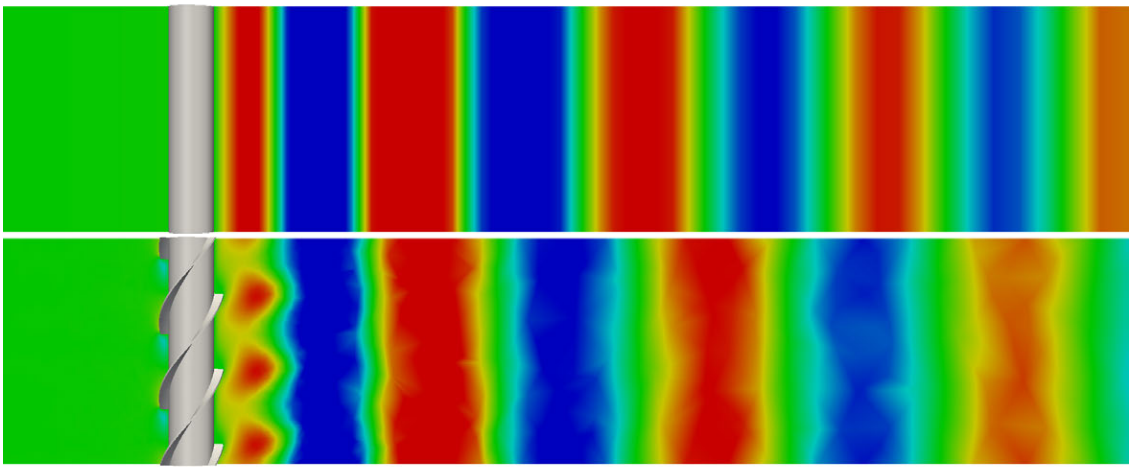

Figure 7.10: Difference between wakes of *(top)* Bare cylinder and *(bottom)* Straked Cylinder at $Re = 100$. $v = \pm 0.3$

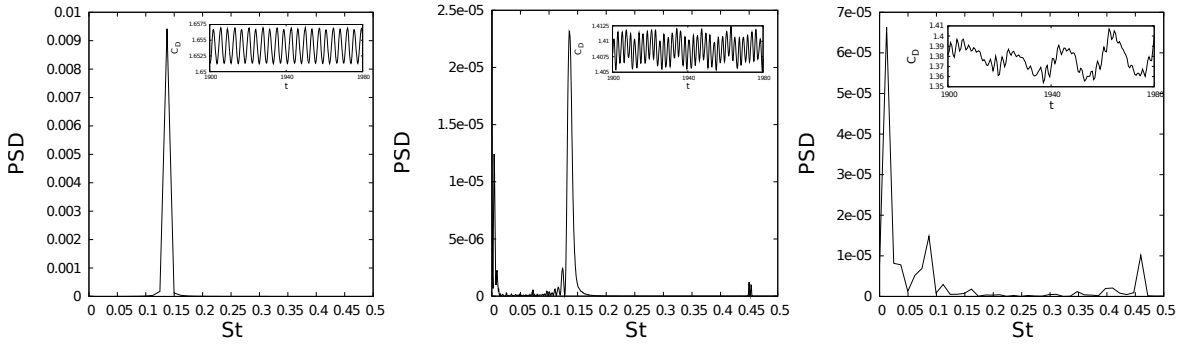

Figure 7.11: Power density spectrum of the drag coefficients C_D at (*left*) $Re = 120$ (*middle*) $Re = 160$ (*right*) $Re = 200$

capture the first Floquet mode and the lack of computational resources prevented this kind of analysis.

7.2 Flow over an inhomogeneous open cavity flow

Flow in a wide range of speeds around the three-dimensional open cavity configuration is relevant to store separation and, as such, has motivated extensive theoretical investigations over decades, focusing on both hydrodynamic [175] and aeroacoustic [176, 177, 8] aspects. Invariably, simplifying assumptions needed to be made, in tune with the theoretical/numerical capabilities of the respective era. Local linear theory based on variants of the Orr-Sommerfeld equation and its compressible counterpart, the Parabolized Stability Equations [178] and BiGlobal linear theory [176, 175, 179] have all been applied in the past in order to understand flow interactions in this problem. The assumptions underlying these theories are spatial homogeneity along two (the streamwise and spanwise) or one (the spanwise) spatial directions. Here, TriGlobal linear theory is employed for the first time to address linear instability of the inhomogeneous three-dimensional incompressible flow at a low Reynolds number, $Re = 100$, at which steady laminar flow can be obtained.

7.2.1 Base Flow

The flow over the open cavity is described by the incompressible Navier–Stokes equations (2.28) and the cavity Re number is defined with the length in the streamwise direction as reference length, in consistency with the lid-driven cavity geometry shown in Figure 6.1. Figure 7.12 shows a mesh constructed using the OF *blockMesh* utility around a three-dimensional open cavity of aspect ratio $AR = 1 : \frac{1}{5} : \frac{1}{5}$.

The domain above the cavity is defined between $x \in [-1, 2] \times y \in [-0.6, 0.6] \times z \in [0, 2]$, while the cavity itself is bounded by $x \in [-0.5, 0.5] \times y \in [-0.125, 0.125] \times z \in [-0.2, 0]$. Steady laminar incompressible flow at $Re = 100$ is obtained by imposing the following constant streamwise velocity component at $x = -1$ (Ω_i), outlet boundary conditions at $x = 2$ (Ω_o), slip boundary conditions at the sides and the top (Ω_s) and no-slip boundary conditions at the bottom wall (Ω_w). This follows:

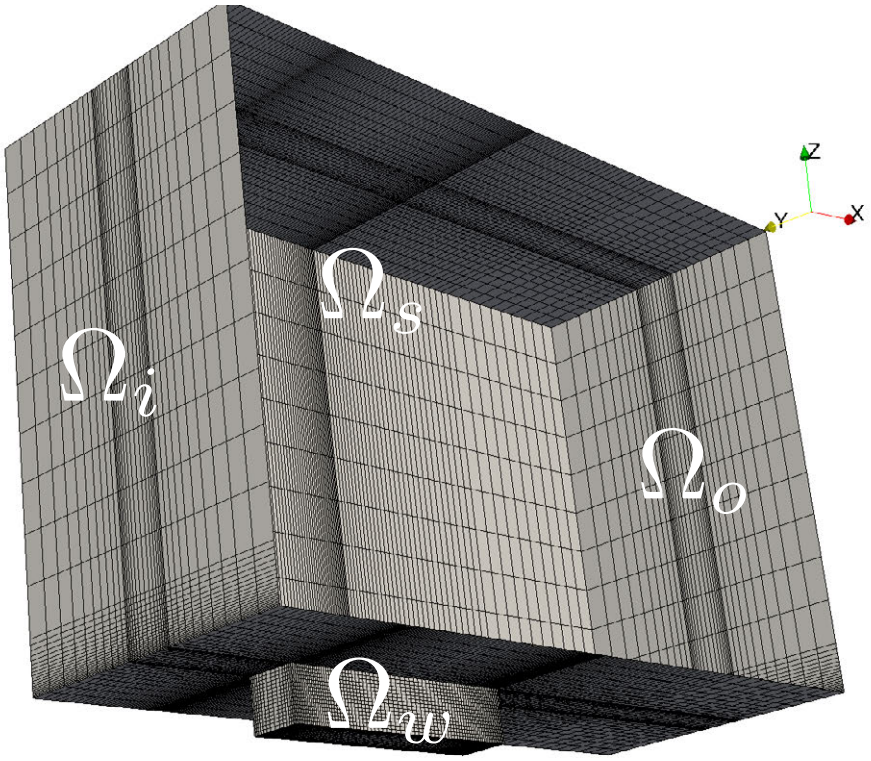

Figure 7.12: Employed domain and mesh for the simulation of flow over the three-dimensional $AR = 1 : \frac{1}{5} : \frac{1}{5}$ open cavity

$$
\begin{array}{cccc}
\mathbf{u}(x,y,z) = (1,0,0), & \frac{\partial p(x,y,z)}{\partial \mathbf{n}} = 0 & \text{on } \Omega_i \\
\mathbf{u} = (0,0,0), & \frac{\partial p(x,y,z)}{\partial \mathbf{n}} = 0 & \text{on } \Omega_w \\
\mathbf{u}(x,y,z) \cdot \mathbf{n} = 0, & \frac{\partial p(x,y,z)}{\partial \mathbf{n}} = 0 & \text{on } \Omega_s \\
\frac{\partial \mathbf{u}}{\partial \mathbf{n}} = 0, & p(x,y,z) = 0 & \text{on } \Omega_o\,.
\end{array}
$$

It needs to be noticed that the present problem is substantially different to the numerical exercise carried out in Gómez et al. [180], in which periodic boundary conditions were impose in x and y boundaries and the flow was driven a constant velocity in the far-field with a small domain in the z direction.

Quality of the flow is investigated by the grid convergence study of the flow and the monitoring of the residuals as in the previous validation cases. Table 7.4 presents the GCI index results based on the streamwise velocity downstream of the open cavity at $Re = 100$ for three different resolutions, concluding that a resolution slightly bigger than $\sim 8 \times 10^5$ nodes may be needed to obtain an accurate solution of the flow. However, given the small improvement in convergence from using $\sim 4 \times 10^5$ to $\sim 8 \times 10^5$ nodes, it has been decided to use $\sim 8 \times 10^5$ nodes, which serves well enough the purpose of this study case.

Table 7.4: Grid convergence study based on the velocity downstream of the cavity using three resolutions at $Re = 100$. Grid convergence index obtained with $l = 2^{1/3}$ and $n = 1.89$

Number of nodes	$u(4, 0.25, 0.25)$	$GCI_{j+1,j}(\%)$
$\sim 8 \times 10^5$	0.825988	1.73
$\sim 4 \times 10^5$	0.824306	2.68
$\sim 2 \times 10^5$	0.821706	-

7.2.2 Instability analysis

Figure 7.13 represents a construction of the leading global mode as sum of amplitude functions of the real and imaginary part of the mode at a certain phase as a result of applying the present methodology to the base flow described above.

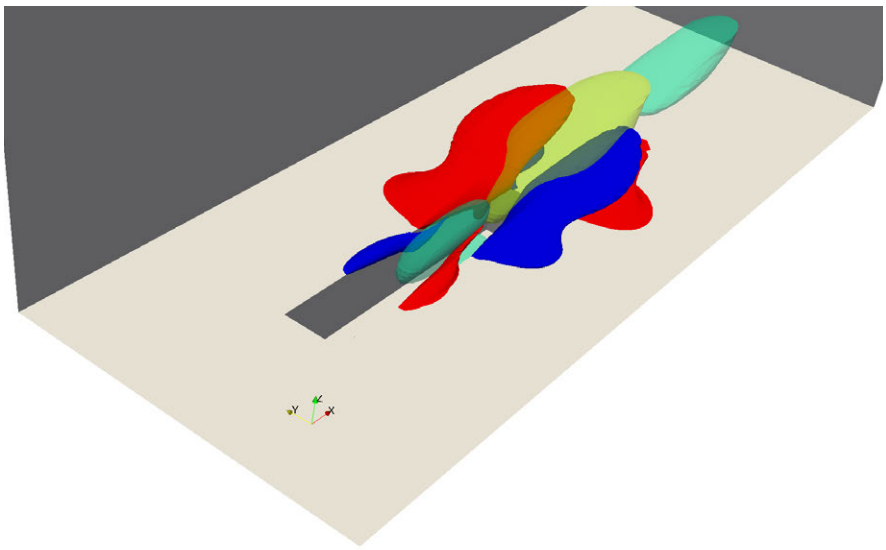

Figure 7.13: Leading global mode of a three-dimensional open cavity. $x-$vorticity component is represented by solid isosurfaces (red-blue), corresponding to $\omega_x = \pm 0.13$ of the maximum vorticity. Translucid isosurfaces (green-yellow) represent the contours satisfying $\hat{u}(x, y, z) = \pm 0.2$ of the maximum of the u eigenvector

This leading eigenmode corresponds to a complex conjugate eigenvalue $\lambda = 0.134 \pm 0.047$. The spatial distribution of the eigenfunction shows a streamwise periodic structure that begins in the cavity and travels dowstream. Although this mode resembles some analogy to the wave-like branch of modes[178, 181] recovered as solution of an BiGlobal eigenvalue problem, as Figure 7.14 shows, the spatial structure of $x-$ vorticity along the sides of the cavity, as seen in Figure 7.13, clearly demonstrates the influence of the three-dimensionality in the span direction on the eigenmode. In addition, the localized origin of the amplitude function of the eigenmode centered in the neighborhood of the cavity, point to the fact that the cavity acts as the origin of linear perturbations, rather than an instability of the downstream boundary layer.

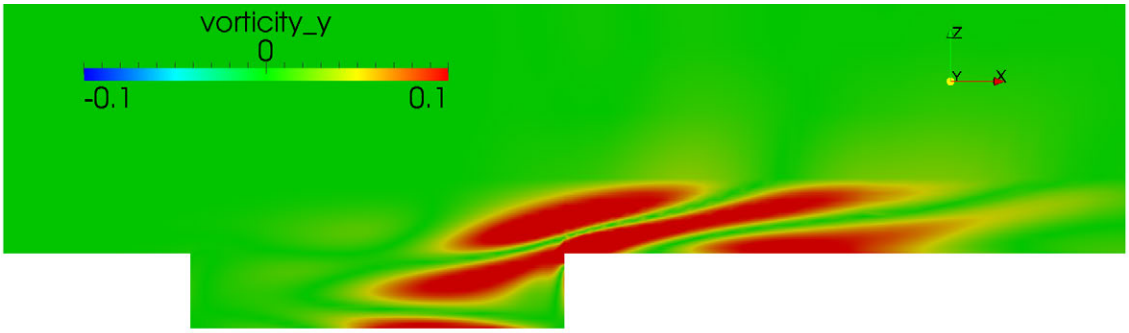

Figure 7.14: $y-$vorticity component in plane $y = 0$ of the leading eigenmode of the open cavity at $Re = 100$

Interesting as it may be in its own right, the present analysis at low Reynolds number and incompressible flow is only a feasibility study as far as the store separation problem is concerned; work to complete the incompressible analysis and to extend it at higher Reynolds numbers in compressible flow remains to be carried out.

Chapter 8

Flow Control Aspects

8.1 Flow control via state space system

Active flow control, via control of linear flow instabilities, can alter the flow state in a desired manner through either attenuation or amplification of intrinsic small-amplitude flow perturbations, at the expense of relatively small amounts of actuator power compared with that necessary to control the nonlinear flow. Ever expanding flow control concepts and improving technologies for the construction of actuators capable of controlling a flow at ever smaller spatial scales [182], combined with continuous progress in the identification and understanding of fluid flow instabilities, increasingly convert flow control from art to science, in which the input-output dynamic behavior is described by an appropriately defined state-space formulation [183]. Success has been reported in the literature over the past two decades, initially focusing on regular geometries in which canonical flows, having one inhomogeneous and either two homogeneous (e.g. plane channel) or one homogeneous and one weakly-developing (e.g. flat-plate boundary layer) spatial direction, were considered [184, 185].

However, most interesting flows develop over or through complex geometries in which all three spatial directions are inhomogeneous, or the flow may be taken to depend in an inhomogeneous manner upon two spatial directions and either be homogeneous or develop weakly along the third spatial direction. Small-amplitude *hydrodynamic and aeroacoustic* perturbations in these classes of flows are unraveled by global linear theory [1]. In the last decade flow control via control of global flow instabilities has also been reported [186], expedited by Galerkin projection of the full system onto an appropriately defined low-dimensional basis, a Reduced Order Model (ROM) designed to describe the system dynamics [167, 187]. The key advantage of building theoretical flow control around a ROM is the drastic reduction it offers in the number of degrees of freedom of the discretized linear state-space formulation which describes feedback control of the flow in question; in this manner, controllers of manageable size may be constructed. An obvious drawback of embedding a ROM in the overall control algorithm is the *a-priori* unknown performance (or even validity) of the proposed ROM when flow conditions are changed.

The linear state space system describing input-output small-amplitude perturbation dynamics can be written as

$$\dot{\hat{\mathbf{q}}} = \mathbf{A}\hat{\mathbf{q}} + \mathbf{B}\mathbf{u}, \tag{8.1}$$

$$\mathbf{y} = \mathbf{C}\hat{\mathbf{q}} + \mathbf{D}\mathbf{u}, \tag{8.2}$$

where $\hat{\mathbf{q}} \in \mathbb{R}^n$ is the vector of linear flow perturbations, $\mathbf{A} \in \mathbb{R}^{n \times n}$ is the operator describing spatial discretization of the linearized Navier-Stokes equations (LNSE), linearization being performed around the base state $\bar{\mathbf{q}}$ which is to be controlled, $\mathbf{u} \in \mathbb{R}^m$ and $\mathbf{y} \in \mathbb{R}^r$ are the vectors of inputs and outputs, respectively, while the input matrix $\mathbf{B} \in \mathbb{R}^{n \times m}$ describes the actuators, and the output matrix $\mathbf{C} \in \mathbb{R}^{r \times n}$ describes the sensors. The feed-through matrix $\mathbf{D} \in \mathbb{R}^{r \times m}$ is taken to be non-zero when $\mathbf{u}$ directly affects $\mathbf{y}$, otherwise it is neglected. The usual assumption $m, r \ll n$ implies that the dimension of the discretized system (8.1-8.2) is dominated by n, the number of degrees of freedom which discretize the LNSE. In turn, n is determined by whether the flow to be controlled is incompressible or compressible and also whether it is developing in a domain with one, two or three inhomogeneous spatial directions.

A Laplace transformation of the system (8.1-8.2) leads to the definition of the transfer function, $\mathbf{G}(s) \in \mathbb{C}^{r \times m}$, through which the frequency response matrix, $\mathbf{G}(\mathrm{i}\omega)$, may also be defined,

$$\mathbf{G}(s) = \mathbf{C}(s\mathbf{I} - \mathbf{A})^{-1}\mathbf{B} + \mathbf{D}, \qquad \mathbf{G}(\mathrm{i}\omega) = \mathbf{C}(\mathrm{i}\omega\mathbf{I} - \mathbf{A})^{-1}\mathbf{B} + \mathbf{D}, \tag{8.3}$$

with s the Laplace-transformed time-coordinate, ω a real frequency and $\mathrm{i} = \sqrt{-1}$. From a purely formal point of view, computation of the frequency response matrix and recovery of a window of the global flow eigenspectrum after a complex shift [1], share the common need to calculate the inverse of matrix $(\mu\mathbf{I} - \mathbf{A}), \mu \in \mathbb{C}$, which is circumvented in practice by calculating its LU decomposition. On the other hand, (8.1-8.2) could be solved in a time-stepping context as:

$$\hat{\mathbf{q}} = e^{\mathbf{A}\tau}\hat{\mathbf{q}}_{\mathbf{0}} + \int_{\tau}^{0} \mathbf{B}\mathbf{u}\mathrm{d}t \tag{8.4}$$

with the matrix-free methodologies developed in this thesis.

Accuracy in the numerical solutions of (8.1-8.2) and the computation of (8.3) or (8.4) via matrix-forming or matrix-free strategies is of paramount significance, if reliable flow control results are to be obtained. However, the large size of the discretized matrices describing the feedback control problem can hardly be managed in all but canonical base flows with one inhomogeneous spatial direction, thus a ROM of the flow dynamics must be invariably constructed prior to applying flow control [188].

8.2 Flow control via adjoint operator

A further discussion of the adjoint eigenvalue problem is introduced in what follows. A comparison of the spatial distribution of the amplitude functions of direct and adjoint eigenfunctions reveals that areas of overlap between them exist, or not. In the first case, the relevant theoretical background to flow control introduced in the celebrated work of Hill [189], who demonstrated that the spatial locations of overlapping direct and adjoint eigenfunctions indicate positions of maximal sensitivity of a given eigenmode to changes in base flow or boundary conditions. In the same work, results in excellent agreement with experiment [190] were produced, regarding the correlation of the location where a second, small-diameter control cylinder was placed, and the ensuing stabilization of the wake of circular cylinder. Giannetti and Luchini [168] introduced the associated concept of structural sensitivity of the eigenvalues delivered by (2.4) and paved the way for the application of the analysis to a variety of flows in two inhomogeneous spatial directions. No work is known to the author dealing with application of this concept in conjunction with TriGlobal linear instability. On the

other hand, as discussed by Chomaz [191], the case of no spatial overlap between direct and adjoint eigenfunctions is indicative of convective non-normality and the associated potential of the flow to exhibit large transient growth, as demonstrated, e.g. by Blackburn et al. [55] and Nichols & Lele [48] in incompressible and compressible flow, respectively. Finally, the utility of the adjoint EVP solution has long been established in the context of studies of receptivity of flat plate boundary layer flow [192, 193], but it is still at its infancy as far as global linear instability theory is concerned, in either a BiGlobal or a TriGlobal context.

Structural sensitivity of the eigenmodes to modifications of the base flow can be calculated with the construction of an bi-orthogonal or adjoint operator[189, 168] $\mathbf{A}^*$, being their eigenfunctions $\hat{\mathbf{v}}$ left eigenvectors of the Jacobian matrix. Following notation of equation (2.34) this reads:

$$\hat{\mathbf{v}}(\mathbf{A} - \lambda\mathbf{I}) = 0\,. \tag{8.5}$$

or equivalently,

$$(\mathbf{A}^* - \lambda\mathbf{I})\hat{\mathbf{v}} = 0\,. \tag{8.6}$$

By perturbing the direct eigenvalue problem (8.6) it is obtained that:

$$\delta(\mathbf{A} - \lambda\mathbf{I})\hat{\mathbf{u}} = (\delta\mathbf{A} - \delta\lambda\mathbf{I})\hat{\mathbf{u}} + (\mathbf{A} - \lambda\mathbf{I})\delta\hat{\mathbf{u}}\,, \tag{8.7}$$

and using the adjoint relation (8.6) leads to a relation between the change induced in the eigenvalue $\delta\lambda$ by the modification of the Jacobian-matrix,

$$\delta\lambda = \frac{\hat{\mathbf{v}}\delta\mathbf{A}\hat{\mathbf{u}}}{\hat{\mathbf{v}}\cdot\hat{\mathbf{u}}}\,. \tag{8.8}$$

If a localized in space perturbation as $\delta\mathbf{A} = \delta(x - x_o, y - y_o, z - z_o)$ is introduced in the the above equation, it is possible to define a function that localizes the spatial positions where the direct eigenfunctions $\mathbf{u}_\mathbf{i}'$ are most sensible to perturbations of the Jacobian-matrix through small changes in the base flow, enabling the possibility of suppressing instability onsets by small modifications in the base flow, as done experimentally by Strykowski & Sreenivasan [190]. This reads:

$$\delta\lambda(x, y) = \frac{|\hat{\mathbf{v}}|\,|\hat{\mathbf{u}}|}{\hat{\mathbf{v}}\cdot\hat{\mathbf{u}}}\,. \tag{8.9}$$

As oppose to the modal linear instability analysis, the effect of the adjoint operator cannot be obtained by means of the use of general purpose aerodynamic codes without modification (and availability) of the source-code. Therefore, a linearization of the Navier–Stokes is required for the solution of TriGlobal adjoint problems.

The derivation of the adjoint operator can be found in multiple classical textbooks, e. g. Golub & Van Loan [194] or Morse & Feshback [49], where the most critical step is deriving proper boundary conditions for the vanishing of the bilinear concomitant. In what follows, the derivation will be omitted for simplicity and the adjoint equations will be presented with correct boundary conditions that satisfies a zero bilinear concomitant. This section will be focused on the extraction of the adjoint eigenmodes in a time-stepping matrix-free context, as performed by Barkley et al. [16]. Further details about the construction of the adjoint operator and its use to determine the structural sensitivity of the eigenmodes can be found in the works of Hill[189] or Giannetti & Luchini[168].

As a first step, the modification of the *icoFoam* solver has been carried out in order to solve direct and adjoint NS equations. Appendix A summarizes the development of a linearized and adjoint Navier–Stokes equation solver using the same PISO algorithm thoroughly employed in this thesis, named *dirIcoFoam* and *adjIcoFoam* respectively. In a similar fashion to the LNSE (2.32), the adjoint equations can be written in a compact form as:

$$\frac{\partial \mathbf{v}'}{\partial t} = \mathbf{A}^* \mathbf{v}' \,, \tag{8.10}$$

which permits the instability analysis in a time-stepping context using the exponential of the adjoint operator as it has been carried out with the exponential transformation (4.7) in Chapter 4. The instability analysis algorithm is analogous to the algorithm 4.4 using LNSE with the particularity that the effect of the adjoint operator is computed backwards in time because the negative sign in the temporal term in Equation (9). The numerical method to extract the adjoint modes is detailed in Algorithm 8.2.

Algorithm 5 Instability analysis with adjoint exponential operator

S1. Initial Condition: Set m, $\mathbf{v}'_1$

S2. Power iteration: Perform until convergence $(l = 1, ..., m)$,

- **A1. Call *adjIcoFoam*:** $\mathbf{v}'_l \leftarrow e^{-\mathbf{A}*\tau}\mathbf{v}'_l$
- **A2. Gram-Schmidt:** $(i = 1, ..., l)$
  - **GS1.** Form Hessenberg matrix $h_{il} = \mathbf{v'}_i^T e^{-\mathbf{A}^*\tau}\mathbf{v}'_l$
  - **GS2.** Orthogonalize $\mathbf{v}'_{l+1} = e^{-\mathbf{A}^*\tau}\mathbf{u}'_l - \sum_{i=1}^{j} h_{il}\mathbf{u}'_i$
  - **GS3.** Normalize $h_{l+1,l} = \|\mathbf{v}'_{l+1}\|$, $\mathbf{v}'_{l+1} = \frac{\mathbf{v}'_{l+1}}{h_{l+1,l}}$

S3. QR: Perform eigenvalue decomposition of the $m \times m$ matrix $\mathbf{H}$

S4. Undo exponential transformation

In the case that the interest only lies on the leading global mode that first bifurcates the flow and not on the rest of modes, an easier method, a power iteration, can be carried out in order to extract the direct and adjoint leading modes. Algorithm 8.2 shows the basic numerical method based on power iteration, where an additional damping term that produces an eigenvalue shift λ_s is introduced in the right hand of the equations (8) and (8.10) in order to attenuate or mitigate the damping/growth ratio of the leading mode. In addition, this shift eliminate the need of normalization at each step, since the leading eigenvalue preserves its initial magnitude and the others eigenvalues are damped while the temporal integration.

Since this is equivalent to the temporal integration it converges as $\sim |\lambda_1 - \lambda_2|\,\tau$, thus this algorithm is very effective when a gap between first and second eigenvalue is expected in the spectrum. Further modifications based on the update of the eigenvalue shift λ_s at each step by making use of the direct adjoint relationship (8.8), as envisaged by Giannetti & Luchini in a shift-invert matrix-forming framework, can be easily introduced in the algorithm [168].

Algorithm 6 Instability analysis with direct and adjoint power iteration

S1. Initial Condition: Set m, $\mathbf{u}'_1$, $\mathbf{v}'_1$, λ_s

S2. Power iteration: Perform until convergence ($l = 1, ..., m$),

A1. Call *dirIcoFoam*: $\mathbf{u}'_l \leftarrow e^{(\mathbf{A}-\lambda_\mathbf{s}\tau)}\mathbf{u}'_l$

A2. Call *adjIcoFoam*: $\mathbf{v}'_l \leftarrow e^{(-\mathbf{A}*+\lambda_\mathbf{s}\tau)}\mathbf{v}'_l$

A3. Eigenvalue computation: $e^{\lambda_l-\lambda_s} = \mathbf{u}'^T_l e^{(\mathbf{A}-\lambda_\mathbf{s}\tau)}\mathbf{u}'_l$

S3. After convergence $\mathbf{u}'_m = \hat{\mathbf{u}}_\mathbf{1}$, $\mathbf{v}'_m = \hat{\mathbf{v}}_\mathbf{1}$, $\lambda_m = \lambda_1$

8.3 Sensitivity of the flow past a circular cylinder

The well-known example of the cylinder wake flow has served as validation of this chapter. A similar mesh to the one employed in Chapter 7 for the straked cylinder validation has been used for the generation of a base flow at $Re = 40$. Direct and adjoint modes has been computed by using the algorithms 4.4 and 8.2 using the *dirIcoFoam* and *adjIcoFoam* solver respectively.

In case of the LNSE, the boundary conditions are derived straight forward from the linearization of the ones used for the base flow, which are zero inflow, no-slip at the cylinder surface and outflow at the rear part. This reads:

$$\begin{array}{rl} \mathbf{u}'(x,y,z) = (0,0,0), & \frac{\partial p'(x,y,z)}{\partial \mathbf{n}} = 0 \quad \text{on } \Omega_i \\ \mathbf{u}'(x,y,z) = (0,0,0), & \frac{\partial p'(x,y,z)}{\partial \mathbf{n}} = 0 \quad \text{on } \Omega_w \\ \frac{\partial \mathbf{u}'}{\partial \mathbf{n}} = 0, & p'(x,y,z) = 0 \quad \text{on } \Omega_o\,. \end{array}$$

Regarding the adjoint equations, the most suitable boundary conditions are:

$$\begin{array}{rl} \mathbf{v}'(x,y,z) = (0,0,0), & \frac{\partial m'(x,y,z)}{\partial \mathbf{n}} = 0 \quad \text{on } \Omega_i \\ \mathbf{v}'(x,y,z) = (0,0,0), & \frac{\partial m'(x,y,z)}{\partial \mathbf{n}} = 0 \quad \text{on } \Omega_w \\ \mathbf{v}'(x,y,z) = (0,0,0), & m'(x,y,z) = 0 \quad \text{on } \Omega_o\,. \end{array}$$

The derivation of these boundary conditions are not trivial and the reader is referred to the works of Barkley et al. [16] or Giannetti & and Luchini [168]. Furthermore, the given outflow boundary condition is not formally correct. However, it can be imposed in the computational domain is large enough for the adjoint mode to be vanished at the far-field.

Figure 8.1 shows the spatial distribution of the velocity field modulus of the cylinder wake leading mode at $Re = 40$ corresponding to an eigenvalue $\lambda_1 = -0.030 \pm i \cdot 0.126$ in excellent agreement with the results from the literature shown in Figure 7.7 [172, 168] . It can be seen that the maximum of the eigenvector lies inside the computational domain, proving that the employed domain is large enough for the present calculations.

The corresponding modulus of the adjoint leading mode and the spatial distribution of the product between the direct and adjoint eigenfunctions $\delta\lambda(x, y)$ are shown in Figure 8.2. These figures are in perfect agreement with those available in the literature and indicate that the instability mechanism is located in two lobes placed symmetrically inside the separation bubble.

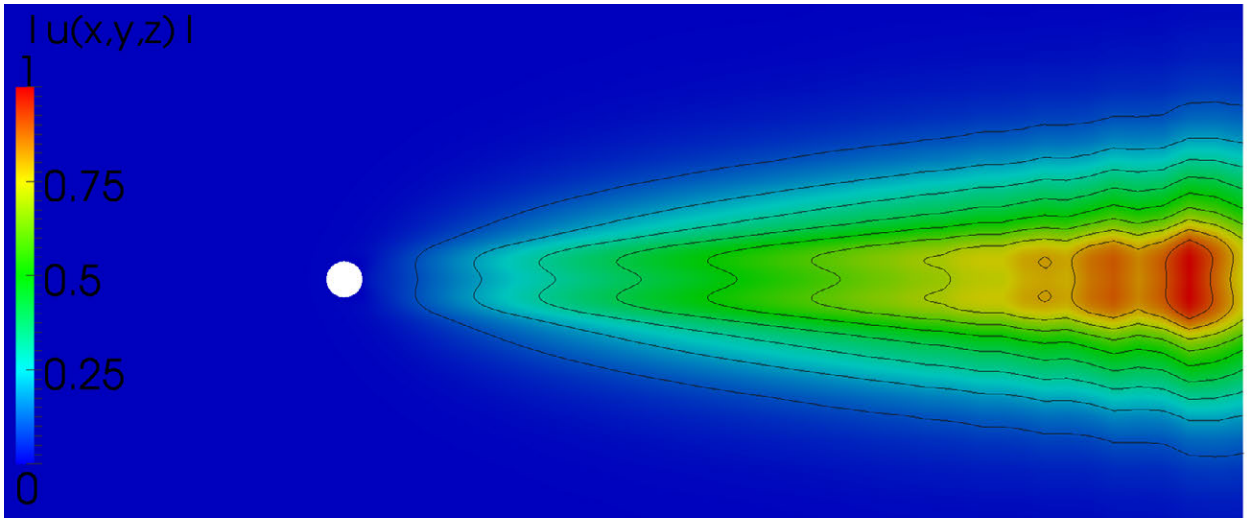

Figure 8.1: $|\hat{\mathbf{u_1}}|$ normalized module of the leading eigenvector of the cylinder wake at $Re = 40$

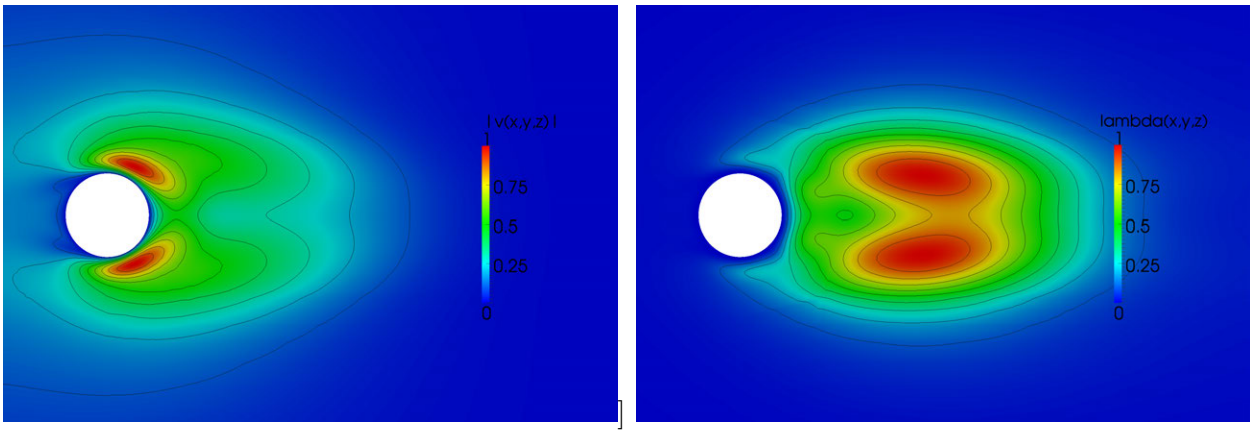

Figure 8.2: (*left*)$|\hat{\mathbf{v_1}}|$ normalized module of the adjoint leading eigenvector of the cylinder wake. (*right*) Contour plot of the function $\delta\lambda(x, y)$ at $Re = 40$

8.4 Sensitivity of the flow inside a three-dimensional lid-driven cavity

The direct-adjoint instability analysis has been applied to the wall-bounded three-dimensional lid-driven cavity studied in Chapter 6, which correspond to a TriGlobal EVP, as a final example of the capability of the present methodology. The employed mesh and base flow is the one corresponding to $Re = 1000$, which spectrum is shown in Figure 6.4. The sensitivity of the leading eigenvalue of that spectrum, corresponding to $\lambda_1 = -0.1292 \pm i0.329$, will be analyzed. Since this leading eigenvector is already known from the previous analysis, only the leading adjoint modes need to be computed by using the algorithm with the *adjIcoFoam* solver. Dirichlet and Neumann boundary conditions are imposed for the adjoint velocity and adjoint pressure respectively in all boundaries. Figure 8.3

shows the normalized spatial distribution of the velocity field modulus of the cylinder wake direct and adjoint leading eigenfunction, in which some similarity can be inferred, thus anticipating spatial overlapping of both functions.

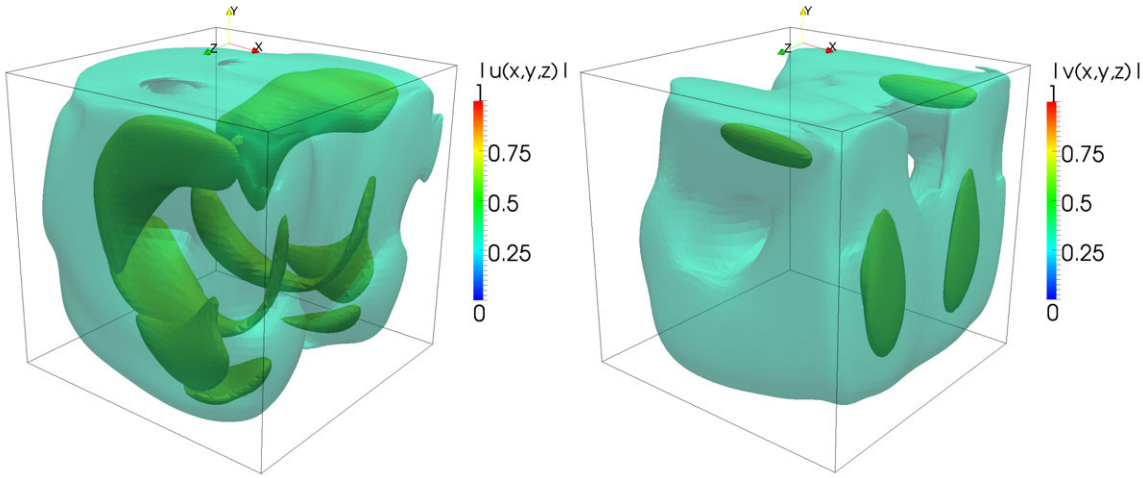

Figure 8.3: Normalized module of the (*top*) $|\hat{\mathbf{u_1}}|$ direct eigenmode (*bottom*) $|\hat{\mathbf{v_1}}|$ adjoint eigenmode at $Re = 1000$. Translucid isosurfaces represent a normalized value of 0.3 and solid isosurfaces indicate a value of 0.7

The spatial distribution of the product between these direct and adjoint eigenfunctions $\delta\lambda(x, y, z)$ is shown in Figure 8.4. The large overlapping of the direct and adjoint eigenfunctions indicates that the Jacobian-matrix of this flow presents small non-normality. This results is well-known in the literature since the wall-bounded flows do not exhibit large transient growth [191]. However, the areas of maximum sensitivity of the eigenvalue are located in two lobes symmetrically located close to the upper side corners, indicating the influence of the end-wall effects on the three-dimensional global mode. Flow control based on this feature could be exploited in a future work.

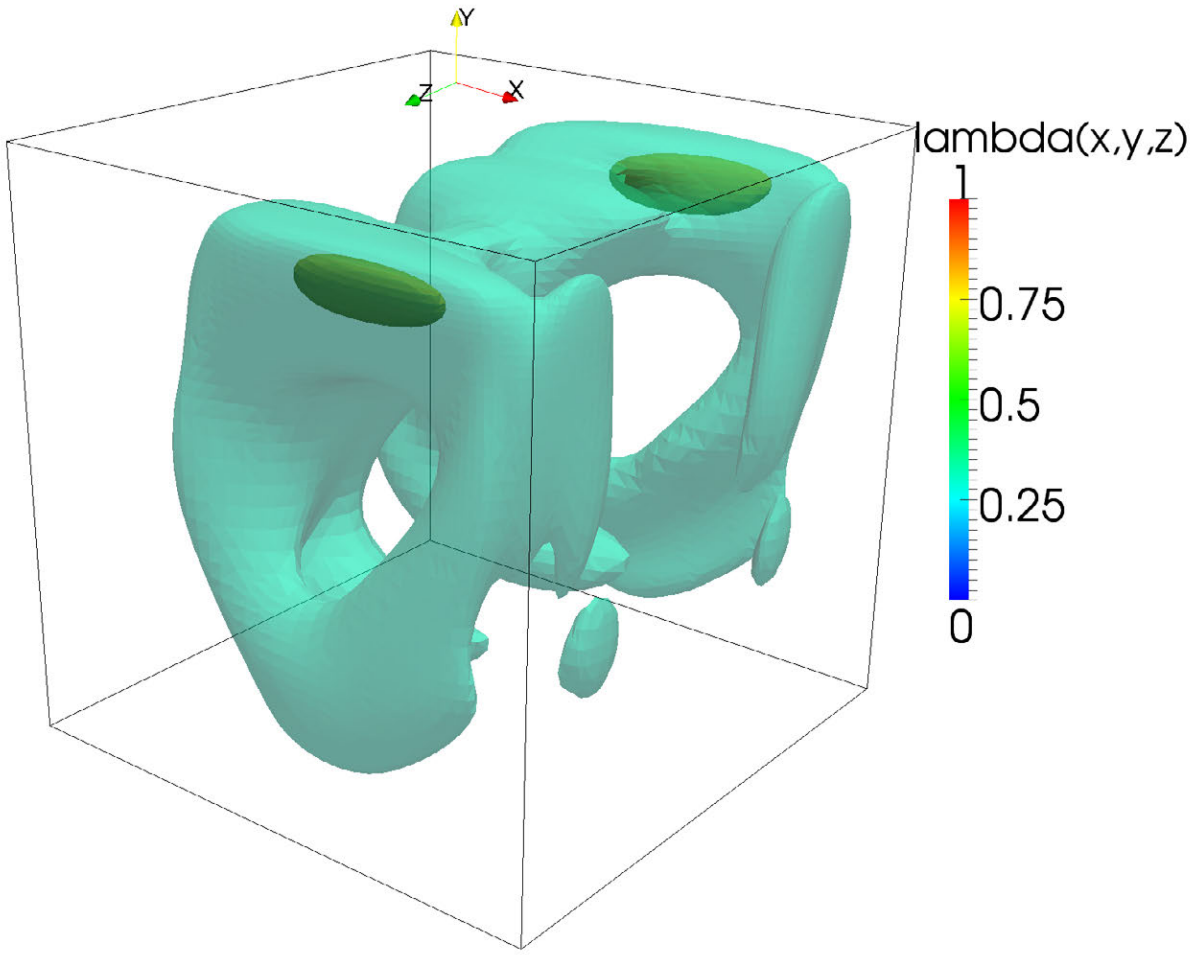

Figure 8.4: Contour plot of the function $\delta\lambda(x, y, z)$ of the cubic LDC at $Re = 1000$. Translucid isosurfaces represent a normalized value of 0.3 and solid isosurfaces indicate a value of 0.7

Chapter 9

Conclusions

The development of a general approach for the solution of the TriGlobal linear instability analysis eigenvalue problem has been successfully developed, by coupling different codes with a matrix-free time-stepping methodology, including the algorithmic innovations necessary in order to perform such analysis. The ability to directly use software utilities available within the employed CFD solvers, such as parallelization, pre- or post-processing has been exploited. This feature provides a large versatility to the methodology.

It has been found that the reliability of the present analysis strongly depends on the parameter of the numerical method and concise guidelines have been provided for the adequate selection of the parameters of the proposed algorithm. In addition, the time-stepping methodology has been extended with shift-invert strategies in order to provide access to any subset of the spectrum at the cost of additional computational resources.

The methodology has been successfully validated against the available results in the literature for cubic lid-driven cavities and it has been further demonstrated to be capable of providing for the first time eigenvalues and eigenfunctions of the flow inside three-dimensional, wall-bounded lid-driven cavity flows of aspect ratio different to unity. Results were found in qualitative agreement with those available in the literature in a DNS or experimental context. Moreover, it has been shown that linear eigenmodes presenting symmetric and asymmetric n-cell TGL patterns exist in stable flows, linking these well-known structures with linear global flow eigenmodes.

The present global instability methodology has been also successfully applied to challenging three-dimensional open flows: the flow past a cylinder fitted with helical strakes and the flow over an inhomogeneous open cavity. Global instability analysis of these flows has provided for first time insight on the three-dimensional structure of their corresponding leading modes.

Furthermore, it has been shown that the methodology can be modified in order to perform adjoint instability analysis of three-dimensional base flows and, ultimately, flow control.

It can be concluded that the proposed algorithm enables TriGlobal linear modal instability analysis of flows in complex geometries on modest contemporary hardware and is a viable alternative to existing methods for the instability analysis of laminar flows in three-dimensional geometries, leaving the analysis of turbulent flows in such geometries as a future challenge.

Appendix A: Direct and adjoint LNSE using the PISO algorithm

The PISO (Pressure Implicit with Splitting of Operators) algorithm employed by the *icoFoam* solver and its modifications to solver linearized and adjoint NS equations are explained here in detail. The key idea of the PISO algorithm[89, 90, 91] is that for small time-steps the pressure-velocity coupling is much stronger than the non-linear convective coupling, therefore it is possible to split the solution into a set of corrections where the pressure is decoupled from the velocity, since the velocity in the momentum equation does not need to be updated for each pressure correction.

As an example of the notation that will be employed in what follows, the semi-discretization of the convective term of the Navier–Stokes using finite volumes is written as:

$$\int_V \nabla \cdot (\mathbf{u}u) dV = \int_S u\mathbf{u} \cdot \hat{n} dS = \sum_i \mathbf{u}^i \cdot S^i u^i = \sum_i \phi^i u^i = a_P u_P + \sum_N a_N u_N \tag{1}$$

where the velocity is evaluated on the faces i of the cell P with volume V and surface S, and subscript N refers to neighbors cells and interpolation is required for the volume fluxes. Taking this formulation into account, the momentum equation of the Navier–Stokes equation can be written as:

$$\mathbf{a_P u} = \mathbf{H}(\mathbf{u}) - \nabla p_n \,, \tag{2}$$

or equivalently

$$\mathbf{u} = \mathbf{a_P}^{-1}\mathbf{H}(\mathbf{u}) - \mathbf{a_P}^{-1}\nabla p_n \,, \tag{3}$$

where $\mathbf{a_P}$ represents the discretization matrix operator of the implicit terms while $\mathbf{H}$ represents the explicit terms of the velocity. The first two terms of the above equations are written in OpenFOAM® notation as:

```
fvVectorMatrix UEqn (fvm::ddt(U)+ fvm::div(phi, U) - fvm::laplacian(nu, U));
```

where *fvm* denotes implicit construction of the operator. A momentum predictor is then obtained using the momentum equation and the pressure from a previous step, which in OpenFOAM® notation leads to:

```
solve(UEqn == -fvc::grad(p));
```

Recalling equation (3), the explicit terms can be written as

$$U^* = a^{-1}H\,, \tag{4}$$

which in OpenFOAM® notation is written as:

```
volScalarField rUA = 1.0/UEqn.A(); U* = rUA*UEqn.H();
```

where the functions $UEqn.A()$ and $UEqn.H()$ extract the implicit and explicit terms from equation (3). The momentum equation is then written as:

$$U = U^* - a^{-1}\nabla p\,, \tag{5}$$

where the left hand side term is divergence-free and the continuity equation can be applied to obtain the laplacian equation:

$$\nabla \cdot U^* = \nabla \cdot a^{-1}\nabla p\,, \tag{6}$$

in which the left hand side can be treated explicitly. Using finite volumes formulation and updating the velocity flux ϕ with the new velocity the new pressure field is obtained. In OpenFOAM® notation this follows:

```
phi = (fvc::interpolate(U*) & mesh.Sf());
fvScalarMatrix pEqn (fvm::laplacian(rUA, p) == fvc::div(phi));
```

Finally the divergence-free velocity U is corrected with the correct pressure gradient with Equation (3). This PISO algorithm is summarized in Algorithm 9. Non-orthogonal, boundary conditions corrections and details about the discretization has been omitted for simplicity.

Algorithm 7 PISO algorithm

S1: Set initial conditions

S2: Time-step iteration ($t = 0, ..., t_f$)

- **S2:** Obtain momentum predictor by solving momentum equation using mass flux ϕ from previous velocity and pressure $a_P\mathbf{u}^* = H - \nabla p_{n-1}$
- **S3:** PISO Iteration ($i = 1, ..., N_{PISO}$)
  - **P2:** Compute volume fluxes
  - **P4:** Solve the pressure equation
  - **P5:** Correct the velocity with new pressure field
  - **P6:** Update boundary conditions.
- **S4:** Advance time-step

This PISO algorithm can be easily modified in order to solve the direct and adjoint linearized NS equations. The LNSE equations (2.32) can be written in detail as

$$\nabla \cdot \mathbf{u}' = 0 \tag{7}$$

$$\frac{\partial \mathbf{u}'}{\partial t} + \bar{\mathbf{u}} \cdot \nabla \mathbf{u}' + \mathbf{u}' \cdot \nabla \bar{\mathbf{u}} = -\nabla p' + \frac{1}{Re} \nabla^2 \mathbf{u}' . \tag{8}$$

while the corresponding adjoint equations follow that

$$\nabla \cdot \mathbf{v}' = 0 \tag{9}$$

$$-\frac{\partial \mathbf{v}'}{\partial t} + \bar{\mathbf{u}} \cdot \nabla \mathbf{v}' - \mathbf{v}' \cdot \nabla \bar{\mathbf{u}} = -\nabla m' + \frac{1}{Re} \nabla^2 \mathbf{v}' . \tag{10}$$

It is trivial to observe that the main difference with the full NS equations are the additional advection terms and the different signs in case of the adjoint equations. Since the terms related with the base flow are constant, and the predictor fluxes of the perturbation are constructed with the perturbation velocity from previous step, the second advection term of direct and adjoint equations can be formed in a explicit manner, thus the equations to be solved are equivalent to the non-linear case. In other words, the base flow advection term can be treated as a source term .

Therefore, the *dirIcoFoam* and *adjIcoFoam* solvers for the solution of the temporal evolution of the linearized direct and adjoint Navier–Stokes equations (8) and (9) can be constructed by modifying the matrix *UEqn* including the new advection terms without further modifications. For the LNSE solver *dirIcoFoam* this reads:

```
fvVectorMatrix UEqn
   (
       fvm::ddt(U)
     + fvm::div(phiB, U)
     + fvc::div(phi, UB)
     - fvm::laplacian(nu, U)
   );
```

where *U* refers now to the perturbation, *UB* to the base flow and *fvc* means explicit construction. Finally, the adjoint equation solver *dirIcoFoam* is written as:

```
fvVectorMatrix VEqn
(
  -  fvm::ddt(V)
  + (fvc::grad(UB) & V)
  - fvm::div(phiB, V)
  - fvm::laplacian(nu, V)
);
```

where *V* refers to the adjoint perturbation and special treatment of the temporal scheme is required for the backwards temporal integration.

Bibliography

[1] Theofilis, V., "Global Linear Instability," *Annual Review of Fluid Mechanics*, Vol. 43, 2011, pp. 319–352.

[2] Saad, Y., "Variations of Arnoldi's method for computing eigenelements of large unsymmetric matrices." *Linear Algebra Appl.*, Vol. 34, 1980, pp. 269–95.

[3] Arnoldi, W., "The principle of minimized iterations in the solution of the matrix eigenvalue problem," *Quart. Appl. Math.*, Vol. 9, 1951, pp. 17–29.

[4] Natarajan, R. and Acrivos, A., "The instability of the steady flow past spheres and disks," *Journal of Fluid Mechanics*, Vol. 254, 1993, pp. 323–344.

[5] Eriksson, L. and Rizzi, A., "Computer-aided analysis of the convergence to steady state of discrete approximations to the Euler equations," *J. Comput. Phys*, Vol. 57, 1985, pp. 90–128.

[6] Gomez, F., Le Clainche, S., Paredes, P., Hermanns, M., and Theofilis, V., "Four Decades of Studying Global Linear Instability: Progress and Challenges," *AIAA Journal*, Vol. 50, No. 12, 2012, pp. 2731–2743.

[7] Perez, J., Rodriguez, D., and Theofilis, V., "Linear global instability of non-orthogonal incompressible swept attachment-line boundary-layer flow," *Journal of Fluid Mechanics*, Vol. 710, 2012, pp. 131–153.

[8] Bres, G. A. and Colonius, T., "Three-dimensional instabilities in compressible flow over open cavities," *Journal of Fluid Mechanics*, Vol. 599, 2008, pp. 309–339.

[9] Hussain, F. and Reynolds, W. C., "The mechanics of an organized wave in turbulent shear flow," *J. Fluid Mech.*, Vol. 41, 1970, pp. 241–258.

[10] Crouch, J. D., Garbaruk, A., and Magidov, D., "Predicting the onset of flow unsteadiness based on global instability," *Journal of Computational Physics*, Vol. 224, No. 2, June 2007, pp. 924–940.

[11] Crouch, J. D., Garbaruk, a., Magidov, D., and Travin, a., "Origin of transonic buffet on aerofoils," *Journal of Fluid Mechanics*, Vol. 628, June 2009, pp. 357.

[12] Biau, D., Soueid, H., and Bottaro, A., "Transition to turbulence in duct flow," *Journal of Fluid Mechanics*, Vol. 596, Jan. 2008, pp. 133–142.

[13] Nichols, J. W. and Lele, S. K., "Global modes and transient response of a cold supersonic jet," Vol. 669, 2011, pp. 225–241.

[14] Rodriguez, D. and Theofilis, V., "Massively Parallel Solution of the BiGlobal Eigenvalue Problem Using Dense Linear Algebra," *AIAA Journal*, Vol. 47, 2009, pp. 2449–2459.

[15] Paredes, P., Hermanns, M., Le Clainche, S., and Theofilis, V., "Order 10^4 speedup in global linear instability analysis using matrix formation," *Computer Methods in Applied Mechanics and Engineering*, Vol. 253, 2013, pp. 287–304.

[16] Barkley, D., Blackburn, H. M., and Sherwin, S. J., "Direct optimal growth analysis for timesteppers," *International journal for numerical methods in fluids*, Vol. 57, No. 9, 2008, pp. 1435–1458.

[17] Chiba, S., "Global stability analysis of incompressible viscous flow," *J. Jpn. Soc. Comput. Fluid Dyn.*, Vol. 7, 1998, pp. 20–48.

[18] Tezuka, A., "Global Stability Analysis of Attached or Separated Flows over a NACA0012 Airfoil," *AIAA Paper*, No. 2006-1300, 2006.

[19] Tezuka, A. and Suzuki, K., "Three-Dimensional Global Linear Stability Analysis of Flow Around a Spheroid," *AIAA Journal*, Vol. 44, No. 8, Aug. 2006, pp. 1697–1708.

[20] Edwards, W., Tuckerman, L., Friesner, R., and Sorensen, D., "Krylov Methods for the Incompressible Navier-Stokes Equations," *Journal of Computational Physics*, Vol. 110, No. 1, Jan. 1994, pp. 82–102.

[21] Barkley, D. and Henderson, R. D., "Three-dimensional Floquet stability analysis of the wake of a circular cylinder," *Journal of Fluid Mechanics*, Vol. 322, No. -1, April 1996, pp. 215.

[22] Tuckerman, L. and Barkley, D., "Bifurcation analysis for timesteppers," *Numerical Methods for Bifurcation Problems and Large-Scale Dynamical Systems*, edited by E. Doedel and L. Tuckerman, Springer Berlin, 2000, pp. 453–566.

[23] Bagheri, S., Åkervik, E., Brandt, L., and Henningson, D. S., "Matrix-free methods for the stability and control of boundary-layer flows," *AIAA J.*, Vol. 47, 2009, pp. 1057 – 1068.

[24] Mack, C. J. and Schmid, P. J., "A preconditioned Krylov technique for global hydrodynamic stability analysis of large-scale compressible flows," *Journal of Computational Physics*, Vol. 229, No. 3, Feb. 2010, pp. 541–560.

[25] Pérez, J., Gómez, F., Gómez, R., and Theofilis, V., "A shift-invert strategy for global flow instability analysis using matrix-free methods," 42^{nd} Fluid Dynamics Conference and Exhibit, New orleans, LA, June 25-28, 2012, AIAA Paper 2012-3276, 2012.

[26] Bagheri, S., Schlatter, P., Schmid, P. J., and Henningson, D. S., "Global stability of a jet in crossflow," *Journal of Fluid Mechanics*, Vol. 624, March 2009, pp. 33–44.

[27] Noack, B., Morzynski, M., and Tadmor, G., *Reduced-order modelling for flow control*, SpringerWienNewYork, 2011.

[28] Giannetti, F., Luchini, P., and Marino, L., "Linear stability analysis of three-dimensional lid-driven cavity flow. Atti del XIX Congresso AIMETA di Meccanica Teorica e Applicata," (Aras Edizioni, Ancona, Italy), Ancona 14-17 Sep. 2009, 2009, pp. 738.1–10.

[29] Liberzon, A., Feldman, Y., and Gelfgat, A. Y., "Experimental observation of the steady-oscillatory transition in a cubic lid-driven cavity," *Physics of Fluids*, Vol. 23, 2011, pp. 23–32.

[30] Feldman, Y. and Gelfgat, A. Y., "Oscillatory instability of a three-dimensiona lid-driven flow in a cube," *Physics of Fluids*, Vol. 22, 2010.

[31] Gómez, F., Paredes, P., Gómez, R., and Theofilis, V., "Global stability of cubic and large aspect ratio three-dimensional lid-driven cavities," 42$^{\text{nd}}$ Fluid Dynamics Conference and Exhibit, New orleans, LA, June 25-28, 2012, AIAA Paper 2012-3274, 2012.

[32] Dijkstra, H. A., Molemaker, M. J., van der Ploeg, A., and Botta, E. F. F., "An efficient code to compute non-parallel flow steady flows and their linear stability," *Comput. Fluids*, Vol. 24, No. 4, 1995, pp. 415 – 434.

[33] Morzyńksi, M. and Thiele, F., "Numerical stability analysis of flow about a cylinder," *Z. Angew. Math. Mech.*, Vol. 71, 1991, pp. T424–T428.

[34] Jackson, C. P., "A finite-element study of the onset of vortex shedding in flow past variously shaped bodies," *Journal of Fluid Mechanics*, , No. 182, 1987, pp. 23–45.

[35] Albensoeder, S., Kuhlmann, H. C., and Rath, H. J., "Three-dimensional centrifugal-flow instabilities in the lid-driven-cavity problem," *Physics of Fluids*, Vol. 13, No. 1, 2001, pp. 121–136.

[36] Albensoeder, S., Kuhlmann, H. C., and Rath, H. J., "Multiplicity of steady two-dimensional flows in two–sided lid–driven cavities," *Theor. Comp. Fluid. Dyn.*, Vol. 14, 2001, pp. 223–241.

[37] Karniadakis, G. and Sherwin, S. J., *Spectral/hp element for Computational Fluid Dynamics*, Oxford University Press, 2nd ed., 2005.

[38] Blackburn, H. M. and Sherwin, S. J., "Formulation of a Galerkin spectral element–Fourier method for three-dimensional incompressible flows in cylindrical geometries," *J. Comput. Phys.*, Vol. 197, No. 2, 2004, pp. 759–778.

[39] Theofilis, V., Barkley, D., and Sherwin, S. J., "Spectral/hp element technology for flow instability and control," *Aero. J.*, Vol. 106, 2002, pp. 619–625.

[40] Gonzalez, L. M., Theofilis, V., and Sherwin, S. J., "High-order methods for the numerical solution of the BiGlobal linear stability eigenvalue problem in complex geometries," *International Journal for Numerical Methods in Fluids*, Vol. 65, No. 8, 2011, pp. 923–952.

[41] Gonzalez, L. M., Ahmed, M., Kuehnen, J., Kuhlmann, H., and Theofilis, V., "Three-dimensional flow instability in a lid-driven isosceles triangular cavity," *Journal of Fluid Mechanics*, Vol. 675, 2011, pp. 369–396.

[42] Trefethen, L. N., Trefethen, A. E., Reddy, S. C., and Driscoll, T., "Hydrodynamic stability without eigenvalues," *Science*, Vol. 261, 1993, pp. 578–584.

[43] Schmid, P. and Henningson, D. S., *Stability and Transition in Shear Flows*, Springer, New York, 2001.

[44] Tumin, A. and Reshotko, E., "Spatial Theory of Optimal Disturbances in Boundary layers," *Phys. Fluids*, Vol. 13, 2001, pp. 2097–2104.

[45] Herbert, T., "Parabolized stability equations," *Annual Review of Fluid Mechanics*, Vol. 29, 1997, pp. 245–283.

[46] Keller, H. B., "Numerical solution of bifurcation and nonlinear eigenvalue problems," *Applications of Bifurcation Theory*, edited by P. Rabinowitz, Academic Press, 1977, pp. 359–384.

[47] Åkervik, E., Brandt, L., Henningson, D. S., Hœpffner, J., Marxen, O., and Schlatter, P., "Steady solutions of the Navier–Stokes equations by selective frequency damping," *Phys. Fluids*, Vol. 18, 2006, pp. 068102.

[48] Nichols, J. W. and Lele, S. K., "Global modes and transient response of a cold supersonic jet," *J. Fluid Mech.*, Vol. 669, 2011, pp. 225–241.

[49] Morse, P. M. and Feshbach, H., *Methods of Theoretical Physics, Parts I, II*, McGraw-Hill, 1953.

[50] Farrell, B. F. and Ioannou, P. J., "Generalized stability theory. Part I: Autonomous operators," *J. Atmos. Sci.*, Vol. 53, No. 14, 1996, pp. 2025–2040.

[51] Farrell, B. F. and Ioannou, P. J., "Generalized stability theory. Part II: Nonautonomous operators," *J. Atmos. Sci.*, Vol. 53, No. 14, 1996, pp. 2041–2053.

[52] Karniadakis, G. E. and Sherwin, S. J., *Spectral/hp element methods for Computational Fluid Dynamics (2nd ed.)*, Oxford University Press, 2005.

[53] Barkley, D. and Henderson, R. D., "Three-dimensional Floquet stability analysis of the wake of a circular cylinder," *J. Fluid Mech.*, Vol. 322, 1996, pp. 215–241.

[54] Luchini, P., "Reynolds-number-independent instability of the boundary layer over a flat surface: Optimal perturbations," *J. Fluid Mech.*, Vol. 404, 2000, pp. 289–309.

[55] Blackburn, H. M., Barkley, D., and Sherwin, S. J., "Convective instability and transient growth in flow over a backward-facing step," *J. Fluid Mech.*, Vol. 603, 2008, pp. 271 – 304.

[56] Cantwell, C. D., Barkley, D., and Blackburn, H. M., "Transient growth analysis of flow through a sudden expansion in a circular pipe," *Phys. Fluids*, Vol. 22, 2010, pp. 034101–1–15.

[57] Åkervik, E., Ehrenstein, U., Gallaire, F., and Henningson, D. S., "Global two-dimensional stability measures of the flat plate boundary-layer flow," *Eur. J. Mech. B / Fluids*, Vol. 27, 2008, pp. 501–513.

[58] Blackburn, H. M., Sherwin, S. J., and Barkley, D., "Convective instability and transient growth in steady and pulsatile stenotic flows," *J. Fluid Mech.*, Vol. 607, 2008, pp. 267–277.

[59] Abdessemed, N., Sherwin, S. J., and Theofilis, V., "Linear instability analysis of low pressure turbine flows," *J. Fluid Mech.*, Vol. 628, 2009, pp. 57–83.

[60] Halmos, P. R., *Finite-dimensional vector spaces*, Springer, 1958.

[61] Salwen, H. and Grosch, C., "The continuous spectrum of the Orr-Sommerfeld equation. Part 2. Eigenfunction expansions," *J. Fluid Mech.*, Vol. 104, 1981, pp. 445–465.

[62] Tumin, A., "Receptivity of pipe Poiseuille flow," *J. Fluid Mech.*, Vol. 315, 1996, pp. 119–137.

[63] Ehrenstein, U. and Gallaire, F., "On two-dimensional temporal modes in spatially evolving open flows: the flat-plate boundary-layer," *J. Fluid Mech.*, Vol. 536, 2005, pp. 209–218.

[64] Rodríguez, D., Tumin, A., and Theofilis, V., "Towards the foundation of a global modes concept," 6^{th} Theoretical Fluid Mechanics Conference, Honolulu, HI, June 27-30, 2011, AIAA Paper 2011-3603, 2011.

[65] Theofilis, V., "On steady-state flow solutions and their nonparallel global linear instability," *Advances in Turbulence*, edited by C. Dopazo, Vol. 8, 2000, pp. 35–38.

[66] Holmes, P., Lumley, J., and Berkooz, G., *Turbulence, coherent structures, dynamical systems and symmetry*, Cambridge University Press, 1996.

[67] Sirovich, L., "Turbulence and the dynamics of coherent structures. Part I: Coherent structures," *Quart. Appl. Math.*, Vol. 45, No. 3, 1987, pp. 561–571.

[68] Sirovich, L. and Kirby, M., "Low-dimensional procedure for the characterization of human faces," *J. Opt. Soc. Am. A*, Vol. 4, No. 3, 1987, pp. 519–524.

[69] Sirovich, L., Kirby, M., and Winter, M., "An eigenfunction approach to large scale transitional structures in jet flow," *Phys. Fluids A*, Vol. 2, No. 2, 1990, pp. 127–137.

[70] Rempfer, D. and Fasel, H. F., "Evolution of three-dimensional coherent structures in a flat-plate boundary layer," *J. Fluid Mech.*, Vol. 260, 1994, pp. 351–357.

[71] Aubry, N., Guyonnet, R., and Lima, R., "Spatiotemporal analysis of complex signals: theory and applications," *J. Stat. Phys.*, Vol. 64, No. 3/4, 1991, pp. 683–739.

[72] Koopman, B. O., "Hamiltonian systems and transformations in Hilbert space," *Proc. Natl. Acad. Sci. USA*, Vol. 17, 1931, pp. 315 – 318.

[73] Rowley, C. W., Mezić, I., Bagheri, S., Schlatter, P., and Henningson, D. S., "Spectral analysis of nonlinear flows," *J. Fluid Mech.*, Vol. 641, 2009, pp. 115–127.

[74] Schmid, P. J., "Dynamic mode decomposition of numerical and experimental data." *J. Fluid Mech.*, Vol. 656, 2010, pp. 5–28.

[75] Mezić, I., "Spectral properties of dynamical systems, model reduction and decompositions," *Nonlinear Dynamics*, Vol. 41, 2005, pp. 309–325.

[76] Mezic, I., "Analysis of Fluid Flows via Spectral Properties of the Koopman Operator," *Annual Review of Fluid Mechanics*, Vol. 45, 2013, pp. 357–378.

[77] Schmid, P. J., Li, L., Juniper, M., and Pust, O., "Applications of the dynamic mode decomposition," *J. Fluid Mech.*, Vol. 25, 2011, pp. 249–259.

[78] Rodríguez, D. and Theofilis, V., "On the birth of stall cells on airfoils," *Theor. Comp. Fluid Dyn.*, Vol. 25, No. 1-4, 2011, pp. 105–118.

[79] Rodríguez, D. and Theofilis, V., "Structural changes of laminar separation bubbles induced by global linear instability," *J. Fluid Mech.*, Vol. 655, 2010, pp. 280–305.

[80] Rowley, C. W., Colonius, T., and Murray, R. M., "POD Based Models of Self-Sustained Oscillations in the Flow Past an Open Cavity," AIAA Paper 2000-1969, 2000.

[81] Rowley, C. W., Colonius, T., and Murray, R. M., "Model reduction for compressible flows using POD and Galerkin projection," *Physica D*, Vol. 189, 2004, pp. 115–129.

[82] Segunpta, T. K., Singh, N., and Suman, V., "Dynamical system approach to instability of flow past a circular cylinder," *J. Fluid Mech.*, Vol. 656, 2010, pp. 82–115.

[83] Merzari, E., Ninokata, H., Mahmood, A., and Rohde, M., "Proper orthogonal decomposition of the flow in geometries containing a narrow gap," *Theor. Comp. Fluid Dyn.*, Vol. 23, 2009, pp. 333–351.

[84] Merzari, E., Wang, S., Ninokata, H., and Theofilis, V., "BiGlobal linear stability analysis for the flow in eccentric annular channels and a related geometry," *Phys. Fluids*, Vol. 20, No. 11, 2008, pp. 114104.

[85] Oberleithner, K., Sieber, M., Nayeri, C. N., Paschereit, C. O., Petz, C., Hege, H.-C., Noack, B. R., and Wygnanski, I., "Three-dimensional coherent structures in a swirling jet undergoing vortex breakdown: stability analysis and empirical mode construction," *J. Fluid Mech.*, Vol. 679, 2011, pp. 383–414.

[86] Theofilis, V. and Colonius, T., "An algorithm for the recovery of 2- and 3-D BiGlobal Instabilities of Compressible Flow Over 2-D Open Cavities," *AIAA*, Vol. 4143, 2003.

[87] Gomez, R., *Una estructura de dados basada en aristas para la resolucion de las ecuaciones de Navier-Stokes*, Ph.D. thesis, Universidad Politecnica de Madrid, 2000.

[88] Gomez, R., "BERTA: Resolvedor Transparente a la Malla," Internal Report AP/TNO/4434/005/INTA/02, INTA, 2002.

[89] Issa, R., "Solution of the implicitly discretized fluid flow equations by operator-splitting," *Journal of Computational Physics*, Vol. 62, 1986, pp. 40–65.

[90] Jasak, H., *Error Analysis and Estimation for the Finite Volume Method and Applications to Fluid Flows*, Ph.D. thesis, Imperial College, 1996.

[91] Ferziger, J. and Peric, M., *Computational Methods for Fluid Dynamics*, Springer, 2001.

[92] Van der Vorst, H. A., "Bi-CGSTAB: A Fast and Smoothly Converging Variant of Bi-CG for the Solution of Nonsymmetric Linear Systems," *SIAM J Sci. Stat. Comput.*, Vol. 13, No. 2, 1992, pp. 631–644.

[93] Sanmiguel-Rojas, E., Jimenez-Gonzalez, J., Bohorquez, P., Pawlak, G., and Martínez-Bazán, C., "Effect of base cavities on the stability of the wake behind slender blunt-based axisymmetric bodies," *Physics of Fluids*, Vol. 23, No. 114103, 2011.

[94] Bohorquez, P., Sanmiguel-Rojas, E., Sevilla, A., Jimenez-Gonzalez, J., and Martinez-Bazan, C., "Stability and dynamics of the laminar wake past a slender blunt-based axisymmetric body," *J. Fluid Mech*, Vol. 676, 2011, pp. 110–144.

[95] Bohorquez, P. and Parras, L., "Three-dimensional numerical simulation of the wake flow of an afterbody at subsonic speeds." *Theor. Comp. Fluid Dyn.*, 2012.

[96] Canuto, C., Hussaini, M. Y., Quarteroni, A., and Zang, T. A., *Spectral methods: Fundamentals in single domains*, Springer, 2006.

[97] Boyd, J. P., *Chebyshev and Fourier spectral methods*, Dover Publications, Inc., second edi ed., 2001.

[98] Spalart, P., Moser, R., and Rogers, M., "Spectral methods for the Navier–Stokes equations with one infinite and two periodic directions," *Journal of Computational Physics*, Vol. 96, 1991, pp. 297–324.

[99] Theofilis, V., "Advances in global linear instability analysis of nonparallel and three-dimensional flows," *Progress in Aerospace Sciences*, Vol. 39, 2003, pp. 249–315.

[100] Karniadakis, G. E., Israeli, M., and Orszag, S. A., "High-order splitting methods for the incompressible Navier–Stokes equations," *J. Comput. Phys.*, Vol. 97, No. 3, 1991, pp. 441–443.

[101] Blackburn, H. M. and Henderson, R. D., "A study of two-dimensional flow past an oscillating cylinder," *J. Fluid Mech.*, Vol. 385, 1999, pp. 255–286.

[102] Blackburn, H. M. and Lopez, J. M., "Symmetry breaking of the flow in a cylinder driven by a rotating endwall," *Phys. Fluids*, Vol. 12, No. 11, 2000, pp. 2698–2701.

[103] Blackburn, H. M., Govardhan, R., and Williamson, C. H. K., "A complementary numerical and physical investigation of vortex-induced vibration," *J. Fluids & Struct.*, Vol. 15, No. 3/4, 2001, pp. 481–488.

[104] Blackburn, H. M. and Lopez, J. M., "Modulated rotating waves in an enclosed swirling flow," *J. Fluid Mech.*, Vol. 465, 2002, pp. 33–58.

[105] Keller, H., *Numerical solution of bifurcation and nonlinear eigenvalue problems*, Academic Press, 1997.

[106] Knoll, D. and Keyes, D., "Jacobian-free Newton–Krylov methods: a survey of approaches and applications," *Journal of Computational Physics*, Vol. 193, No. 2, Jan. 2004, pp. 357–397.

[107] Chiba, S., "Three-dimensional global stability analysis for the time-periodic cylinder wake," *Theor. Appl. Mech. Japan*, Vol. 50, 2001, pp. 321–326.

[108] Gómez, F., Gómez, R., and Theofilis, V., "Coupling time-stepping numerical methods and standard aerodynamics codes for instability analysis of flows in complex geometries," 6^{th} Theoretical Fluid Mechanics Conference, Honolulu, HI, June 27-30, 2011, AIAA Paper 2011-3753, 2011.

[109] Goldhirsch, I., Orszag, S. A., and Maulik, B. K., "An efficient method for computing leading eigenvalues and eigenvectors of large asymmetric matrices," *J. Sci. Comput.*, Vol. 2, No. 1, 1987, pp. 33 – 58.

[110] Saad, Y., "Variations of Arnoldi's method for computing eigenelements of large unsymmetric matrices." *Linear Algebra Appl.*, Vol. 34, 1980, pp. 269–95.

[111] Lehoucq, R. B., Sorensen, D. C., and Yang, C., *Arpack User's Guide: Solution of Large-Scale Eigenvalue Problems With Implicitly Restarted Arnoldi Methods (Software, Environments, Tools)*, Soc for Industrial & Applied Math, 1997.

[112] Theofilis, V., Duck, P. W., and Owen, J., "Viscous linear stability analysis of rectangular duct and cavity flows," *Journal of Fluid Mechanics*, Vol. 505, April 2004, pp. 249–286.

[113] Gonzalez, L. M., Theofilis, V., and Gomez-Blanco, R., "Finite Element Methods for Viscous Incompressible BiGlobal Instability Analysis on Unstructured Meshes," *AIAA Journal*, Vol. 45, No. 4, April 2007, pp. 840–854.

[114] Ding, Y. and Kawahara, M., "Linear stability of incompressible fluid flow in a cavity using finite element method," *International Journal for Numerical Methods in Fluids*, Vol. 27, 1998, pp. 139–157.

[115] Theofilis, V., "Globally-unstable flows in open cavities," AIAA Paper 2000-1965, 2000, p. 12 pp.

[116] Theofilis, V., "Advances in global linear instability of nonparallel and three-dimensional flows," *Prog. Aero. Sciences*, Vol. 39 (4), 2003, pp. 249–315.

[117] Sherwin, S. J. and Blackburn, H. M., "Three-dimensional instabilities and transition of steady and pulsatile axisymmetric stenotic flows," *J. Fluid Mech.*, Vol. 533, No. 297-327, 2005.

[118] Shankar, P. N. and Deshpande, M. D., "Fluid mechanics in the driven cavity," *Annual Review of Fluid Mechanics*, Vol. 32, No. 1, Jan. 2000, pp. 93–136.

[119] Ertuck, E., "Discussions On Driven Cavity Flow," *International Journal for Numerical Methods in Fluids*, Vol. 60, 2009, pp. 275–294.

[120] Boppana, V. and Gajjar, J., "Global flow instability in a lid-driven cavity," *International Journal for Numerical Methods in Fluids*, Vol. 62, 2010, pp. 827–853.

[121] Koseff, J. and Street, R., "Visualisation studies of a shear driven three–dimensional recirculating flow," *J. Fluids Eng.*, Vol. 106, 1984, pp. 21–29.

[122] Koseff, J. and Street, R., "The lid-driven cavity flow: A synthesis of qualitative and quantitative observations," *J. Fluids Eng.*, Vol. 106, 1984, pp. 390–398.

[123] Iwatsu, R., Hyun, J. M., and Kuwahara, K., "Analyses of three-simensional flow calculations in a driven cavity," *Fluid Dynamics Research*, Vol. 6, 1990, pp. 91–102.

[124] Iwatsu, R., Ishii, K., Kawamura, T., Kuwahara, K., and Hyun, J. M., "Numerical simulation of three-simensional flow structure in a driven cavity," *Fluid Dynamics Research*, Vol. 5, 1989, pp. 173–189.

[125] Saric, W., "Görtler Vortices," *Annual Review of Fluid Mechanics*, Vol. 26, 1994, pp. 379–409.

[126] Chiang, T., Hwang, R., and Sheu, W., "On end-wall corner vortices in a lid-driven cavity," *J. Fluids Eng.*, Vol. 1119, 1997, pp. 201–204.

[127] Prasad, A. and Koseff, J., "Reynols number and endwall effect on a liddriven cavity flow," *Physics of Fluids*, Vol. 1, No. 209-218, 1989.

[128] Aidun, C. K., Triantafillopoulos, N. G., and Benson, J. D., "Global stability of a lid-driven cavity with through-flow: Flow visualization studies," *Physics of Fluids*, Vol. 3, No. 9, 1991.

[129] Guermond, J., Migeon, G., Pineau, G., and Quartapelle, L., "Start-up flows in a three-dimensional rectangular driven cavity of aspect raton 1:1:2 at Re=1000," *Journal of Fluid Mechanics*, Vol. 450, 2002, pp. 169–199.

[130] Migeon, C., "Details on the start-up development of the Taylor-Gortler-like vortices inside a square-section lid-driven cavity for 1,000 ¡ Re ¡ 3,200," *Experiments in Fluids*, Vol. 33, 2002, pp. 594–602.

[131] Kim, J. and Moin, P., "Application of a Fractional-step Method to Incompressible Navier-Stokes Equations," *Journal of Computational Physics*, Vol. 59, 1985, pp. 308–323.

[132] Ramanan, N. and Homsy, G., "Linear Stability of liddriven cavity flow," *Phys. Fluids*, Vol. 6, 1994, pp. 2690.

[133] Theofilis, V., "Globally unstable basic flows in open cavities," *AIAA Paper 2000-1965.*, 2000.

[134] Albensoeder, S., Kuhlmann, H. C., and Rath, H. J., "Three-dimensional centrifugal-flow instabilities in the lid-driven-cavity problem," *Physics of Fluids*, Vol. 13, No. 1, 2001, pp. 121.

[135] Blackburn, H., "Three-dimensional instability and state selecion in an oscillatory axisymmetric swirling flow," *Physics of Fluids*, Vol. 14, No. 11, 2002, pp. 3983–3996.

[136] De Vicente, J., Rodriguez, D., Theofilis, V., and Valero, E., "Stability analysis in spanwise-periodic double-sided lid-driven cavity flows with complex cross-sectional profiles," *Computers & Fluids*, Vol. 43, No. 1, 2011, pp. 143–153.

[137] Leriche, E., *Direct Numerical simulation of a lid-driven cavity flow by a chebyshev spectral method*, Ph.D. thesis, Ecole Polytechnique Federale de Lausanne, 1999.

[138] Ku, H., Hirsh, R., and Taylor, T., "A Pseudospectral Method fo Solution of the Three-Dimensional Incompressible Navier-Stokes Equations." *Journal of Computational Physics*, Vol. 70, 1987, pp. 439–462.

[139] Benson, J. D. and Aidun, C. K., "Transition to unsteady nonperiodic state in a throughflow liddriven cavity," *Physics of Fluids*, Vol. 4, 1992, pp. 2316–2319.

[140] Chiang, T., Sheu, W., and Hwang, R., "Effect of Reynolds Number on the eddy structure in a lid-driven cavity," *International Journal for Numerical Methods in Fluids*, Vol. 26, 1998, pp. 557–579.

[141] Albensoeder, S. and Kuhlmann, H. C., "Nonlinear three-dimensional flow in the lid-driven square cavity," *Journal of Fluid Mechanics*, Vol. 569, 2006, pp. 465–480.

[142] Albensoeder, S. and Kuhlmann, H., "Accurate three-dimensional lid-driven cavity flow," *Journal of Computational Physics*, Vol. 206, 2005, pp. 536–558.

[143] Theofilis, V., "Global linear instability," *Annu. Rev. Fluid Mech.*, Vol. 43, 2011, pp. 319–352.

[144] Roache, P., "Perspective: A method for uniform reporting of grid refinement studies," *J. Fluids Eng.*, Vol. 116, No. 405, 1994.

[145] Scruton, C. and Walshe, D., "A means for avoiding wind-excited oscillations of structures with circular or nearly circular cross section," Aero Report 335, Natl. Phys. Lab. (U.K.), 1957.

[146] Williamsom, C. and Govardhan, R., "Vortex-induced vibrations," *Annual Review of Fluid Mechanics*, Vol. 36, 2004, pp. 413–455.

[147] Zdravkovich, M., "Review and classification of various aerodynamic and hydrodinamic means for suppressing vortex shedding." *Journal of Wind Engineering and Industrial Aerodynamics*, Vol. 7, 1981, pp. 145–189.

[148] Scruton, C., "Note on a device for the suppression of the vortex excited oscillations of flexibles structures of circular or near circular section, with special reference to its application to tall statcks," Aero Note 1012, Natl. Phys. Lab. (U.K.), 1963.

[149] Ishizaki, H., Hara, H., and Shimada, T., "The efficiency of helical strakes for the suppression of virtex-excited oscillation of steel stacks," *Eng. Struct.*, Vol. 6, October 1984, pp. 334–339.

[150] Allen, D., Henning, D., and Lee, L., "Performance Comparisons of Helical Strakes for VIV suppression of risers and tendons," *Offshore Technology Conference*, No. OTC-16186, Houston, Texas, May 2004.

[151] Trim, A., Braaten, H., Lie, H., and Tognarelli, M., "Experimental investigation of vortex-induced vibration of long marine risers," *Journal of Fluids and Structures*, Vol. 21, No. 3, 2005, pp. 335–361.

[152] Brankovic, M. and Bearman, P., "Measurements of transverse forces on circular cylinders undergoing vortex-induced vibration," *Journal of Fluids and Structures*, Vol. 22, No. 6-7, 2006, pp. 829–836.

[153] Lubbad, R., Sveinung, L., Gudmestad, O. T., Torum, A., and Moe, G., "Vortex-induced vibrations of slender Marine Risers - Effects of Round-Sectioned Helical Strakes," *Proceedings of the Seventeenth International Offshore and Polar Engineering Conference*, The International Society of Offshore and Polar Engineers ISOPE, 2007.

[154] Korkischko, I. and Meneghini, J., "Experimental investigation of flow-induced vibration on isolated and tandem circular cylinders fitted with strakes," *Journal of Fluids and Structures*, Vol. 26, No. 4, 2010, pp. 611–625.

[155] Zhou, T., Razali, S.F.M., H. Z., and Cheng, L., "On the study of vortex-induced vibration of a cylinder with helical strakes," *Journal of Fluids and Structures*, Vol. 27, 2011, pp. 903–917.

[156] Constantinides, Y. and Oakley, O., "Numerical Prediction of bare and straked cylinder VIV," *Proceedings of the 25th International Conference on Offshore Mechanics and Arctic Engineering*, OMAE, June 2006.

[157] Korskischko, I. and Meneghini, J., "Volumetric reconstruction of the mean flow around circular cylinder fitted with strakes," *Exp Fluids*, , No. 51, 2011, pp. 1109–1122.

[158] Carmo, B., Gioria, R. S., Korkischko, I., Freire, C. M., and Meneghini, J., "Two- and Three-dimensional simulations of the flow around a cylinder fitted with strakes," *Proceedings of the 31st International COnference on Ocean, Offshore and Artic Engineering*, edited by OMAE, No. OMAE2012-83603, June 2012.

[159] Fornberg, B., "A numerical study of steady viscous flow past a circular cylinder," *Journal of Fluid Mechanics*, Vol. 98, No. 819, 1980.

[160] Zebib, a., "Stability of viscous flow past a circular cylinder," *Journal of Engineering Mathematics*, Vol. 21, No. 2, 1987, pp. 155–165.

[161] Noack, B. R. and Eckelmann, H., "A global stability analysis of the steady and periodic cylinder wake," *Journal of Fluid Mechanics*, 1994, pp. 297–330.

[162] Park, J., Kwon, H., and Choi, H., "Numerical solution of flow past a circular clinder at Reynolds number up to 160," *KSME Int. J.*, Vol. 12, No. 1200, 1998.

[163] Ye, T., Mittal, R., Udaykumar, H., and Shyy, W., "An accurate Cartesian grid method for viscous incompressible flows with complex immersed boundaries," *J. Comput. Phys.*, Vol. 156, pp. 209–240.

[164] Mittal, S. and A., R., "Control of vortex shedding behind circular cylinder for flows at low Reynolds numbers," *International Journal for Numerical Methods in Fluids*, Vol. 35, 2001, pp. 421–447.

[165] Kim, J., Kim, D., and Choi, H., "An inmersed-boundary finite-volume method for simulations of flow in complex geometries," *J. Comput. Phys.*, Vol. 171, 2001, pp. 132–150.

[166] Lima E Silva, A., Silveira-Neto, A., and Damasceno, J., "Numerical simulation of two-dimensional flows over a circular cylinder using the immersed boundary method," *Journal of Computational Physics*, Vol. 189, 2003, pp. 351–370.

[167] Noack, B. R., Afanasiev, K., Morzyński, M., Tadmor, G., and Thiele, F., "A hierarchy of low-dimensional models for the transient and post-transient cylinder wake," *Journal of Fluid Mechanics*, Vol. 497, Dec. 2003, pp. 335–363.

[168] Giannetti, F. and Luchini, P., "Structural sensitivity of the first instability of the cylinder wake," *Journal of Fluid Mechanics*, Vol. 581, May 2007, pp. 167.

[169] Henderson, R. D. and Barkley, D., "Secondary instability in the wake of a circular cylinder," *Physics of Fluids*, Vol. 8, No. 6, 1996, pp. 1683.

[170] Williamsom, C., "Vortex dynamics in the cylinder wake," *Ann. Rev. Fluid Mech.*, Vol. 28, No. 477, 1996.

[171] Blackburn, H. M., Marques, F., and Lopez, J., "Symmetry breaking of the two-dimensional time-periodic wakes," *Journal of Fluid Mechanics*, Vol. 552, 2005, pp. 395–411.

[172] Barkley, D., "Linear analysis of the cylinder wake mean flow," *Europhysics Letters*, Vol. 75, No. 5, 2006, pp. 750–756.

[173] Marquardt, D. W., "An Algorithm for the Least-Squares Estimation of Nonlinear Parameters," *SIAM Journal of Applied Mathematics*, Vol. 11, No. 2, June 1963, pp. 431–441.

[174] Levenberg, K., "A Method for the Solution of Certain Non-linear Problems in Least-Squares," *Quarterly of Applied Mathematics*, Vol. 2, No. 2, July 1944, pp. 164–168.

[175] De Vicente, J., Valero, E., González, L., and Theofilis, V., "Spectral multi-domain methods for BiGlobal instability analysis of complex flows over open cavity configurations," 36th Fluid Dynamics Conference and Exhibit, San Francisco CA, June 5–8, 2006, AIAA Paper 2006-2877, 2006.

[176] Theofilis, V. and Colonius, T., "Three-dimensional instablities of compressible flow over open cavities: direct solution of the BiGlobal eigenvalue problem," 34th Fluid Dynamics Conference and Exhibit, AIAA Paper 2004-2544, Portland, Oregon, June 28 – July 1, 2004 2004.

[177] Sipp, D. and Lebedev, A., "Global stability of base and mean flows: a general approach and its applications to cylinder and open cavity flows," *J. Fluid Mech.*, Vol. 593, 2007, pp. 333–358.

[178] De Vicente, J., Paredes, P., Valero, E., and Theofilis, V., "Wave-like Disturbances on the Downstream Wall of an Open Cavity," 6th aiaa theoretical fluid mechanics conference, 27 - 30 june 2011. Honolulu, HI, June 27-30, AIAA Paper 2011-3754, 2011.

[179] Vicente, J. D., Valero, E., and Theofilis, V., "Numerical Considerations in Spectral multi-domain Methods for BiGlobal Instability Analysis of Open Cavity Configurations," *Progress in Industrial Mathematics at ECMI 2006*, edited by S. B. Heidelberg, Vol. 12, 2006, pp. 201 – 206.

[180] Gómez, F., Theofilis, V., Paredes, P., Liu, Q., and Wei, H., "On the role of global flow instability analysis in closed loop flow control," 42nd Fluid Dynamics Conference and Exhibit, New orleans, LA, June 25-28, 2012, AIAA Paper 2012-2679, 2012.

[181] Brès, G., "Numerical simulation of three-dimensional instabilities in cavity flows," *PhD thesis. California Institute of Technology*, 2007.

[182] Cattafesta, L. N. and Sheplak, M., "Actuators for active flow control," *Annu. Rev. Fluid Mech.*, Vol. 43, 2011, pp. 247–272.

[183] Bewley, T. R., "Flow Control: New Challenges for a New Renaissance," *Progress in Aerospace Sciences*, Vol. 37, 2001, pp. 21–58.

[184] Kim, J. and Bewley, T. R., "A linear systems approach to flow control," *Annu. Rev. Fluid Mech.*, Vol. 39, 2007, pp. 383–417.

[185] Collis, S. S., Joslin, R. D., Seifert, A., and Theofilis, V., "Issues in active flow control: theory, control, simulation and experiment," *Prog. Aero. Sciences*, Vol. 40, No. 4-5, 2004, pp. 237–289.

[186] Åkervik, E., Hoepffner, J., Ehrenstein, U., and Henningson, D. S., "Optimal growth, model reduction and control in a separated boundary-layer flow using global eigenmodes," *Journal of Fluid Mechanics*, Vol. 579, May 2007, pp. 305.

[187] Rowley, C. W., "Model reduction for fluids using balanced proper orthogonal decomposition," *Int. J. Bifurc. Chaos*, Vol. 15, No. 3, 2005, pp. 997–1013.

[188] Luchtenburg, D. M., Günther, B., Noack, B., King, R., and Tadmor, G., "A generalized mean-field model of the natural and high-frequency actuated flow around a high-lift configuration," Vol. 623, 2009, pp. 283–316.

[189] Hill, D. C., "A theoretical approach for the restabilization of wakes," AIAA Paper 92–0067, 1992.

[190] Strykowski, P. and Sreenivasan, K., "On the formation and suppression of vortex "shedding" at low Reynolds numbers," *J. Fluid Mech.*, Vol. 218, 1987, pp. 71–107.

[191] Chomaz, J.-M., "Global instabilities in spatially developing flows: non-normality and nonlinearity," *Annu. Rev. Fluid Mech.*, Vol. 37, 2005, pp. 357 –392.

[192] Tumin, A. and Fedorov, A. V., "Instability Wave Excitation by a Localized Vibrator in the Boundary Layer," *J. Appl. Mech. Tech. Phys.*, Vol. 25, 1984, pp. 867–873.

[193] Tumin, A., Wang, X., and Zhong, X., "Direct Numerical Simulation and the Theory of Receptivity in a Hypersonic Boundary Layer," *Phys. Fluids*, Vol. 19, 2007, pp. 014101.

[194] Golub, G. and Van Loan, C., *Matrix Computations*, The Johns Hopkins University Press, 3rd ed., 1996.